UNIVERSITÀ
DEGLI STUDI
FIRENZE

Dottorato di Ricerca in Ingegneria Industriale

Ciclo XXVI

Development and Experimental Validation of Innovative Models to Predict Wheel and Rail Wear on Complex Railway Networks

Settore Scientifico Disciplinare ING/IND 13

Candidato

Ing. Marini Lorenzo

Tutor

Dott. Ing. Rindi Andrea

Co-Tutors

Prof. Toni Paolo

Dott. Ing. Meli Enrico

Coordinatore del Dottorato

Prof. De Lucia Maurizio

Anni 2011/2013

Alla mia famiglia

Contents

List of Figures

List of Tables

Ringraziamenti

Desidero ringraziare il mio Tutor Dott. Ing. Andrea Rindi ed il Prof. Paolo Toni per il supporto e l'incoraggiamento fornito durante lo svolgimento dell'attività di ricerca. Un ringraziamento doveroso al Dott. Ing. Enrico Meli per i preziosi consigli e l'aiuto che mi ha concesso durante questi anni.

Una menzione particolare a tutti gli stimati colleghi grazie alla cui collaborazione ho potuto intraprendere un persorso di accrescimento professionale ed in particolare un sentito grazie all'Ing. Alice Innocenti con la quale ho avuto il piacere di instaurare un rapporto di sincera amicizia.

Il ringraziamento più grande va ai miei genitori che, con i loro sacrifici, mi hanno permesso di arrivare fin qui.

Chapter 1

Introduction

Wear phenomena due to wheel-rail interaction is a main critical aspect in railway applications; in fact the evolution of the wheel and rail profiles shape that ensues from it has a deep effect on both the dynamics and the stability of the vehicle causing a running performance variation.

The wheel and rail surfaces are subjected to high normal and tangential contact stresses. Contact forces change magnitude and orientation as the wheel travels over the rail curves, crossings, and local surface perturbations; the constantly changing contact patch moves over the wheel tread and to a certain extent the flange. The contact is nominally rolling but a small amount of local sliding takes place at the interface; the removal of material from the wheel and rail surfaces by wear is a function of the sliding and contact stresses.

From a safety viewpoint the arising of a contact geometry which may compromise the vehicle stability or increase the derailment risk due to wheels climbing over the rail has to be avoid. Profile changes also cause higher maintenance cost, mainly concerned with the periodically re-profiling operations of wheels and the undesirable replacements of rails, necessary to re-establish the original profiles.

Because of these reasons, the development of a mathematical model for the prediction of the wear at the wheel-rail interface represents a very powerful tool to plan the maintenance interventions, leading both to an increase of the running safety and a considerable cost saving. A reliable wear model can be used to optimize the original wheel and rail profiles and to obtain a more uniform wear on rolling surfaces. In such a way the overall amount of worn material can be reduced, the mean time between two maintenance operations can be increased and, at the same time, the dynamical performance of the wheel-rail pair can be kept approximately constant between two succeeding repair interventions. The shape optimization of profiles for the reduction of wear at the wheel-rail interface represents so an important aspect in railway field and

various approaches were developed to obtain a satisfactory combination of wheel and rail profiles [6][18][31][34].

In the literature there are many interesting works dealing with wheel-rail wear modeling based both on global and local approaches to the wear estimation. In the global approaches, often used by commercial multibody software to reduce the computational load despite of the model accuracy [26][39], the wear is evaluated without taking into account the contact patch. The local approaches [21][35][41], instead, subdivide the contact patch into adhesion and creep area, leading to more accurate results but increasing the computational time; some works in which the differences between global and local wear approaches are carefully investigated can be found in the literature [36].

In most cases suitable wear model are developed to investigate only the wheel wear evolution [10][13][21] because of the several time consumption required by the rail wear study. However a substantial lack is present in the literature concerning wear models capable of estimate the simultaneous wheel and rail profiles evolution (both global and even more local) specially developed for complex railway network applications. In this case the computational load needs to carry out the exhaustive simulation of vehicle dynamics and wear evaluation turns out to be absolutely too high for each practical purpose.

Moreover one of main critical aspect in the wear evaluation is the availability of experimental data for the validation of the model, because the wear is a long-term phenomenon which requires several months of monitoring to collect the data; usually the experimental campaigns are carried out only in dry contact condition [21][44][50]. If on line experimental measurement cannot be carried out, the problem can be overcome carrying out experimental proofs on a scaled test rig [5][21], in some case also related to wet contact condition [16].

In this Ph.D. Thesis will be present a procedure to estimate the evolution of the wheel and rail profiles due to wear specifically developed for complex railway networks [42][43][44][48][49][50]. The general layout of the model consists of two mutually interactive parts: the vehicle model (multibody model and 3D global contact model) and the wear model (local contact model, wear evaluation and profiles update) (see Figure 2.1). Concerning the vehicle model, the multibody model accurately reproduces the dynamics of the vehicle, taking into account all the significant degrees of freedom. The 3D global contact model [3][27], detects the wheel-rail contact points by means of an innovative algorithm based on suitable semi-analytic procedures and then, for each contact point, calculates the contact forces through Hertz's and Kalker's theories [17][24][25]. Thanks to the numerical efficiency of the new contact model, the two models interact directly online during the simulation of the vehicle dynamics.

As regards the wear estimation, the model is based on a local contact model (in

this case the Kalker's FASTSIM algorithm) and on a experimental relationship for the calculation of the removed material [5][13]. The wear model, starting from the outputs of the vehicle model (contact points, contact forces and global creepages), calculates the total amount of removed material due to wear and its distribution along the wheel and rail profiles. The removal of the material is carried out considering the different time scales characterizing the wear evolution on the wheel and on the rail respectively.

A new track statistical approach to reach relevant results in a reasonable time will be proposed to overcome the critical issue related to the computational effort of the wear prediction models [42]; more specifically it is suggested to replace the entire railway line with a discrete set of N_c different curved tracks (classified by radius, superelevation and traveling speed) statistically equivalent to the original network. The new approach allows a substantial reduction of the computational load and, at the same time, assures a good compromise in terms of model accuracy. The proposed model will be validated with experimental data referred to an Italian critical scenario that exhibits serious problems in terms of wear concerning the Aosta-Pre Saint Didier railway line and the vehicle DMU Aln 501 Minuetto; track and experimental data have been provided by the University of Florence partners' Trenitalia S.p.A. and Rete Ferroviaria Italiana. Subsequently, to further validate the innovative model, an exhaustive comparison with the wear evaluation model implemented in the Simpack commercial multibody software will be performed, both in terms of accuracy and efficiency [48].

The last chapter of this Ph.D. Thesis concerns with the main industrial applications of the proposed model in railway field. The wear model is employed to assess the performance in terms of wear of a new wheel profile designed with a suitable procedure having the aim to research the wheel profile shape optimized for the reduction of wear at wheel-rail interface. The proposed optimization procedure, with respect to the state of the art [6][18][31][34], introduces innovative features since it permits to work directly on the contact points and on their distribution, with a consequent improvement in terms of wear control, stability and guidance [45][46][47]. The prediction of the wheel and rail maintenance intervals is another interesting issue that could be overcome thanks to appropriate wear model; in this way also preventive measures, i.e. the fitting of suitable wheel and rail greasers, could be planned during the vehicle design in order to increase both the wheel and the rail life cycle, with considerable cost saving.

Chapter 2

General Architecture of the Model

The general architecture of the model developed for studying the wear phenomena on complex railway lines is shown in the block diagram in Fig. 2.1 in which two different main parts are present: the *vehicle model* necessary to perform the dynamical analysis and the *wear model*.

The *vehicle model* consists of the multibody model of the benchmark railway vehicle and the 3D global contact model that, during the dynamical simulation, interact directly online creating a loop. At each time integration step the former evaluates the kinematic variables (position, orientation and their derivatives) relative to the wheelsets and consequently to each wheel - rail contact pair. At this point, starting from the kinematic quantities the 3D global contact model calculates the global contact variables (contact points and contact forces, contact areas and global creepages); it is based on both an innovative algorithm for the detection of the contact points [3][27] and Hertz's and Kalker's global theories for the evaluation of the contact forces [25]. The global contact variables are then passed to the multibody model to carry on the vehicle dynamics simulation.

The dynamic simulations have been performed in the commercial Multibody Software (MBS) Simpack. In particular, the multibody model has been defined in the Simpack Rail environment, while the wheel-rail 3D global contact model, implemented in C/C++ language, has been customized by means of a specifically developed FORTRAN routine defined within the Simpack User routine module.

The main inputs of the *vehicle model* are the multibody model of the railway vehicle and the corresponding railway track. In the wear estimation research activities the track description is a critical task due to the complexity of the railway networks to be studied: in fact the exhaustive simulation of the vehicle dynamics and of the wear evolution on overall the railway line turns out to be too expensive concerning computation times, memory consumption and the availability and collection of the

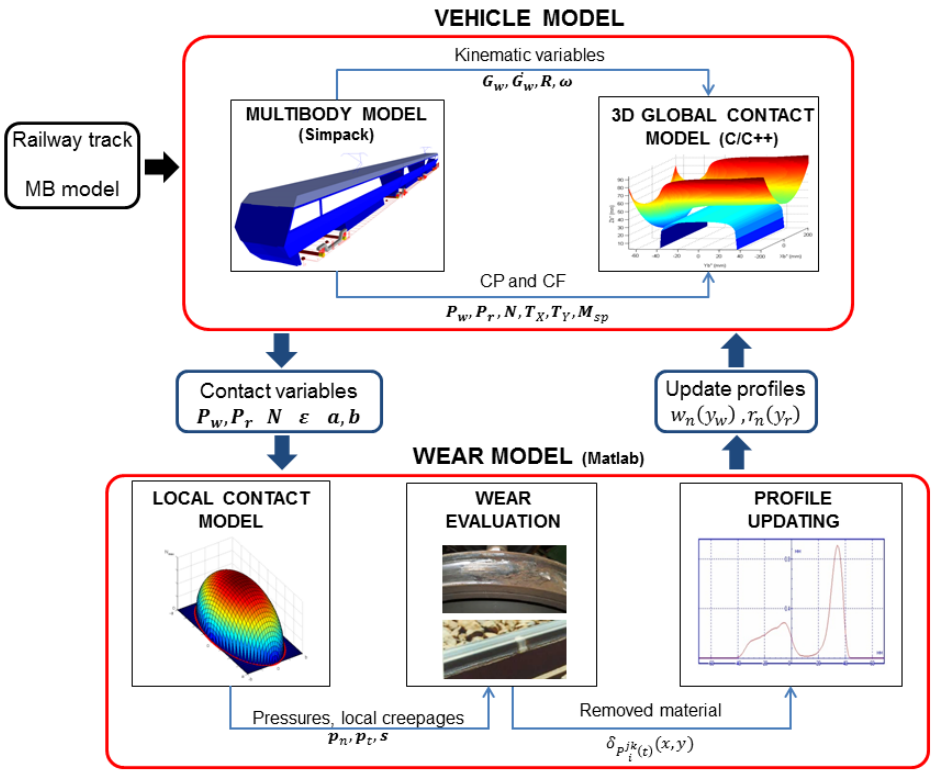

Figure 2.1: General Architecture of the Model.

experimental data needed for the model validation. To overcome these limitations, a new statistical approach will be developed to achieve general significant results in a reasonable time; in particular the entire considered railway network will be replaced with a discrete set of N_c different curved tracks (classified by radius, superelevation and traveling speed) statistically equivalent to the original net. In the first phase of the thesis the wear model will be validated considering the whole track configuration; then the equivalent track representation derived by means of statistical methods will be introduced focusing on the wear modeling differences between the two cases and comparing the results obtained from the efficiency and accuracy viewpoint.

The *wear model* is the part of procedure concerning with the prediction of worn material amount to be removed from the wheel and rail surfaces and it is made up of three distinct phases: the local contact model, the wear evaluation and the profile update. The local contact model (based both on Hertz's local theory and on simplified Kalker's algorithm FASTSIM), starting from the global contact variables, estimates the local contact stresses and creepages inside the contact patch and detects the creep zone of the contact area. Subsequently the distribution of removed material is calculated both on the wheel and on the rail surface only within the creep area by using an experimental relationship between the removal material and the energy dissipated by friction at the contact interface [5][13]. Finally the wheel and rail worn profiles are

derived from the original ones through an appropriate update strategy. The new updated wheel and rail profiles are then fed back as inputs to the *vehicle model* and the whole model architecture can proceed with the next discrete step. In particular, since the new wear model is conceived to describe complex railway networks (composed by several different tracks traveled by different vehicles), it is natural to consider, in the first step, the wear evolution of a mean profile both for wheel and rail without distinguishing the single wheels and the single tracks. A main topic of the wear model is the suitable simulation campaign developed to permit the simultaneous treatment of wheel and rail wear evolution. The wear model has been fully implemented in the Matlab environment.

The evolution of the wheel and rail profiles is therefore a discrete process. The choice of the discrete step is a main issue and, as it will be clarified in the following, has to consider the difference between the time scales characterizing the wheel and rail wear evolution rates. For the wheel wear prediction the following considerations are valid:

1. the total mileage km_{tot} traveled by the considered vehicle has been subdivided in steps of length equal to km_{step} with a suitable strategy;

2. within each discrete step of the whole model (corresponding to km_{step} kilometers traveled by the vehicle) the wheel profile is supposed to be constant.

The depth of the rail wear does not depend on the distance traveled by vehicle but on the number of vehicles moving on the track. Therefore a different approach for evaluating the discrete step for the rail, based on the total tonnage burden on the track M_{tot}, is needed:

1. dividing the total tonnage M_{tot} by the vehicle mass M_v, the corresponding vehicle number N_{tot} has been calculated; then N_{tot} has been subdivided in steps equal to N_{step};

2. within each discrete step (corresponding to N_{step} vehicles moving on the track) the rail profile is supposed to be constant.

As regards the discretization strategy, the number of discrete steps should be chosen according to a good balance between the model precision and the computational load (an increase of the step number increases the model precision but, at the same time, the computational load increases too). Furthermore several types of update procedures exist [21][41]: the constant step and the adaptive step are the main ones. In the first one a constant update step is defined while the second one is based on the definition

of a threshold value that imposes the maximum material quantity to remove at each profiles update; consequently the update step is variable. Both the methods have been considered and the second one has been chosen due to the following reasons:

1. the adaptive step is more suitable to follow the nonlinear behavior of the wear evolution;

2. the wear evolution on both wheel and rail is, in a first phase, characterized by an higher rate because of the initial non conformal contact between the unworn profiles while in a second phase a slower rate due to the high conformal contact is present. For these reason an adaptive step follows the wear phenomena better than a constant one.

Chapter 3

The Vehicle Model

This chapter deals with the description of the vehicle model to be used in the multibody simulations. The vehicle model, as hinted in the chapter 2, can be usefully considered made up of the multibody part which includes all the significant elements of the real railway vehicle and of the global contact model, through which the track and the wheel-rail interaction are implemented. In the first part of the chapter, the most significant characteristics of the Simpack multibody models will be described briefly without getting down to the modeling details [20][30][40]; in the second part, the analytic description of global contact model will be accurately presented [3][17][24][25][27].

3.1 The Multibody Models

In the present research the multibody approach have been chosen to simplify the handling of complex mechanical systems such as railway vehicles without introducing significant simplifications. In fact, in the multibody approach a generic mechanical system is being implemented as a lumped parameter model, mainly made up of rigid or elastic bodies interconnected by means of force elements and constraints which can reproduce the dynamics behavior for large displacements, taking into account all the relevant nonlinearities as well.

In the present work, according to Trenitalia S.p.A. and Rete Ferroviaria Italiana (RFI) three different vehicles have been modeled in Simpack environment to investigate the wear phenomena. The three considered vehicles are the following:

- Aln 501 Minuetto;
- Vivalto coach;
- E.464 locomotive.

The analyses have been carried out with the Aln 501 Minuetto and with a composition of the Vivalto coach pulled by a E.464 locomotive. All the three multibody models have been built by consulting the technical documentation provided by Trenitalia, hence the models are a close representation of the real vehicles. Since structural analysis and response at high frequency were not of interest in this work, all the bodies have been introduced in the models are rigid.

3.1.1 The Aln 501 Minuetto Vehicle

The DMU Aln 501 Minuetto is a passenger transport unit produced by Alstom S.A. widespread in Italian Railways where it is equipped with the standard ORE S1002 wheel profile running on UIC 60 rail profile canted at 1/20 rad. This particular vehicle exhibits severe wear and stability problems mainly caused by the adopted matching. It is a diesel fixed composition unit (DMU) made up of three coaches (see Fig. 3.1): the traction is distributed on the bogies at the ends while the intermediate ones are trailer bogies of Jacobs type (see Figs. 3.2-3.3), hence shared between two coaches, and therefore the wheel arrangements is Bo-2-2-Bo. The coaches are characterized by low-floor structure to leg up the reduced mobility users.

Figure 3.1: The Aln 501 Minuetto vehicle.

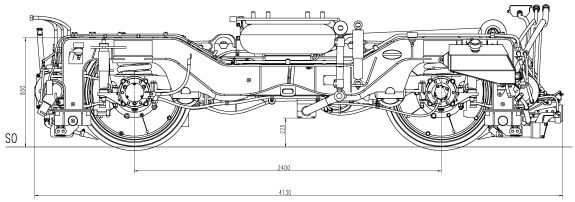

Figure 3.2: The Minuetto motor bogie.

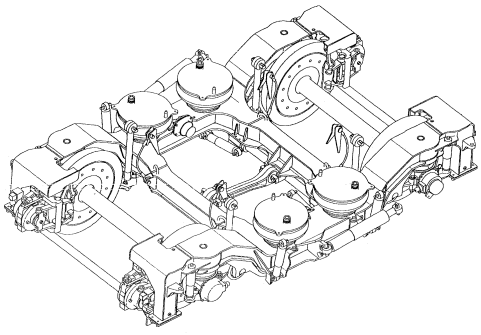

Figure 3.3: The Minuetto Jacobs bogie.

The Aln 501 Minuetto mechanical structure and inertial, elastic and damping prop-

erties can be found in literature [20][40]. The Tab. 3.1 shows the main characteristics of the considered vehicle.

Table 3.1: Main characteristics of the Aln 501 Minuetto.

Length	51.9 m
Width	2.95 m
Height	3.82 m
Bogie pivot distances	14.8-13.8-14.8 m
Bogie wheelbase	2.80 m
Unladen weight	100 t
Wheel arrangement	Bo-2-2-Bo
Wheel diameter	850 mm
Max speed	130 km/h

In Tab. 3.2 the most significant inertia properties of the vehicle are shown: motors and gear boxes have not been modeled and their inertia properties have been included in the motor bogie and in the motor wheelset (indicated in Tab. 3.2 with *Bogie m* and *Wheelset m* respectively) in order to take into account their different influence on the unsprung and sprung mass. The multibody model has been realized in the Simpack Rail environment (see Fig. 3.4) and consists of thirty-one rigid bodies:

- three coaches;
- four bogies: the intermediate ones, interposed between two successive coaches, are trailer bogies while the other ones are motor bogies;
- eight wheelsets: two for each bogie;
- sixteen axleboxes: two for each wheelset.

Table 3.2: Inertia properties of the multibody model.

MBS body	Mass kg	Roll Inertia kgm^2	Pitch Inertia kgm^2	Yaw Inertia kgm^2
Coach M	31568	66700	764000	743000
Coach T	14496	30600	245000	236000
Bogie m	3306	1578	2772	4200
Bogie t	3122	1674	3453	5011
Wheelset m	2091	1073	120	1073
Wheelset t	1462	1027	120	1027

The rigid bodies are connected by means of appropriate elastic and damping elements; particularly the vehicle, like the most part of passenger trains, is equipped with two suspension stages to fulfill the different requirements of dynamic behavior

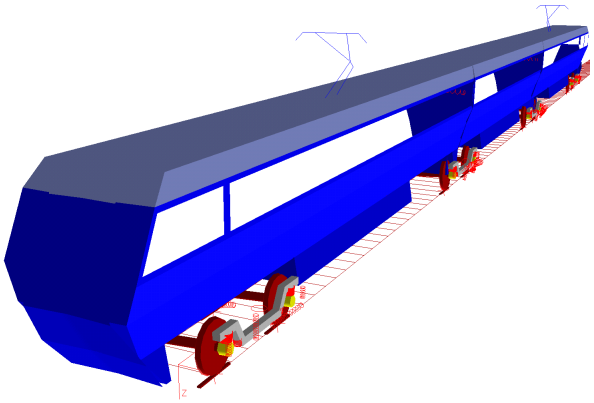

Figure 3.4: Global view of the Minuetto multibody model.

and passenger comfort. The primary suspensions (see Figs. 3.5-3.6), which link the axleboxes with the bogie frame, are constituted by Flexicoil springs, made up of two coaxial springs, which mainly provide the vertical stiffness in this stage; the Flexicoil element have also a significant stiffness in the radial direction, thanks to the rubber wedge (Sommier) which encloses the external coils of the two springs. Moreover an internal rubber vertical bumpstop is present. Since the stability against the hunting at high speed in straight tracks requires higher longitudinal and lateral stiffness, the first one is entrusted to a longitudinal linking arm which connects the axlebox with the frame, while the lateral one is provided by a silent block (Sutuco). A non linear damper is responsible for the damping of the vertical relative displacements while there are no dedicated damping elements for the lateral and longitudinal directions.

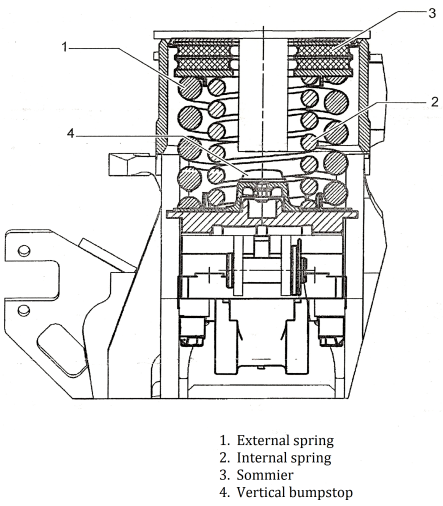

Figure 3.5: The Minuetto primary suspension.

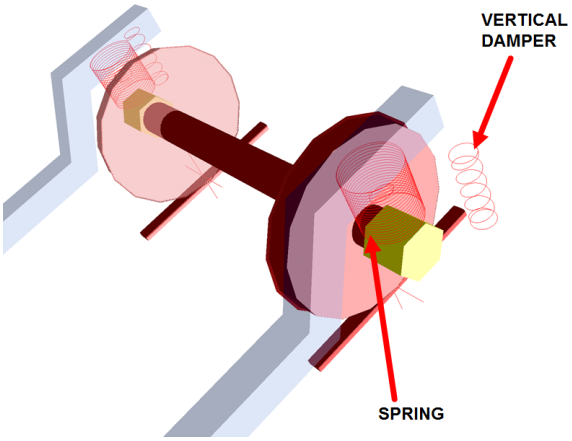

Figure 3.6: The Minuetto primary suspension modeling.

The secondary suspensions connect the bogies to the coaches (see Fig. 3.7) and comprise the following elements:

- two air springs (four in the Jacobs bogie);

- six non linear dampers (lateral, vertical and anti - yaw dampers);
- one non linear traction rod;
- a torsion bar;
- two non linear lateral bumpstops.

Air springs are widely used in the secondary suspensions of low-floor trains because besides the passengers' comfort, they also provide a simple automatic regulation of the coaches height which allow the coach floor to remain at the curb height whatever the vertical load in the springs is. However, since the air springs provide a correct stiffness in the vertical direction but a too lower stiffness for the longitudinal and lateral forces to be balanced, other force elements have to be included in this stage. The longitudinal rod transmits the traction and braking efforts and provides the longitudinal stiffness, whereas the lateral relative displacements are bounded by lateral bumpstops: the correct rolling stiffness is achieved with the torsion bar. All the dampers are viscous.

The connection between two coaches consists of a stiffness element and a non linear damper that attenuates the relative lateral and roll motions.

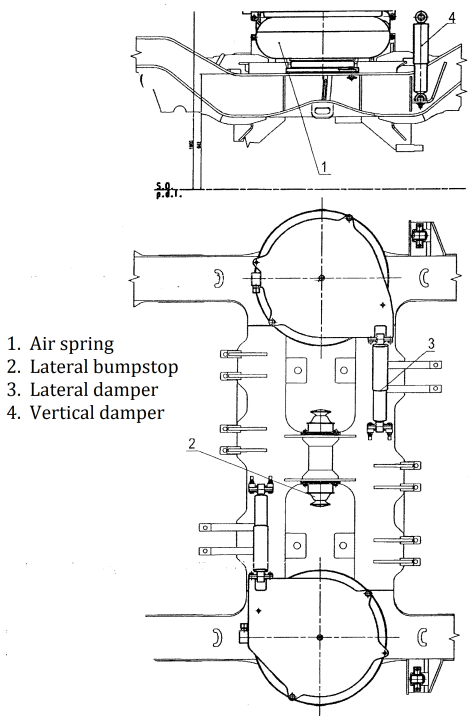

Figure 3.7: The Minuetto secondary suspension.

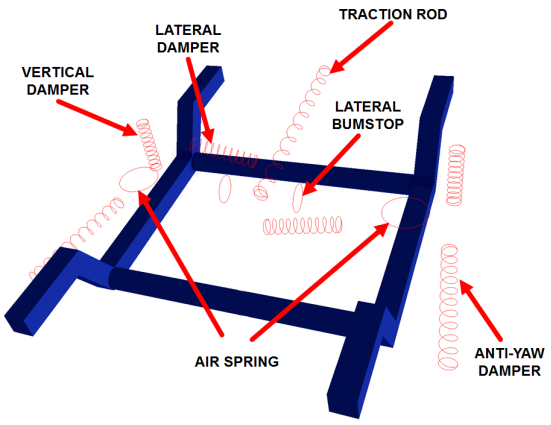

Figure 3.8: The Minuetto secondary suspension modeling.

Both the stages of suspensions have been modeled by means of three-dimensional viscoelastic force elements taking into account all the mechanical non linearities of the

system (bumpstops clearance, dampers and rods behavior). The main linear characteristics of the suspensions are shown in Tab. 3.3 while the nonlinear characteristics are imposed as a function of displacement and velocity for the springs and the dampers respectively (see Figs. 3.9-3.10).

Table 3.3: Main linear stiffness properties of the ALn 501 Minuetto.

Primary suspension	Flexicoil k_z	9.01E+05 N/m
	Flexicoil k_x, k_y	1.26E+06 N/m
	Sutuco bushing k_x	2.0E+07 N/m
	Sutuco bushing k_y	1.5E+07 N/m
Secondary suspension	Airspring k_z	3.98E+05 N/m
	Airspring k_x, k_y	1.2E+05 N/m
	Anti-roll bar k_α	2.6E+06 Nm/rad
Coach connection	Bushing k_x, k_z	7.24E+07 N/m
	Bushing k_y	5.2E+06 N/m

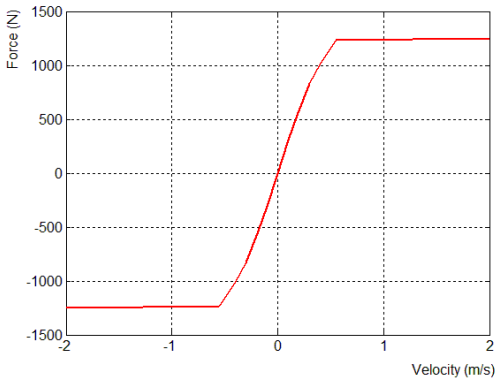

Figure 3.9: Example of nonlinear characteristic: vertical damping of the primary suspension.

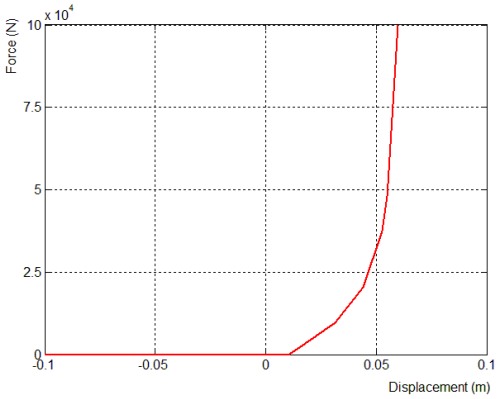

Figure 3.10: Example of nonlinear characteristic: lateral bumpstop stiffness of the secondary suspension.

3.1.2 The Vivalto Vehicle

The other railway vehicle considered in this research activity is a vehicle composition widely used on the Italian railway network for the regional passenger transport, comprising a Vivalto passenger transport unit and a E.464 locomotive (see Fig. 3.11); in the following the main characteristics of the multibody models of the two separated units, built in Simpack environment (see Fig. 3.12), are described.

The Vivalto Coach Multibody Model

The Vivalto is a two-floor coach produced by the Corifer consortium. "Vivalto" is also the name of the typical train composition (Fig. 3.11) in which this coach is

Figure 3.11: The Vivalto Train.

employed, made up of five coaches hauled by a electrical E.464 locomotive. The main feature of the Vivalto coach is the possibility to hold the passengers on two different levels realized in the middle of the carriage; the weight increase resulting from this configuration has led to install three ventilated brake discs for each wheelset, in order to obtain good braking performance. The main general characteristics of the coach are summarized in Tab. 3.4.

Table 3.4: Main characteristics of the Vivalto coach.

Length	26.1 m
Width	2.72 m
Height	4.30 m
Bogie pivot distances	20.0 m
Bogie wheelbase	2.50 m
Unladen weight	50 t
Wheel diameter	920 mm
Max speed	160 km/h

The coach is equipped with two trailer bogies with two suspension stages designed by Siemens company, marked SF-400; an isometric view of the resultant multibody model of this bogie is shown in Fig. 3.13. The main inertia properties of the whole Simpack multibody model are summed up in Tab. 3.5 [20][40].

Table 3.5: Inertia properties of the Vivalto multibody model.

MBS body	Mass kg	Roll Inertia kgm^2	Pitch Inertia kgm^2	Yaw Inertia kgm^2
Car body	50935	128118	2911166	2811166
Bogie frame	2470	1890	2014	3737
Wheelset	1410	866	101	866

Related to the primary suspensions, each axlebox has two slots which house a pair

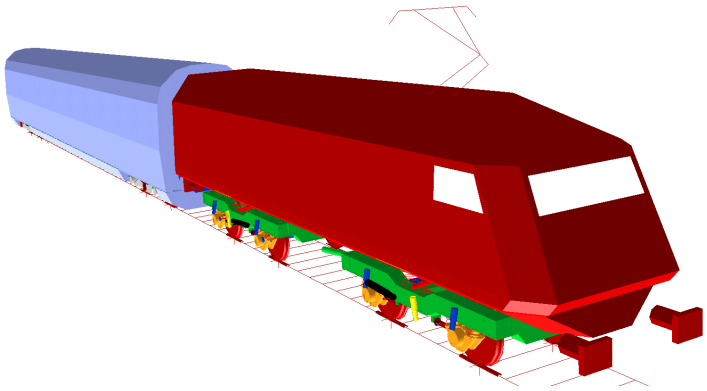

Figure 3.12: Global view of the Vivalto train multibody model.

of coil springs and two sheaths where the device responsible for the transmission of longitudinal and lateral forces is inserted (Fig. 3.14). This device has two pins attached to the bogie frame; each of these pins is coaxial with respect to the coil spring and transmits the forces by means of rubber cylindrical elements conveniently patterned. The vertical relative displacements are allowed through an adapter sleeve which can slide with respect to the internal surface, while it is fixed to the external cylindrical surface of the rubber elements. The solution allows the vertical forces to be exchanged between the coil springs and the bogie frame without the involvement of the adapter sleeves; the tractive, braking and lateral forces are instead transmitted by means of the rubber elements. These rubber elements are not axial-symmetric to provide different stiffness values in the lateral and longitudinal direction.

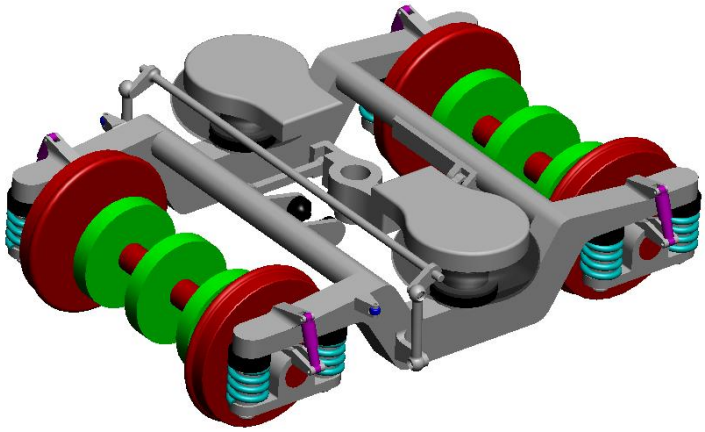

Figure 3.13: Multibody model of the SF-400 bogie.

The equivalent vertical stiffness of the primary suspension is given by the serial combination of the coil spring and a rubber. The maximum limit of the compression stroke is not given by the presence of a vertical bumpstop, but simply by the same spirals of the coil spring which, in conditions of maximum load, coming into contact between them and the coil spring behaves practically as a rigid body: in these extreme

conditions is the rubber element in series with the coil spring which absorbs the excessive stress due to metal-metal contact. The dumping is provided by a damper, whose characteristic is almost linear, the arrangement of which is not perfectly vertical to allow the damping of later motions between axlebox and bogie frame. The stiffness and dumping properties of the primary suspension stage are summarized in Tab. 3.6.

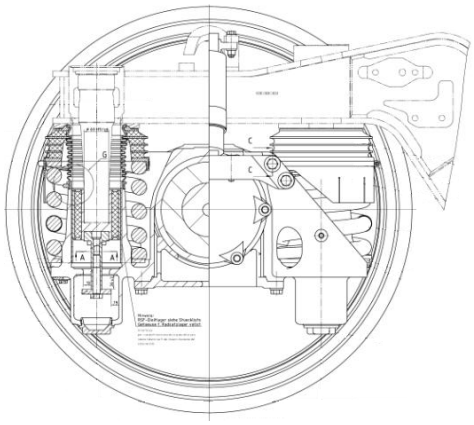

Figure 3.14: The Vivalto coach primary suspension.

Likewise to Minuetto, the vertical stiffness of the secondary suspension is provided with air springs to guarantee a constant height of the coach floor with respect to the top of rail, since in the full load condition the mass of coach is increased of 16 t. The air springs are fitted in series at two emergency springs which have the purpose to ensure the safety in deflated spring condition; in the multibody model a single spring with the characteristic given by the springs mounted in series has been considered.

Because of the unsatisfactory stiffness in lateral and longitudinal directions, other elements are required to complete the arrangement of the secondary suspension. The longitudinal tractive and braking forces between the bogie and the coach are transmitted through a system made up of a central pin for each bogie fixed to the coach; two rods and a rocker arm constitute a common "zeta" connection which constrain the pin to the bogie. In regard to the lateral displacement, they are limited by lateral bumpstops after a stroke of 20mm and are damped by the two viscous dampers which are fixed on one side to the rocker arm and on the other side to the internal flange of the bogie. A sufficient amount of roll stiffness is provided by the torsion bar (necessary because of the rise of the coach center of gravity due to the two passenger levels), while in the SF-400 bogie version used in Italian railway networks the anti-yaw damper are not present. The most interesting stiffness and damping characteristics of the secondary suspension stage are again shown in Tab. 3.6.

Even for the Vivalto, all the kinematic constraints and the force elements have been modeled as viscoelastic force elements, taking into account all the possible non linearities.

Table 3.6: Main stiffness and damping properties of the SF-400 bogie.

Primary suspension	k_x	5.50E+06 N/m
	k_y	2.43E+07 N/m
	k_z	5.0E+06 N/m
	c_x	1.2E+04 Ns/m
	c_y	9.0E+03 Ns/m
	c_z	2.0E+03 Ns/m
Secondary suspension	k_x	1.40E+05 N/m
	k_y	1.40E+05 N/m
	k_z	2.80E+05 N/m
	c_x	8.40E+02 Ns/m
	c_y	8.40E+02 Ns/m
	c_z	2.50E+04 Ns/m
	Anti-roll bar k_α	9.75E+05 Nm/rad
	Anti-roll bar c_α	1.0E+02 Nms/rad

The E.464 Multibody Model

The TRAXX 160 DCP, well known with the E.464 commercial name, is a set of light electric locomotives widely used as a traction unit in the passenger vehicles traveled on short and medium distances which operate for logistic reasons as blocked composition convoys. The physical and geometrical characteristics of this vehicle can be found in the literature [20][40] and its principal characteristics are presented in Tab. 3.7.

Table 3.7: Main characteristics of the E.464 locomotive.

Length	15.75 m
Width	3.11 m
Height	4.28 m
Bogie pivot distances	7.54 m
Bogie wheelbase	2.65 m
Unladen weight	72 t
Wheel arrangement	BoBo
Wheel diameter	1100 mm
Max tractive effort	200 kN
Max speed	160 km/h

As regard the vehicle structure, the E.464 have two bogies equipped with two suspension stages and characterized by standard technical arrangements such as two independent motorized axles (BoBo), hollow-shaft elastic transmission and traction bars in low position as can be seen in Fig. 3.15. In the multibody modeling the traction elements (motors, gearboxes and auxiliary organs) have been considered part of the frame bogie (Fig. 3.16); the main inertia properties for the vehicle implemented in the multibody model are shown in Tab. 3.8.

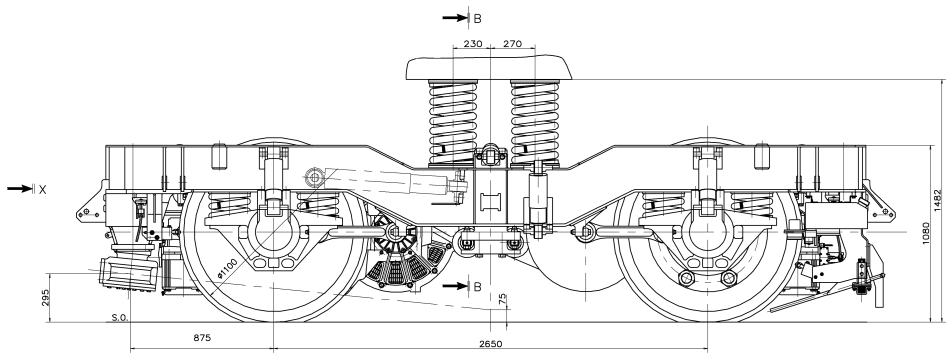

Figure 3.15: Lateral view of the E.464 bogie

Table 3.8: Inertia properties of the E.464 multibody model.

MBS body	Mass (kg)	Roll Inertia ($kg \cdot m^2$)	Pitch Inertia ($kg \cdot m^2$)	Yaw Inertia ($kg \cdot m^2$)
E.464 Coach	43000	61000	524700	524300
E.464 Bogie	10605	1735	6670	8224
E.464 Wheelset	1599	954	220	954

In the primary suspension arrangement, a SKF rocking axlebox is constrained to the bogie by means of two coil springs housed in two seats of the axlebox itself and through a linking arm, which is attached to the frame and the axlebox by means of two bushings. The stiffness in the relative vertical displacement is provided by the coil springs, while the higher longitudinal and lateral stiffnesses are due to the linking arm and the rubber elements. Finally the primary suspension stage includes a damper arranged in not perfectly vertical position, likewise in the Vivalto coach, to allow the damping of later motions between axlebox and bogie frame.

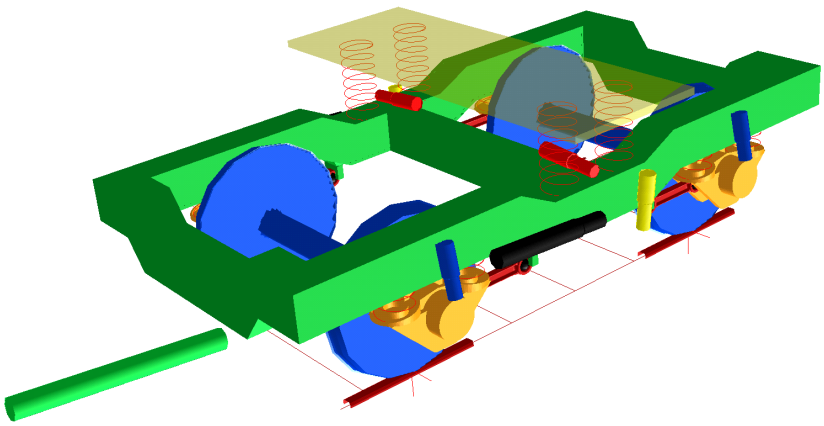

Figure 3.16: Bogie and suspension stages of the E.464 multibody model.

The secondary suspension stage first of all consist of four coil springs for each bogie and six non linear dampers (two verticals ones, two laterals ones and two anti-yaw ones) which provide the damping for vertical and lateral displacements as well as for

the yaw rotation. The coach is leaned on the four springs of the bogie without any intermediate beam. The longitudinal forces, as previously mentioned, are transmitted through the traction bars fitted in low position to reduce the vertical load transfers between the axles of the bogies; the bars are attached to the bogie and the coach by means of rubber elements.

Both the stages of suspensions have been modeled by means of three-dimensional viscoelastic force elements taking into account all the mechanical non linearities of the dampers. The main linear characteristics of the suspensions are shown in Tab. 3.9 while the nonlinear damper characteristics are imposed as a function of the velocity.

Table 3.9: Main stiffness properties of the E.464 bogie.

Primary suspension	Axlebox-frame link	k_{ax}	1.2E+07 N/m
		k_{rad}	8.5E+07 N/m
		k_{tors}	1.80E+03 Nm/rad
	Coil spring	k_x	1.73E+06 N/m
		k_y	1.73E+06 N/m
		k_z	8.52E+05 N/m
		k_α	2.0E+06 Nm/rad
		k_β	2.0E+06 Nm/rad
		k_γ	2.0E+06 Nm/rad
Secondary suspension	Coil spring	k_x	8.43E+04 N/m
		k_y	8.43E+04 N/m
		k_z	2.84E+05 N/m
		k_α	2.0E+06 Nm/rad
		k_β	2.0E+06 Nm/rad
		k_γ	2.0E+06 Nm/rad
	Traction rod	k_x	1.0E+07 N/m

3.2 The Global Contact Model

Dynamic simulations of railway vehicles need a reliable and efficient method to evaluate the contact points between wheel and rail, because their position has a considerable influence on both the direction and the magnitude of the contact forces. In this work a specific contact model has been considered instead of that implemented in Simpack Rail in order to improve reliability and accuracy of the contact points detection [3][27]. The proposed contact model is divided in two parts: the former detects the contact points by means of an innovative algorithm designed and validated by researchers of the Florence University [3][27], while the latter evaluates the global contact forces acting at the wheel-rail interface by means of Hertz's and Kalker's global theories [17][24][25].

3.2.1 The Contact Point Detection Algorithm

The algorithm for the contact points detection starts from the standard idea that the contact points make stationary the distance between the wheel and rail surfaces (see Fig. 3.17(a)); in more details the distance has a point of relative minimum if there is no penetration between the considered surfaces, while it has a relative maximum in the other case. The main features of the innovative algorithm are the following:

- it is a fully 3D model that takes into account all the six relative degrees of freedom (DOF) between wheel and rail;
- it is able to support generic railway tracks and generic wheel and rail profiles;
- it ensures a general and accurate treatment of the multiple contact without introducing simplifying assumptions on the problem geometry and kinematics and limits on the number of detected contact points;
- it ensures highly numerical efficiency making possible the online implementation within the commercial multibody software (Simpack - Rail, Adams - Rail) without look-up table; in this way also the numerical performances of the commercial multibody software are improved.

Two specific reference systems have to be introduced in order to simplify the model equations: the auxiliary one and the local one. The auxiliary system $O_r x_r y_r z_r$ is defined on the plane of the rails and follows the motion of the wheelset during the dynamic simulations: the x_r axis is tangent to the center line of the track in the origin O_r, the position of which is defined so that the $y_r z_r$ plane contains the center of mass $\mathbf{G}_w$ of the wheelset, while the z_r axis is perpendicular to plane of the rails. The local system $O_w x_w y_w z_w$ is rigidly connected to the wheelset (except for the rotation around its axis), its origin O_w coincides with the center of mass $\mathbf{G}_w$ of the wheelset, the x_w axis is parallel to the $x_r y_r$ plane and the y_w axis is coincident with the rotation axis of the wheelset (see Fig. 3.17(b)). In the following, for the sake of clarity, the variables referred to the local system will be marked with the apex w, while those referred to the auxiliary system with the apex r; the variables belonging to the wheel and to the rail will be indicated with the subscripts w and r respectively.

Thanks to these reference systems, the definition of the wheel and rail geometrical surfaces is very simple. In the local reference system the wheelset can be considered as a simple revolution surface around its axis y_w (see equation (3.2)); the generating function, indicated by $w(y_w)$, is supposed to be known (in this work, the profile ORE S1002 for a single wheel has been chosen (see Fig. 3.18)). Similarly the track can be locally described in the auxiliary reference system as an extrusion surface along the

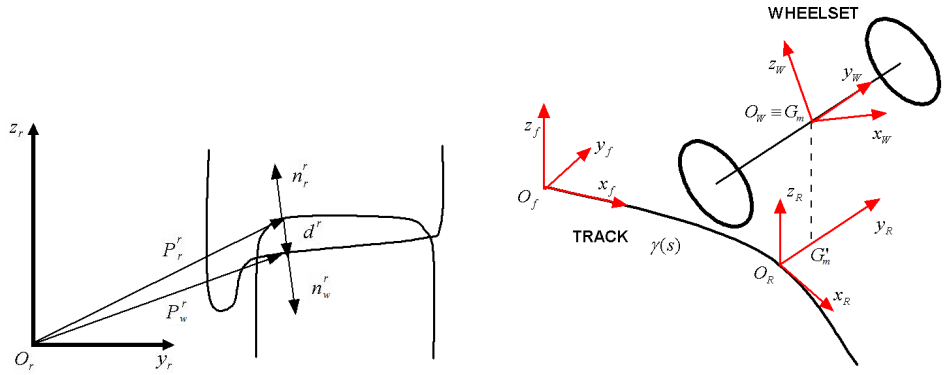

Figure 3.17: Distance method.

x_r axis (see equation (3.3)); the generating function, indicated by $r(y_r)$, is known (the profile UIC 60, with laying angle α_p equal to 1/20 rad, has been chosen for a single rail (see Fig. 3.18)). With reference to Fig. 2.1, the global contact model can be thought of as a *black box* having the following inputs and outputs:

- **Inputs**: the kinematic variables evaluated by the multibody model, i.e. the position $\mathbf{O}_w^r$, the orientation matrix R_w^r, the absolute velocity $\dot{\mathbf{O}}_w^r$ and the absolute angular velocity $\boldsymbol{\omega}_w^r$ of the *wheel system* and the analogous quantities of the *rail system* $\mathbf{O}_r^r = \mathbf{0}$, $R_r^r = I$, $\dot{\mathbf{O}}_r$ and $\boldsymbol{\omega}_r^r$;
- **Outputs**: the global contact variables relative to the wheel-rail interface, like the positions $\mathbf{P}_w^r$ and $\mathbf{P}_r^r$ of the contact points, the contact forces (the normal component N^r and the tangential components T_x^r and T_y^r), the global creepages ε_x, ε_y and ε_{sp} and the contact patch's dimensions a, b.

The distance method algorithm (see Fig. 3.17(a)) is based on a classical formulation of the contact problem in multibody field:

$$\mathbf{n}_r^r(\mathbf{P}_r^r) \wedge \mathbf{n}_w^r(\mathbf{P}_w^r) = \mathbf{n}_r^r(\mathbf{P}_r^r) \wedge R_w^r \mathbf{n}_w^w(\mathbf{P}_w^w) = \mathbf{0} \tag{3.1a}$$

$$\mathbf{n}_r^r(\mathbf{P}_r^r) \wedge \mathbf{d}^r = \mathbf{0} \tag{3.1b}$$

where:

- $\mathbf{P}_w^w$ and $\mathbf{P}_r^r$ are the positions of the generic points on the wheel surface and on the rail surface expressed in their reference systems:

$$\mathbf{P}_w^w(x_w, y_w) = \left(\begin{array}{ccc} x_w & y_w & -\sqrt{w(y_w)^2 - x_w^2} \end{array} \right)^T \tag{3.2}$$

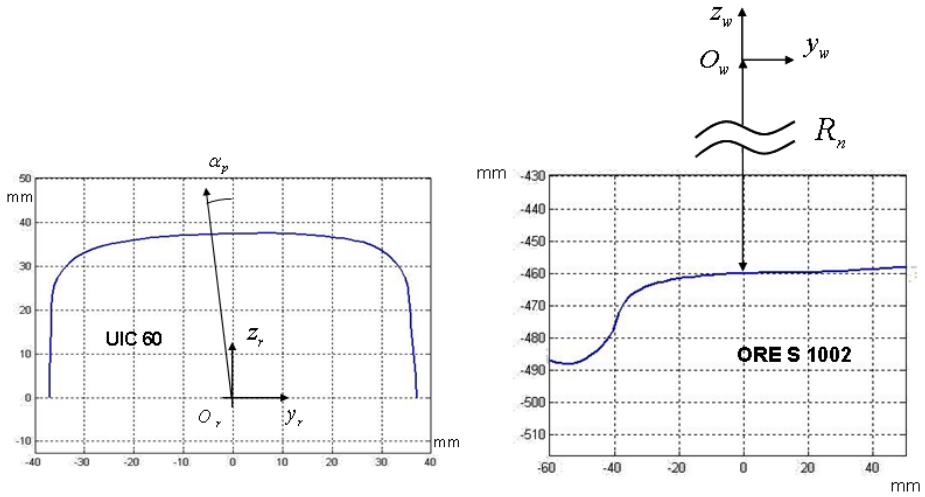

Figure 3.18: Wheel and rail profiles.

$$\mathbf{P}_r^r(x_r,y_r) = \begin{pmatrix} x_r & y_r & r(y_r) \end{pmatrix}^T ; \tag{3.3}$$

- $\mathbf{n}_w^w$ and $\mathbf{n}_r^r$ are the outgoing normal unit vectors to the wheel and rail surface respectively and are defined as follows:

$$\mathbf{n}_w^w(\mathbf{P}_w^w) = \frac{-\dfrac{\partial \mathbf{P}_w^w}{\partial x_w} \wedge \dfrac{\partial \mathbf{P}_w^w}{\partial y_w}}{\left\| \dfrac{\partial \mathbf{P}_w^w}{\partial x_w} \wedge \dfrac{\partial \mathbf{P}_w^w}{\partial y_w} \right\|} \quad , \quad \mathbf{n}_r^r(\mathbf{P}_r^r) = \frac{\dfrac{\partial \mathbf{P}_r^r}{\partial x_r} \wedge \dfrac{\partial \mathbf{P}_r^r}{\partial y_r}}{\left\| \dfrac{\partial \mathbf{P}_r^r}{\partial x_r} \wedge \dfrac{\partial \mathbf{P}_r^r}{\partial y_r} \right\|} \quad ; \tag{3.4}$$

- R_w^r is the rotation matrix that links the local reference system to the auxiliary one;

- $\mathbf{d}^r$ is the distance vector between two generic points on the wheel surface and on the rail surface (both referred to the auxiliary system) and it is equal to:

$$\mathbf{d}^r(x_w,y_w,x_r,y_r) = \mathbf{P}_w^r(x_w,y_w) - \mathbf{P}_r^r(x_r,y_r) \tag{3.5}$$

  where $\mathbf{P}_w^r$ is the position of the generic point of the wheel surface expressed in the auxiliary system:

$$\mathbf{P}_w^r(x_w,y_w) = \mathbf{O}_w^r + R_w^r \mathbf{P}_w^w(x_w,y_w). \tag{3.6}$$

The first condition (equation (3.1a)) of the system (3.1) imposes the parallelism between the normal unit vectors, while the second one (equation (3.1b)) requires the parallelism between the normal unit vector to the rail surface and the distance vector. Alternatively, other classical formulations of the contact problem can be used, by example imposing the orthogonality between the $\mathbf{d}^r$ vector and the tangential planes to

the wheel and rail surfaces (respectively π_w and π_r); however this approach leads to more complex and less manageable calculations and for this reason has not be adopted.

The system (3.1) consists of six nonlinear equations in the unknowns (x_w,y_w,x_r,y_r) (only four equations are independent and therefore the problem is 4D). However it is possible to express three of the four variables (in this case (x_w,x_r,y_r)) as a function of y_w, reducing the original 4D problem to a simple 1D scalar equation.

The reduction of the problem dimension using appropriate analytical procedures is the most innovative aspect of the proposed method. Moreover the exact analytical procedures do not introduce simplifying hypotheses for the contact problem resolution, increasing the accuracy and the numerical efficiency of the contact model; therefore it is possible to get much closer to the limit condition of conformal contact (with respect to the other contact models) without particular numerical problems and instabilities. At the same time, in case of conformal contact, finite element (FE) contact models that guarantee the suitable accuracy can be considered to overcome this issue [28][29]; these FE contact models, specially developed for the railway field, ensure an high numerical efficiency too.

In particular the second component of equation (3.1a) leads to the following equation:

$$r_{13}\sqrt{w(y_w)^2 - x_w^2} = r_{11}x_w - r_{12}w(y_w)w'(y_w) \tag{3.7}$$

where r_{ij} are the elements of the R_w^r matrix. Calling $A = r_{13}$, $B = w\Big(y_w\Big)$, $C = r_{11}$ and $D = r_{12}w\Big(y_w\Big)w'\Big(y_w\Big)$, the previous equation becomes:

$$A\sqrt{B^2 - x_w^2} = Cx_w - D. \tag{3.8}$$

Hence, removing the radical and solving for x_w:

$$x_{w1,2}(y_w) = \frac{CD \pm \sqrt{C^2D^2 - (A^2 + C^2)(D^2 - A^2B^2)}}{A^2 + C^2}; \tag{3.9}$$

as can be seen, there are two possible values of x_w for each y_w.

From the first component of the equation (3.1a) the following relation for $r'(y_r)$ holds:

$$r'(y_r)_{1,2} = \frac{r_{21}x_{r1,2}(y_w) - r_{22}w(y_w)w'(y_w) - r_{23}\sqrt{w(y_w)^2 - x_{w1,2}(y_w)^2}}{r_{32}w(y_w)w'(y_w) + r_{33}\sqrt{w(y_w)^2 - x_{w1,2}(y_w)^2}}. \tag{3.10}$$

If $r'(y_r)_{1,2}$ is a decreasing monotonous function (considering separately the sides of the track), equation (3.10) is numerically invertible and a single pair $y_{r1,2}(y_w)$ exists for each y_w value; otherwise the numerical inversion is still possible but will produce a further multiplication of the solution number.

By the second component of equation (3.1b) the expression of $x_{r1,2}(y_w)$ can be obtained:

$$x_{r1,2}(y_w) = r_{11}x_{w1,2}(y_w) + r_{12}y_w - r_{13}\sqrt{w(y_w)^2 - x_{w1,2}(y_w)^2}. \tag{3.11}$$

Finally, replacing the variables $x_{w1,2}(y_w)$, $x_{r1,2}(y_w)$ and $y_{r1,2}(y_w)$ in the first component of equation (3.1b), the following 1D scalar equation can be written:

$$F_{1,2}(y_w) = -r'\left(G_{wz} + r_{32}y_w - r_{33}\sqrt{w^2 - {x_{w1,2}}^2} - r\right) - \left(G_{wy} + r_{21}x_{w1,2} + r_{22}y_w - r_{23}\sqrt{w^2 - {x_{w1,2}}^2} - y_{r1,2}\right) = 0 \tag{3.12}$$

where G_{wx}, G_{wy}, G_{wz} are the coordinates of the wheelset center of mass in the auxiliary system. The expression (3.12) consists of two scalar equations in the variable y_w that can be easily solved with appropriate numerical algorithms.

The approach based on the reduction of the algebraic problem dimension presents several advantages that can be summarized as follows:

- the reduction of the algebraic problem dimension from 4D to 1D permits to obtain an high numerical efficiency that makes possible the online implementation of the new method within the multibody vehicle models without look-up table;
- the analytical approach assures an high degree of accuracy and generality;
- the 1D problem assures an easier management of the multiple solutions from an algebraic and a numerical point of view;
- in 1D problem also particularly elementary numerical algorithms like the grid method are quite efficient.

Thus, once obtained the generic solution (indicated with the subscript i) y_{wi} of equation (3.12), the complete solution (x_{wi}, y_{wi}, x_{ri}, y_{ri}) of the system (3.1) and consequently the contact points $\mathbf{P}^r_{wi} = \mathbf{P}^r_w(x_{wi},y_{wi})$ and $\mathbf{P}^r_{ri} = \mathbf{P}^r_r(x_{ri},y_{ri})$ can be found by substitution.

However, since the equations (3.1a) (3.1b) contain irrational terms, the generic solution (x_{wi}, y_{wi}, x_{ri}, y_{ri}) must satisfy the following analytical conditions:

- the solution must be real;
- the solution does not have to generate complex terms (that could be caused by the radicals in the equations);
- the solution must be an effective solution of the system (3.1) (check necessary because of the radical removal by squaring).

Furthermore, from a physical point of view, also the next checks must be evaluated:

- the multiple solutions obtained from the analytical resolution of equation (3.12) must be individuated and erased because they have no physical meaning;
- the following convexity conditions must be satisfied so that the contact is physically possible:

$$k_{1,wi} + k_{1,ri} > 0 \quad , \quad k_{2,wi} + k_{2,ri} > 0 \tag{3.13}$$

where $k_{1,wi}$, $k_{2,wi}$ are the normal curvatures of the wheel surface in longitudinal and lateral direction (referred to the auxiliary system and evaluated in the i-th contact point (x_{wi}, y_{wi}, x_{ri}, y_{ri})) while $k_{1,ri}$, $k_{2,ri}$ are the analogous quantities for the rail surface. Because of the problem geometry, the first one of equation (3.13) is always satisfied and thus only the second one must be verified (see Fig. 3.19);

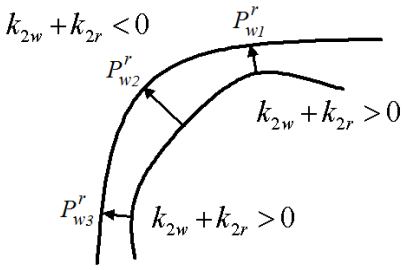

Figure 3.19: Convexity conditions.

- the generic solution of the system (3.1) can be an effective contact point only if the normal penetration $\tilde{p}_n$ between the surfaces of wheel and rail is negative (according to the adopted convention), i.e. there must be effective penetration between the bodies:

$$\tilde{p}_{ni} = \mathbf{d}_i^r \bullet \mathbf{n}_r^r(\mathbf{P}_{ri}^r) = -\mathbf{d}_i^r \bullet \mathbf{n}_w^r(\mathbf{P}_{wi}^r) < 0. \tag{3.14}$$

3.2.2 The Contact Forces Evaluation

At this point, for each contact point detected, the global creepages $\boldsymbol{\varepsilon}$ acting in the contact patch and the normal N^r and tangential $\mathbf{T}^r$ contact forces are determined (see Fig. 3.20) [17][24][25].
The normal forces N^r (expressed in the auxiliary system) are calculated by means of Hertz's theory [17]:

$$N^r = \left[-k_h|\tilde{p}_n|^\gamma + k_v\,|v_n|\,\frac{sign\,(v_n)-1}{2}\right]\frac{sign\,(\tilde{p}_n)-1}{2} \tag{3.15}$$

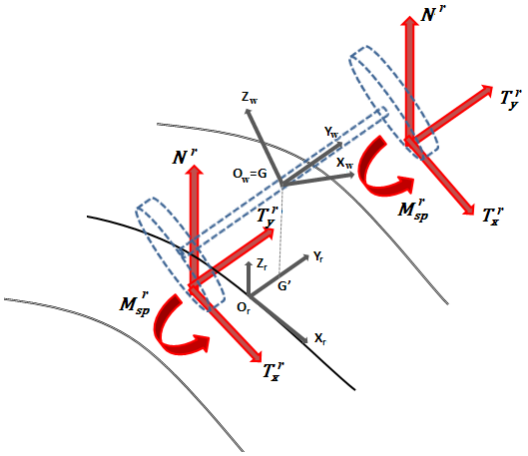

Figure 3.20: Global forces acting at wheel and rail interface.

where:

- $\tilde{p}_n$ is the normal penetration defined by equation (3.14);
- γ is the Hertz's exponent equal to 3/2;
- k_v is the contact damping constant ($k_v = 10^5 Ns/m$);
- $v_n = \mathbf{V} \bullet \mathbf{n}_r^r$ is the normal penetration velocity ($\mathbf{V}$ is the velocity of the contact point rigidly connected to the wheelset);
- k_h is the hertzian constant, function both of the material properties and of the geometry of the contact bodies (curvatures and semiaxes of the contact patch) [22].

The global creepages $\boldsymbol{\varepsilon}$ (longitudinal ε_x, lateral ε_y and spin creepage ε_{sp}) are calculated as follows:

$$\varepsilon_x = \frac{\mathbf{V} \bullet \mathbf{i}_r}{\left\|\dot{\mathbf{O}}_w^r\right\|}, \quad \varepsilon_y = \frac{\mathbf{V} \bullet \mathbf{t}_r^r\left(\mathbf{P}_r^r\right)}{\left\|\dot{\mathbf{O}}_w^r\right\|}, \quad \varepsilon_{sp} = \frac{\boldsymbol{\omega}_w^r \bullet \mathbf{n}_r^r\left(\mathbf{P}_r^r\right)}{\left\|\dot{\mathbf{O}}_w^r\right\|} \tag{3.16}$$

where $\mathbf{V}$ is the velocity of contact point rigidly connected to the wheelset, $\dot{\mathbf{O}}_w^r$ is the wheelset center of mass velocity (taken as the reference velocity for the calculation of the global creepages), $\boldsymbol{\omega}_w^r$ is the angular velocity of the wheelset expressed in the auxiliary system, $\mathbf{i}_r$ is the unit vector in longitudinal direction of the auxiliary system and $\mathbf{t}_r^r$ is the tangential unit vector to the rail profile.

The tangential contact forces $\tilde{T}_x^r$, $\tilde{T}_y^r$ and the spin torque M_{sp}^r (expressed in the auxiliary system) are calculated by means of the Kalker's global theory:

$$\tilde{T}_x^r = -f_{11}\varepsilon_x, \quad \tilde{T}_y^r = -f_{22}\varepsilon_y - f_{23}\varepsilon_{sp}, \quad M_{sp}^r = f_{23}\varepsilon_y - f_{33}\varepsilon_{sp} \tag{3.17}$$

where the coefficients f_{ij} are functions both of the materials and of the semiaxes of the contact patch:

$$f_{11} = abGC_{11}, \quad f_{22} = abGC_{22}, \quad f_{23} = (ab)^{3/2}GC_{23}, \quad f_{33} = (ab)^2GC_{33} \tag{3.18}$$

in which G is the wheel and rail combined shear modulus and C_{ij} are the Kalker's coefficients that can be found tabulated in the literature [25]. At this point, it is necessary to introduce a saturation on the tangential contact forces $\tilde{\mathbf{T}}^r = \begin{bmatrix} \tilde{T}_x^r & \tilde{T}_y^r \end{bmatrix}^T$ in order to consider the adhesion limit (not taken into account by the linear Kalker's theory):

$$\|\mathbf{T}^r\| \leq \mu_c N^r \tag{3.19}$$

where μ_c is the kinetic friction coefficient. Consequently the saturated tangential forces $\mathbf{T}^r$ will have the following expression:

$$\mathbf{T}^r = \epsilon \tilde{\mathbf{T}}^{\mathbf{r}} \tag{3.20}$$

in which the saturation coefficient ϵ can be evaluated as follows [19][37]:

$$\epsilon = \begin{cases} \dfrac{\mu_c N^r}{\tilde{T}^r}\left[\left(\dfrac{\tilde{T}^r}{\mu_c N^r}\right) - \dfrac{1}{3}\left(\dfrac{\tilde{T}^r}{\mu_c N^r}\right)^2 + \dfrac{1}{27}\left(\dfrac{\tilde{T}^r}{\mu_c N^r}\right)^3\right] & \text{if } \tilde{T}^r \leq 3\mu_c N^r \\ \dfrac{\mu_c N^r}{\tilde{T}^r} & \text{if } \tilde{T}^r > 3\mu_c N^r \end{cases} \tag{3.21}$$

where $\tilde{T}_r = \left\|\tilde{\mathbf{T}}^r\right\|$.

Chapter 4

The Wear Model

In this chapter the three phases of the wear model will be described in details: the local contact model[23][24][25], the evaluation of the amount of removed material [5][13] and the wheel and rail profile update. Finally the specific algorithm developed to treat together the wheel and rail wear evolution will be presented [42][43][44][48][49][50].

4.1 The Local Contact Model

The inputs of the wear model are the global contact parameters estimated by the vehicle model. Since a local wear computation is required, the global contact parameters need to be post-processed: the purpose of the local contact model is the calculation of the local contact variables (normal and tangential contact stresses p_n, $\mathbf{p}_t$ and local slips $\mathbf{s}$, all evaluated within the contact patch) starting from the corresponding global variables (contact points $\mathbf{P}_w^r$, $\mathbf{P}_r^r$, normal contact force N^r, global creepages $\boldsymbol{\varepsilon}$ and semiaxes of the contact patch a,b).

This model is based on the Kalker's local theory in the simplified version implemented in the algorithm FASTSIM; this algorithm contains an extremely efficient version (although necessarily approximate) of the Kalker theory and therefore is widely used in railway field [23].

For the local analysis a new reference system is defined at the wheel-rail interface on the contact plane (i.e. the common tangent plane between the wheel and rail surfaces): the x and y axes are the longitudinal and the transversal direction of the contact plane respectively (see Figs. 4.1-4.3). The algorithm is based on the proportionality hypothesis between the tangential contact stresses $\mathbf{p}_t$ and the elastic displacements $\mathbf{u}$, both evaluated within the contact patch:

$$\mathbf{u}(x,y) = L\mathbf{p}_t(x,y) \ , \ L = L(\boldsymbol{\varepsilon},a,b,G,\nu) \tag{4.1}$$

where the flexibility L (function of the global creepages $\boldsymbol{\varepsilon}$, the semiaxes of the contact patch a,b, the wheel and rail combined shear modulus G and the wheel and rail combined Poisson's ratio ν) can be calculated as follows:

$$L = \frac{|\varepsilon_x| L_1 + |\varepsilon_y| L_2 + c |\varepsilon_{sp}| L_3}{(\varepsilon_x^2 + \varepsilon_y^2 + c^2 \varepsilon_{sp}^2)^{1/2}} \tag{4.2}$$

with $L_1 = 8a/(3GC_{11})$, $L_2 = 8a/(3GC_{22})$, $L_3 = \pi a^2/(4GcC_{23})$ and $c = \sqrt{ab}$ (the constants C_{ij}, functions both of the Poisson's ratio ν and of the ratio a/b, are the Kalker's parameters and can be found in literature [23]).

The local slips $\mathbf{s}$ can be calculated by derivation considering both the elastic creepages and the rigid ones:

$$\mathbf{s}(x,y) = \dot{\mathbf{u}}(x,y) + V \begin{pmatrix} \varepsilon_x \\ \varepsilon_y \end{pmatrix} \tag{4.3}$$

where $V = \left\| \dot{\mathbf{O}}_w^r \right\|$ is the longitudinal vehicle speed. At this point it is necessary to discretize the elliptical contact patch in a grid of points in which the quantities p_n, $\mathbf{p}_t$ and $\mathbf{s}$ will be evaluated. Initially the transversal axis (with respect to the motion direction) of the contact ellipse has been divided in $n_y - 1$ equal parts of magnitude $\Delta y = 2b/(n_y - 1)$ by means of n_y equidistant nodes. Then the longitudinal sections of the patch (long $2a(y) = 2a\sqrt{1 - y/b^2}$) have been divided in $n_x - 1$ equal parts of magnitude $\Delta x(y) = 2a(y)/(n_x - 1)$ by means of n_x equidistant nodes (see Fig. 4.1). Due to this strategy the longitudinal grid resolution is not constant but increases near the lateral edges of the ellipse, where the lengths $a(y)$ are smaller. This procedure provides more accurate results right next to the edges of the ellipse, where a constant resolution grid would generate excessive numerical noise. The values of the n_x and n_y parameters have to assure the right balance between precision and computational load; good values of compromise are in the range $\begin{bmatrix} 25 & 50 \end{bmatrix}$.

Once the contact patch is discretized, the FASTSIM algorithm allows the iterative evaluation of both the contact stresses value p_n, $\mathbf{p}_t$ and the local slips $\mathbf{s}$ in order to divide the contact patch in adhesion and slip zone. Indicating the generic point of the grid with (x_i,y_j), $1 \leq i \leq n_x$ $1 \leq j \leq n_y$, the normal contact pressure can be expressed as:

$$p_n(x_i,y_j) = \frac{3}{2} \frac{N^r}{\pi ab} \sqrt{1 - \frac{x_i^2}{a^2} - \frac{y_j^2}{b^2}} \tag{4.4}$$

where N^r is the normal contact force, while the limit adhesion pressure $\mathbf{p}_A$ is:

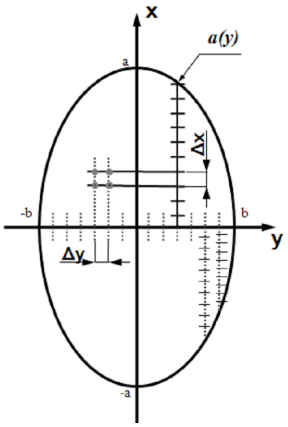

Figure 4.1: Contact patch discretization.

$$\mathbf{p}_A(x_i,y_j) = \mathbf{p}_t(x_{i-1},y_j) - \begin{pmatrix} \varepsilon_x \\ \varepsilon_y \end{pmatrix} \frac{\Delta x(y_j)}{L}; \tag{4.5}$$

thus, knowing the variable values in the point (x_{i-1},y_j), it is possible to pass to the point (x_i,y_j) as follows:

$$\text{if} \quad \|\mathbf{p}_A(x_i,y_j)\| \leq \mu p_n(x_i,y_j) \quad \Rightarrow \quad \begin{cases} \mathbf{p}_t(x_i,y_j) = \mathbf{p}_A(x_i,y_j) \\ \mathbf{s}(x_i,y_j) = \mathbf{0} \end{cases} \tag{4.6a}$$

$$\text{if} \quad \|\mathbf{p}_A(x_i,y_j)\| > \mu p_n(x_i,y_j) \quad \Rightarrow \quad \begin{cases} \mathbf{p}_t(x_i,y_j) = \frac{\mu p_n(x_i,y_j)\mathbf{p}_A(x_i,y_j)}{\|\mathbf{p}_A(x_i,y_j)\|} \\ \mathbf{s}(x_i,y_j) = \frac{LV}{\Delta x(y_j)} \left(\mathbf{p}_t(x_i,y_j) - \mathbf{p}_A(x_i,y_j)\right) \end{cases} \tag{4.6b}$$

where μ is the static friction coefficient; equations (4.6a) and (4.6b) hold respectively in the adhesion and slip zone.

Iterating the procedure for $2 \leq i \leq n_x$ and successively for $1 \leq j \leq n_y$ and assuming as boundary conditions $\mathbf{p}_t(x_1,y_j) = \mathbf{0}$, $\mathbf{s}(x_1,y_j) = \mathbf{0}$ for $1 \leq j \leq n_y$ (i.e. stresses and creepages zero out of the contact patch), the desired distribution of $p_n(x_i,y_j)$, $\mathbf{p}_t(x_i,y_j)$ and $\mathbf{s}(x_i,y_j)$ can be determined.

4.2 The Wear Evaluation

To evaluate the distribution of removed material on wheel and rail due to wear an experimental relationship between the volume of removed material and the frictional work [5][13] has been used.

The adopted wear function employs the local normal p_n and tangential $\mathbf{p}_t$ stresses (expressed in N/mm^2), the local slips $\mathbf{s}$ (m/s) and the vehicle velocity V (m/s) as inputs to directly compute the specific volume of worn material $\delta_{P^j_{wi}(t)}(x,y)$ and $\delta_{P^j_{ri}(t)}(x,y)$

(where x and y indicate the coordinates of a generic point of the contact patch as can be seen in Fig. 4.1) related to the i-th contact points $P_{wi}^{j}(t)$ and $P_{ri}^{j}(t)$ on the j-th wheel and rail pair (where $1 \leq i \leq N_{PDC}$ and $1 \leq j \leq N_w$ with N_{PDC} the maximum number of contact points of each single wheel-rail pair and with N_w the vehicle wheels number) for unit of distance traveled by the vehicle (expressed in m) and for unit of surface (expressed in mm^2). More specifically, local contact stresses and slips are used to evaluate the *wear index* I_W (expressed in N/mm^2), which represents the frictional power (expressed in N m) per unit of contact area (mm^2) and per unit of rolled distance (expressed in m) generated by the tangential contact stresses:

$$I_W = \frac{\mathbf{p}_t \bullet \mathbf{s}}{V}. \tag{4.7}$$

This index can be correlated with the *wear rate* K_W, that is the mass of removed material (expressed in $\mu g/(m\,mm^2)$) for unit of distance traveled by the vehicle and for unit of surface. The correlation is based on real data available in literature [2][5][35][36], which have been acquired from experimental wear tests carried out in the case of metal to metal contact using a twin disc test arrangement. The test discs are hydraulically loaded together and driven at controlled rotational speed by independent electric motors; shaft encoders monitor the speeds continuously. A torque transducer is assembled on one of the drive shafts and a load cell is mounted beneath the hydraulic jack. The slip ratio required is achieved by adjustment of the rotational speeds. These tests were carried out under dry condition without lubrication (resulting in a frictional coefficient of 0.45-0.50) considering the coupling between discs made of R8T steel for the wheel and UIC60 900A steel for the rail [5][16][35][36] and measuring the mass loss during the tests; the considered couple of material is widely used in Europe and Italian Railways and also for the vehicles and the tracks analyzed in this research.

The experimental relationship between K_W and I_W is shown in Fig. 4.2.

In order to provide wear coefficients to use in the wheel and rail wear modeling procedure the wear rate data was split into three regions (see Fig. 4.2(b)). A wear coefficient was defined for each of these regions [5][35][36]:

$$K_W(I_W) = \begin{cases} 5.3 * I_W & I_W < 10.4 \\ 55.1 & 10.4 \leq I_W \leq 77.2 \\ 61.9 * I_W - 4778.7 & I_W > 77.2. \end{cases} \tag{4.8}$$

Because of the lack of experimental data generated in the third regime, there may be the possibility of less accurate wear predictions for contacts at these conditions. However the wheel-rail contact is in K_{W1} and K_{W2} regions most if not all of the time and only reaches K_{W3} region in the most severe curves.

From a physical viewpoint [5][35][36], at low I_W oxidative wear was seen to occur on

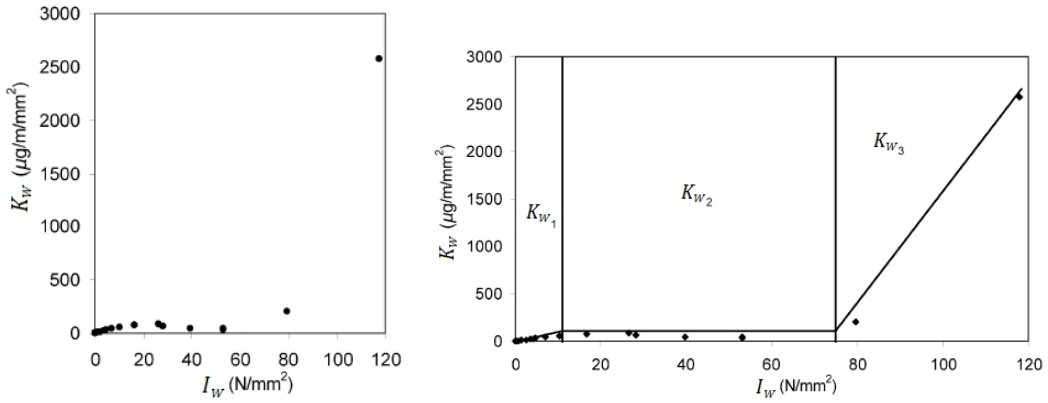

(a) Experimental data. (b) Wear regimes.

Figure 4.2: Trend of the *wear rate* K_W [5][35][36].

both wheel and rail discs. At the surfaces the oxide layer is just visible and there is a very small amount of deformation just below the wear surface of the discs. As I_W was increased, the wear mechanism altered and the wheel material appeared to wearing by a delamination process. A larger amount of plastic deformation was occurring below the wheel disc wear surface and crack formation just below the surface was visible which was leading to thin slivers of material breaking away from the surface. Finally as I_W was increased further these cracks were seen to alter direction from running parallel to the wear surface and turning up to turning down into the material causing larger chunks of material to break away. The wear features and mechanisms are discussed in greater detail in [5][35][36].

Since in this research activity a local wear model is developed, the wear law 4.8 is used in a local version, relating directly the tangential contact stresses (see the expression of I_W) with the amount of removed material due to wear (see the definition of K_W).

Once the wear rate $K_W(I_W)$ is known (the same both for the wheel and for the rail), the specific volume of removed material on the wheel and on the rail (for unit of distance traveled by the vehicle and for unit of surface) can be calculated as follows (expressed in $\mathrm{mm}^3/(\mathrm{m\,mm}^2)$):

$$\delta_{P^j_{wi}(t)}(x,y) = K_W(I_W)\frac{1}{\rho} \tag{4.9}$$

$$\delta_{P^j_{ri}(t)}(x,y) = K_W(I_W)\frac{1}{\rho} \tag{4.10}$$

where ρ is the material density (expressed in $\mathrm{kg/m}^3$).

4.3 The Profile Update Procedure

After obtaining the amount of worn material, wheel and rail profiles need to be updated to be used as the input of the next step of the whole model. The new profiles, denoted by $w_n(y_w)$ and $r_n(y_r)$, are computed from the old ones $w_o(y_w)$, $r_o(y_r)$ and from all the calculated distributions $\delta_{P^j_{wi}(t)}(x,y)$ and $\delta_{P^j_{ri}(t)}(x,y)$ of worn material through an appropriate set of numerical procedures that defines the update strategy. A suitable update strategy is also necessary both to remove the numerical noise that characterizes the distributions $\delta_{P^j_i(t)}(x,y)$ and that, due to non physical alterations of the new profiles, can cause problems to the global contact model and to mediate the distributions $\delta_{P^j_i(t)}(x,y)$ in order to obtain a single mean profile both for the wheel and for the rail as output of the wear model.

The whole numerical procedure which computes the new profiles can be summed up in the following steps:

- *Longitudinal integration*:

$$\frac{1}{2\pi w(y^j_{wi})}\int_{-a(y)}^{+a(y)} \delta_{P^j_{wi}(t)}(x,y)dx = \delta^{tot}_{P^j_{wi}(t)}(y) \tag{4.11}$$

$$\frac{1}{l_{sim}}\int_{-a(y)}^{+a(y)} \delta_{P^j_{ri}(t)}(x,y)dx = \delta^{tot}_{P^j_{ri}(t)}(y) \tag{4.12}$$

  where $a(y)$ is the longitudinal length of the contact patch (evaluated in y) (see Fig. 4.1), $w(y^j_{wi})$ is the wheel radius evaluated in y^j_{wi} and l_{sim} is the length of the simulated track (when the complete railway track of length l_{track} is simulated $l_{sim} = l_{track}$, while in the statistical analysis case $l_{sim} = l_{ct}$ with l_{ct} equal to the length of each of the N_c curved tracks). This first integration sums, in the longitudinal direction, all the wear contributes inside the contact path and averages this quantity over the whole longitudinal development of the wheel and of the rail (by means of the factors $1/2\pi w(y^j_{wi})$ and $1/l_{sim}$); in other words it provides the mean value of removed material (expressed in $\mathrm{mm}^3/(\mathrm{m\,mm}^2)$). The difference between the terms $1/l_{sim}$ and $1/2\pi w(y^j_{wi})$ (with the track length much greater than the wheel circumference length) is the main cause that leads the wheel to wear much faster than the rail and consequently to a different scale of magnitude of the two investigated phenomena. It reflects the real physical behavior where the life of the rail is much greater than that of the wheel.

- *Track integration*:

$$\int_{T_{in}}^{T_{end}} \delta^{tot}_{P^j_{wi}(t)}(y)V(t)dt \approx \int_{T_{in}}^{T_{end}} \delta^{tot}_{P^j_{wi}(t)}(s_w - s^{cj}_{wi}(t))V(t)dt = \Delta_{P^j_{wi}}(s_w) \tag{4.13}$$

$$\int_{T_{in}}^{T_{end}} \delta^{tot}_{P^j_{ri}(t)}(y)V(t)dt \approx \int_{T_{in}}^{T_{end}} \delta^{tot}_{P^j_{ri}(t)}(s_r - s^{cj}_{ri}(t))V(t)dt = \Delta_{P^j_{ri}}(s_r); \tag{4.14}$$

the track integration sums all the wear contributes of the dynamic simulation to obtain the depth of removed material for wheel $\Delta_{P^j_{wi}}(s_w)$ and rail $\Delta_{P^j_{ri}}(s_r)$ expressed in mm $=$ mm^3/mm^2. The introduction of the natural abscissas s_w and s_r of the curves $w(y_w)$ and $r(y_r)$ leads to a better accuracy in the calculation of the worn profiles. In particular the following relations locally hold (see Fig. 4.3):

$$y \approx s_w - s^{cj}_{wi}(t) \qquad\qquad y \approx s_r - s^{cj}_{ri}(t) \tag{4.15}$$

$$w(y_w) = w(y_w(s_w)) = \tilde{w}(s_w) \qquad\qquad r(y_r) = r(y_r(s_r)) = \tilde{r}(s_r) \tag{4.16}$$

where the natural abscissas of the contact points s^{cj}_{wi} and s^{cj}_{wi} can be evaluated from their positions P^j_{wi} and P^j_{ri}.

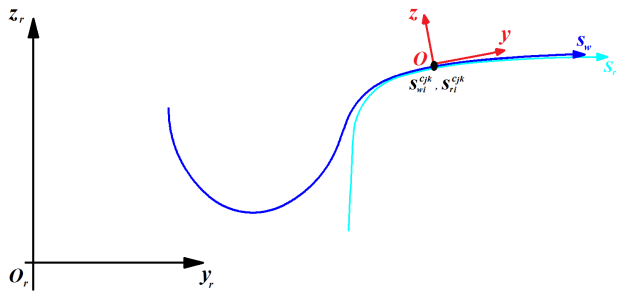

Figure 4.3: Normal abscissa for the wheel and rail profiles.

- *Sum on the contact points*:

$$\sum_{i=1}^{N_{PDC}} \Delta_{P^j_{wi}}(s_w) = \Delta^w_j(s_w) \tag{4.17}$$

$$\sum_{i=1}^{N_{PDC}} \Delta_{P^j_{ri}}(s_r) = \Delta^r_j(s_r) \tag{4.18}$$

where N_{PDC} is the maximum number of contact points of each single wheel (and respectively of each single rail). The number of active contact points changes during the simulation but it is always less than N_{PDC}; thus, the amount of worn material related to non-active contact points is automatically set equal to zero.

- *Average on the wheel-rail pairs*:

$$\frac{1}{N_w}\sum_{j=1}^{N_w} \Delta^w_j(s_w) = \overline{\Delta}^w(s_w) \tag{4.19}$$

$$\frac{1}{N_w}\sum_{j=1}^{N_w}\Delta_j^r(s_r) = \overline{\Delta}^r(s_r) \tag{4.20}$$

where N_w is the number of vehicle wheels. The average on the number of wheel-rail pairs has to be evaluated in order to obtain as output of the wear model a single average profile for both the wheel and the rail.

- *Average on the curved tracks of the statistical approach*: this step of the update procedure is important when a statistical description of the track is adopted. In this case different wear distributions $\overline{\Delta}_k^w(s_w)$ and $\overline{\Delta}_k^r(s_r)$ for each of the N_c curve classes will be obtained from the previous steps (with $1 \leq k \leq N_c$). At this point the statistical weights of the curve classes p_k, calculated as the ratio between the track length characterized by the curve conditions related to the k-th class (in terms of radius and superelevation values) and the total railway track length, have to be introduced to consider the frequency with which each curve appears on the actual railway track. Consequently for the statistical approach the following relationships hold:

$$\sum_{k=1}^{N_c} p_k\overline{\Delta}_k^w(s_w) = \overline{\Delta}_{stat}^w(s_w) \tag{4.21}$$

$$\sum_{k=1}^{N_c} p_k\overline{\Delta}_k^r(s_r) = \overline{\Delta}_{stat}^r(s_r) \tag{4.22}$$

with $\sum_{k=1}^{N_C} p_k = 1$ (see also the chapter 6). Obviously, when the dynamic simulations are performed on the complete railway track equations 4.21 and 4.22 simply become:

$$\overline{\Delta}^w(s_w) = \overline{\Delta}_{track}^w(s_w) \tag{4.23}$$

$$\overline{\Delta}^r(s_r) = \overline{\Delta}_{track}^r(s_r). \tag{4.24}$$

- *Scaling*:
since it normally takes traveled distance of thousands kilometers in order to obtain measurable wear effects, an appropriate scaling procedure is necessary to reduce the simulated track length with a consequent limitation of the computational effort. Hypothesizing the almost linearity of the wear model with the traveled distance inside the discrete steps (valid if the discretization step length km_{step} is small enough to consider the profile variation between two consequent steps negligible), it is possible to amplify the removed material during the dynamic simulations by means of a scaling factor which increases the distance traveled by the vehicle.

The almost linearity of the wear model inside the discrete steps km_{step} (in which the total mileage traveled km_{tot} is subdivided) is a working hypothesis coming from the discrete approach of the model. The linearity hypothesis is equivalent to suppose that the wear rate inside the simulated distance (km_{prove}) remains the same also inside the discrete step km_{step} (reasonable since the considered vehicle repeats the same railway track both during the simulated distance (km_{prove}) and during the discrete step (km_{step})).

In this work adaptive discrete steps (function of the wear rate and obtained imposing the threshold values D^w_{step} and D^r_{step} on the maximum of the removed material quantity on the wheelsets and on the tracks at each discrete step) have been chosen to update the wheel and rail profiles (see eq. 4.25-4.32 and Fig. 4.4): in fact this method well fits in following the behavior of the wear evolution that could present non linear characteristics outside of the discrete steps.

The evaluation of the discrete steps, with the consequent scaling of $\overline{\Delta}^w_{stat}(s_w)$, $\overline{\Delta}^w_{track}(s_w)$ and $\overline{\Delta}^r_{stat}(s_r)$, $\overline{\Delta}^r_{track}(s_r)$, represents the major difference between the update strategy of wheel and rail:

1. the removed material on the wheel due to wear is proportional to the distance traveled by the vehicle; in fact a point of the wheel is frequently in contact with the rail in a number of times proportional to the distance. The following nomenclature can been introduced (see Fig. 4.4):
   - km_{tot} is the total mileage traveled by the considered vehicle; its value can be chosen depending on the purpose of the simulations, for example according to the wheelset maintenance European standard [12];
   - km_{step} is the length of the discrete step corresponding to the threshold value on the wear depth D^w_{step};
   - km_{prove} is the overall mileage traveled by the vehicle during the dynamic simulations. This parameter assumes a different value according to the different way in which the track is treated: if the wear evolution is evaluated on the overall railway track (of length l_{track}) then $km^{track}_{prove} = l_{track}$ while, if the track statistical approach is considered, $km^{stat}_{prove} = l_{ct}$ is the mileage traveled by the vehicle during each of the N_c dynamic simulations. This consideration explains the deeply difference in terms of computational load between the two considered cases; in the statistical analysis one, the necessity of acceptable computational time for the multibody simulations, leads to adopt small values of the curve tracks length km^{stat}_{prove}, while in the total track one the km^{track}_{prove} value is imposed

by the real track length with an inevitable increase in computational time.

Finally the material removed on the wheels and the corresponding km_{step} value have to be scaled according to the following laws:

$$\overline{\Delta}^{w}_{stat}(s_w)\frac{D^{w}_{step}}{D^{w}_{stat}} = \overline{\Delta}^{w}_{stat}{}^{sc}(s_w), \quad km^{stat}_{step} = \frac{D^{w}_{step}}{D^{w}_{stat}} km^{stat}_{prove} \tag{4.25}$$

$$\overline{\Delta}^{w}_{track}(s_w)\frac{D^{w}_{step}}{D^{w}_{track}} = \overline{\Delta}^{w}_{track}{}^{sc}(s_w), \quad km^{track}_{step} = \frac{D^{w}_{step}}{D^{w}_{track}} km^{track}_{prove} \tag{4.26}$$

where:

$$D^{w}_{stat} = \max_{s_w} \overline{\Delta}^{w}_{stat}(s_w) \tag{4.27}$$

$$D^{w}_{track} = \max_{s_w} \overline{\Delta}^{w}_{track}(s_w). \tag{4.28}$$

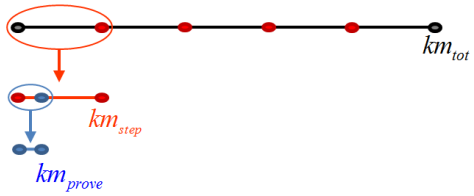

Figure 4.4: Discretization of the total mileage.

The choice of the spatial step km_{step} (and consequently of the threshold value D^{w}_{step}) must be a good compromise between numerical efficiency and the accuracy required by the wear model. A km_{step} too small compared to km_{tot} would provide accurate results but excessive calculation times; the contrary happens with km_{step} too big compared to km_{tot}.

2. the depth of rail wear is not proportional to the distance traveled by the vehicle; in fact the rail tends to wear out only in the zone where it is crossed by the vehicle and, increasing the traveled distance, the depth of removed material remains the same. On the other hand the rail wear is proportional to the total tonnage M_{tot} burden on the rail and thus to the total vehicle number N_{tot} moving on the track. Therefore, if N_{step} is the vehicle number moving in a discrete step, the quantity of rail removed material at each step will be:

$$\overline{\Delta}^{r}_{stat}(s_r)\frac{D^{r}_{step}}{D^{r}_{stat}} = \overline{\Delta}^{r}_{stat}{}^{sc}(s_r), \quad N^{stat}_{step} = \frac{D^{r}_{step}}{D^{r}_{stat}} N^{stat}_{prove} \tag{4.29}$$

$$\overline{\Delta}^{r}_{track}(s_r)\frac{D^r_{step}}{D^r_{track}} = \overline{\Delta}^{r}_{track}{}^{sc}(s_r), \quad N^{track}_{step} = \frac{D^r_{step}}{D^r_{track}} N^{track}_{prove} \tag{4.30}$$

where $N^{stat}_{prove} = N_c$, obviously $N^{track}_{prove} = 1$ and:

$$D^r_{stat} = \max_{s_r} \overline{\Delta}^{r}_{stat}(s_r) \tag{4.31}$$

$$D^r_{track} = \max_{s_r} \overline{\Delta}^{r}_{track}(s_r). \tag{4.32}$$

- *Smoothing of the removed material*:

$$\Im\left[\overline{\Delta}^{w}_{stat}{}^{sc}(s_w)\right] = \overline{\Delta}^{w}_{stat\,sm}{}^{sc}(s_w), \quad \Im\left[\overline{\Delta}^{w}_{track}{}^{sc}(s_w)\right] = \overline{\Delta}^{w}_{track\,sm}{}^{sc}(s_w) \tag{4.33}$$

$$\Im\left[\overline{\Delta}^{r}_{stat}{}^{sc}(s_r)\right] = \overline{\Delta}^{r}_{stat\,sm}{}^{sc}(s_r), \quad \Im\left[\overline{\Delta}^{r}_{track}{}^{sc}(s_r)\right] = \overline{\Delta}^{r}_{track\,sm}{}^{sc}(s_r); \tag{4.34}$$

the numerical noise and short spatial wavelengths without physical meaning that affect the worn material distributions can be passed to the new profiles $\tilde{w}^{stat}_n(s_w)$, $\tilde{w}^{track}_n(s_w)$ and $\tilde{r}^{stat}_n(s_r)$, $\tilde{r}^{track}_n(s_r)$ with consequent problems raising in the global contact model. Hence an appropriate smoothing of the worn material distributions is required. In this case it is achieved by means of a first-order discrete filter (i.e. a moving average filter with window size equal to $1\% \div 5\%$ of the total number of points in which the profiles are discretised); obviously the discrete filter has to conserve the mass.

- *Profile update:*

$$\begin{gathered}
\begin{pmatrix} y_w(s_w) \\ \tilde{w}^{stat}_o(s_w) \end{pmatrix} - \overline{\Delta}^{w}_{stat\,sm}{}^{sc}(s_w)\mathbf{n}^r_w \xrightarrow{re-parameterization} \begin{pmatrix} y_w(s_w) \\ \tilde{w}^{stat}_n(s_w) \end{pmatrix} \\
\begin{pmatrix} y_w(s_w) \\ \tilde{w}^{track}_o(s_w) \end{pmatrix} - \overline{\Delta}^{w}_{track\,sm}{}^{sc}(s_w)\mathbf{n}^r_w \xrightarrow{re-parameterization} \begin{pmatrix} y_w(s_w) \\ \tilde{w}^{track}_n(s_w) \end{pmatrix} \\
\begin{pmatrix} y_r(s_r) \\ \tilde{r}^{stat}_o(s_r) \end{pmatrix} - \overline{\Delta}^{r}_{stat\,sm}{}^{sc}(s_r)\mathbf{n}^r_r \xrightarrow{re-parameterization} \begin{pmatrix} y_r(s_r) \\ \tilde{r}^{stat}_n(s_r) \end{pmatrix} \\
\begin{pmatrix} y_r(s_r) \\ \tilde{r}^{track}_o(s_r) \end{pmatrix} - \overline{\Delta}^{r}_{track\,sm}{}^{sc}(s_r)\mathbf{n}^r_r \xrightarrow{re-parameterization} \begin{pmatrix} y_r(s_r) \\ \tilde{r}^{track}_n(s_r) \end{pmatrix};
\end{gathered} \tag{4.35}$$

the last step consists in the update of the old profiles $\tilde{w}^{stat}_o\Big(s\Big) = w^{stat}_o\Big(y\Big)$, $\tilde{w}^{track}_o\Big(s\Big) = w^{track}_o\Big(y\Big)$ and $\tilde{r}^{stat}_o\Big(s_r\Big) = r^{stat}_o\Big(y_r\Big)$, $\tilde{r}^{track}_o\Big(s_r\Big) = r^{track}_o\Big(y_r\Big)$ to ob-

tain the new profiles $\tilde{w}_n^{stat}\Big(s\Big) = w_n^{stat}\Big(y\Big)$, $\tilde{w}_n^{track}\Big(s\Big) = w_n^{track}\Big(y\Big)$ and $\tilde{r}_n^{stat}\Big(s_r\Big) = r_n^{stat}\Big(y_r\Big)$, $\tilde{r}_n^{track}\Big(s_r\Big) = r_n^{track}\Big(y_r\Big)$; since the removal of material occurs in the normal direction to the profiles ($\mathbf{n}_w^r$ and $\mathbf{n}_r^r$ are the outgoing unit vectors for the wheel and rail profiles respectively), once removed the quantities $\overline{\Delta}^{w\ \ sc}_{stat\,sm}(s_w)$, $\overline{\Delta}^{w\ \ sc}_{track\,sm}(s_w)$ and $\overline{\Delta}^{r\ \ sc}_{stat\,sm}(s_r)$, $\overline{\Delta}^{r\ \ sc}_{track\,sm}(s_r)$ a re-parameterization of the profiles is needed to obtain again curves parameterized by means of the curvilinear abscissa.

4.4 Simulation Algorithm

As explained in previous section 4.3, the wheel and rail wear evolutions evolve according to different time scales and a fully simulation of such events would require a too heavy computational effort. For this reason the following specific algorithm has been adopted for updating the profiles:

1. to have a good compromise between calculation times and result accuracy a suitable number of discrete steps both for the wheel and for the rail have been chosen, n_{sw} and n_{sr}:

   (a) consequently the wheel wear threshold D^w_{step} (see section 4.3) has to be fixed equal to a suitable value so to research a good compromise between numerical efficiency and model accuracy;

   (b) the value of the rail wear threshold D^r_{step} (see section 4.3) has to be fixed equal to a suitable value so to obtain an appreciable rail wear during the simulations.

2. the wear evolutions on wheel and rail must be decoupled because of the different scales of magnitude:

   (a) while the wheel wear evolves, the rail is supposed to be constant: in fact, in the considered time scale, the rail wear variation is negligible;

   (b) the time scale characteristic of the rail wear evolution, much greater than the wheel wear evolution one, causes the same probability that each discrete rail profile comes in contact with each possible wheel profile. For this reason, for each rail profile, the whole wheel wear evolution (from the original profile to the final profile) has been simulated.

Based on the two previous hypotheses, the simulations have been carried out according to the following strategy:

Wheel profile evolution at first rail step: w_i^0

$$p_{1,1}\left\{\begin{pmatrix} w_0^0 & r_0 \end{pmatrix} \rightarrow \begin{pmatrix} w_1^0 & r_0 \end{pmatrix} \rightarrow \ldots \rightarrow \begin{pmatrix} w_{n_{sw}-1}^0 & r_0 \end{pmatrix} \rightarrow w_{n_{sw}}^0\right.$$

Average on the rails $r_1^{(i+1)}$ for the calculation of the second rail step: r_1

$$p_{1,2}\left\{\begin{pmatrix} w_0^0 & r_0 \\ w_1^0 & r_0 \\ \vdots & \vdots \\ w_{n_{sw}-1}^0 & r_0 \end{pmatrix} \rightarrow \begin{pmatrix} r_1^{(1)} \\ r_1^{(2)} \\ \vdots \\ r_1^{(n_{sw})} \end{pmatrix} \rightarrow r_1\right.$$

$\vdots$

Wheel profile evolution at n_{sr} rail step: $w_i^{n_{sr}-1}$

$$p_{n_{sr},1}\left\{\begin{pmatrix} w_0^{n_{sr}-1} & r_{n_{sr}-1} \end{pmatrix} \rightarrow \begin{pmatrix} w_1^{n_{sr}-1} & r_{n_{sr}-1} \end{pmatrix} \rightarrow \ldots \rightarrow \begin{pmatrix} w_{n_{sw}-1}^{n_{sr}-1} & r_{n_{sr}-1} \end{pmatrix} \rightarrow w_{n_{sw}}^{n_{sr}-1}\right.$$

Average on the rails $r_{n_{sr}}^{(i+1)}$ for the calculation of the last rail step: $r_{n_{sr}}$

$$p_{n_{sr},2}\left\{\begin{pmatrix} w_0^{n_{sr}-1} & r_{n_{sr}-1} \\ w_1^{n_{sr}-1} & r_{n_{sr}-1} \\ \vdots & \vdots \\ w_{n_{sw}-1}^{n_{sr}-1} & r_{n_{sr}-1} \end{pmatrix} \rightarrow \begin{pmatrix} r_{n_{sr}}^{(1)} \\ r_{n_{sr}}^{(2)} \\ \vdots \\ r_{n_{sr}}^{(n_{sw})} \end{pmatrix} \rightarrow r_{n_{sr}}\right. \tag{4.36}$$

where w_i^j indicates the i-th step of the wheel profile that evolves on j-th step of the rail profile r_j (with $0 \leq i \leq n_{sw}-1$ and $0 \leq j \leq n_{sr}-1$). The initial profiles w_0^j are always the same for each j and correspond to the unworn wheel profile (ORE S1002).

Initially the wheel (starting from the unworn profile w_0^0) evolves on the unworn rail profile r_0 to produce the discrete wheel profiles w_0^0,w_1^0,...,$w_{n_{sw}}^0$ (step $p_{1,1}$). Then the virtual rail profiles $r_1^{(i+1)}$, obtained by means of the simulations (w_i^0,r_0), are arithmetically averaged so as to get the update rail profile r_1 (step $p_{1,2}$). This procedure can be repeated n_{sr} times in order to perform all the rail discrete steps (up to the step $p_{n_{sr},2}$).

The computational effort required by the simulation strategy is the following:

1. in the wheel wear study, for each update of the rail profile r_j (n_{sr} updates), the whole wheel wear loop w_i^j (n_{sw} steps of simulation) is simulated. The computational effort results of $n_{sw} \times n_{sr}$ steps both for the dynamic analysis (in Simpack Rail) and for the wear model necessary to calculate the removed material on the wheel (in Matlab).

2. in the rail wear study the dynamic analyses are the same of the previous case because for each rail step the wheel profiles w_i^j are simulated on r_j in order to obtain $r_j^{(i+1)}$ and thus the updated rail profile r_{j+1} by means of an arithmetic

mean. Therefore, no additional dynamical analyses are needed. In this case only the wear model steps $n_{sw} \times n_{sr}$ must be simulated so as to get the removed material on the rail.

Chapter 5

Wear Model Validation

This chapter deals with the description of the wear model validation phase [42][43] [44][49][50]. In the first part the Aosta-Pre Saint Didier track, on which the dynamic simulations of the DMU Aln 501 Minuetto vehicle have been performed, will be introduced. Then the control parameters capable of estimate the wear evolution on the wheel and rail will be defined; the flange height FH, the flange thickness FT, the flange steepness QR are the three parameters used for the wheel while an additional quota QM evaluates the rail wear [12][14]. Also the experimental data (provided by Trenitalia) measured on the Aosta-Pre Saint Didier track and their processing will be introduced [40]. In the second part of the chapter the results obtained with the wear model will be analyzed and compared with the experimental data so to validate the model.

5.1 The Aosta Pre-Saint Didier Line

The Aosta-Pre Saint Didier railway network is characterized by an approximate length of $l_{track} \approx 31$km and it is equipped with the standard track gauge (1435mm) (see Fig. 5.1). This is a very sharp line on the Italian Railways with a high percentage of curvilinear track equal almost to the 60% of the total length (see Fig. 5.1(a)); the overall altitude gap is about 430m with an average slope equal to 13.69‰ and picks up to 30‰. The very sharp scenario is rather interesting since the DMU Aln 501 Minuetto exhibits serious problems on this track in terms of wear, requiring frequent maintenance interventions on the wheelsets.

The whole network has been reconstructed and modeled in the Simpack environment starting from the track data provided by RFI.

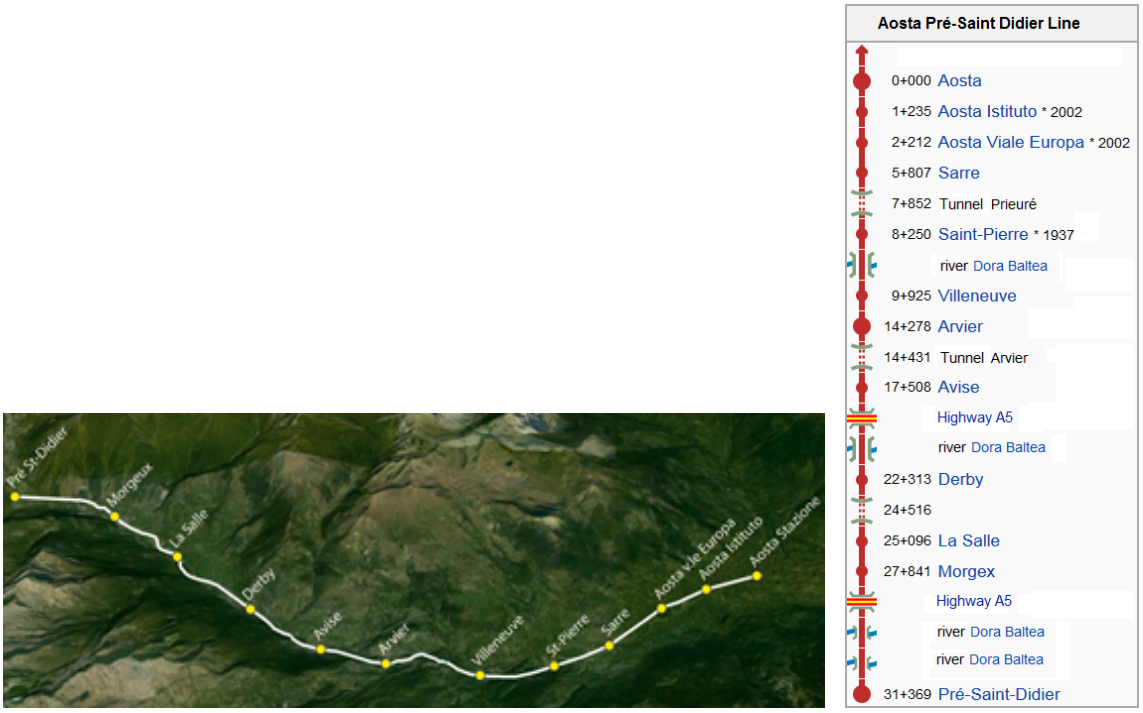

(a) (b)

Figure 5.1: Aosta Pre-Saint Didier railway network.

5.2 The Wear Control Parameters

The reference parameters FH, FT and QR are capable of estimating the wheel profile evolution due to wear without necessarily knowing the whole profile shape (see Fig. 5.2) [12]. According to these quotas the user will be able both to establish when the worn wheel profile will have to be re-profiled and to detect if the wear compromises the dynamical stability of the vehicle.

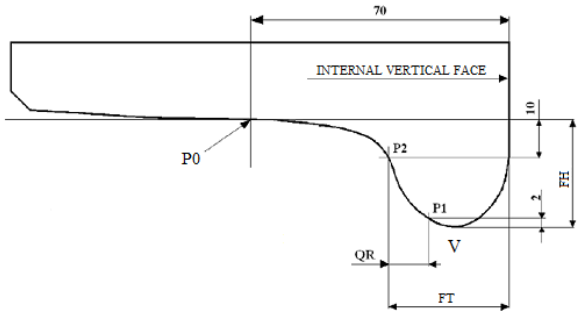

		$d \leq 630$	$630 < d \leq 760$	$760 < d$
FH	min	31.5	29.5	27.5
	max		36	
		$d \leq 760$	$760 < d \leq 840$	$840 < d$
FT	min	27.5	25	22
	max		33	
QR	min		6.5	

Figure 5.2: Reference dimensions of the wheel profile (left) and limit values in mm (right) for a wheel having an actual rolling diameter equal to d.

The procedure to define the wheel reference quotas is the following:

1. first of all the point $P0$ is defined on the profile, at 70mm from the internal vertical face of the wheel;

2. then the point $P1$ is introduced on the profile, 2mm above the flange vertex on the flange side;

3. finally the point $P2$ is determined on the profile, 10mm under the point $P0$ on the flange side;

4. the wear control parameters are then calculated as follows: the flange thickness FT is the horizontal distance between the internal vertical face and the point $P2$; the flange steepness QR is the horizontal distance between the points $P1$ and $P2$, while the flange height FH is the vertical distance between $P0$ and the flange vertex (all the distances are considered positive).

Because of the way the quotas are defined, they are positive and do not depend on the wheel rolling radius. The values of these parameters are measured periodically to decide whether the profile has to be re-turned or not (if it is still possible), considering the maximum or minimum values suggested by the current standard [12]; the quotas limit values are reported in Fig. 5.2.

As regards their physical meaning, both the flange thickness FT and the flange height FH describe the size of the flange: variations of the first quota are due to the action of the wear which progressively reduces the thickness of the flange and its structural resistance, while the rise of the flange height is a measure of the wear on the tread. Conversely, the QR dimension is a shape parameter which quantifies the local conicity on the flange. Although the performance in terms of dynamic behavior depend on the coupling between the wheel and rail profiles rather than just the wheel profile, the check of the reference quotas aims to guarantee an acceptable running behavior; in particular, the safety against the hunting in straight track at high speed and the derailment are of fundamental importance. The first phenomenon is enhanced by high values of equivalent conicity at the wheel-rail contact interface, while the second one can occur in case of worn wheel profile characterized by a low flange angle, which reduces, all other things being equal, the maximum allowable lateral force on wheel.

An additional control parameter is then introduced to evaluate the evolution of rail wear. Particularly the QM quota is defined as the rail head height in the point $y_r = 760$mm with respect to the center line of the track: this y_r value depends on the railway gauge (equal to 1435mm in the Aosta-Pre Saint Didier line) and on the laying angle α_p of the track (equal to 1/20rad). Physically the QM quota gives information on the rail head wear (see Fig. 5.3).

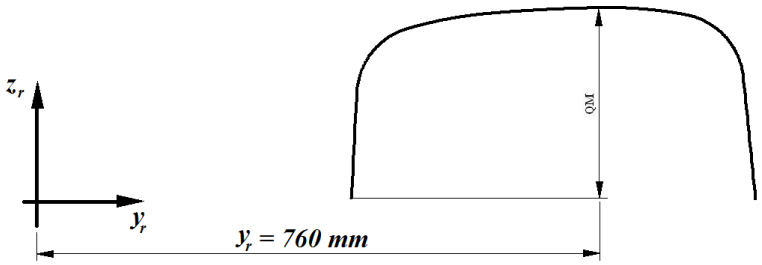

Figure 5.3: Definition of rail wear control parameter.

5.3 Experimental Data

The experimental data provided by Trenitalia are related only to the wheel wear and consist in the wear control parameters measured as a function of the total distance traveled by the considered vehicle DMU Aln 501 Minuetto; particularly the data have been measured on three different vehicles operating on the Aosta-Pre Saint Didier track that are conventionally called DM061, DM068, DM082. The considered vehicles were initially equipped with new ORE S 1002 wheel profiles; at the same time the initial rail profiles of the line were new UIC 60 profiles canted at $\alpha_p = 1/20$rad. A mean value of the kinematic friction coefficient equal to $\mu_c = 0.28$ has been chosen (typical of the most frequent operating conditions).

Table 5.1: Experimental data of the DMU Aln 501 Minuetto DM061.

km	quotas	1r wheel diameter 816 mm	1l wheel diameter 816 mm	2r wheel diameter 815 mm	2l wheel diameter 815 mm	3r wheel diameter 824 mm	3l wheel diameter 824 mm	4r wheel diameter 823 mm	4l wheel diameter 823 mm	5r wheel diameter 823 mm	5l wheel diameter 823 mm	6r wheel diameter 823 mm	6l wheel diameter 823 mm	7r wheel diameter 819 mm	7l wheel diameter 819 mm	8r wheel diameter 820 mm	8l wheel diameter 820 mm
0	FT	32.453	32.444	32.483	32.384	32.599	31.457	31.438	32.576	31.901	31.867	32.330	32.487	31.937	32.217	32.352	32.433
	FH	27.970	27.894	28.141	28.043	27.969	28.187	28.030	28.271	28.245	27.918	28.141	27.982	28.013	27.937	28.333	27.883
	QR	10.208	10.540	10.824	10.857	10.620	10.706	10.679	11.233	10.732	10.845	10.764	10.619	10.821	10.900	10.738	10.796
1426	FT	31.355	30.477	31.783	30.817	31.618	30.883	31.652	30.950	31.296	31.299	31.788	30.983	31.302	30.585	31.767	30.816
	FH	28.010	27.923	28.104	28.108	28.000	28.249	28.095	28.278	28.248	28.284	28.247	28.030	28.997	28.003	30.383	27.919
	QR	9.297	8.626	9.822	9.356	9.744	9.149	9.951	9.472	10.035	10.167	10.173	9.163	9.993	9.283	10.075	9.162
2001	FT	30.556	29.998	31.222	30.378	30.941	30.167	30.129	30.217	30.653	29.601	31.239	30.341	30.566	29.947	31.125	30.277
	FH	27.990	27.880	28.161	28.080	29.998	28.248	28.128	28.283	28.290	27.994	28.273	28.022	28.027	28.014	28.362	27.957
	QR	8.804	7.958	9.633	9.037	9.102	8.350	9.273	8.836	9.544	8.541	9.635	8.486	9.438	8.552	9.648	8.473
2575	FT	29.759	28.596	30.833	29.545	30.472	29.585	30.529	29.624	30.553	29.100	30.595	30.005	30.053	29.366	30.705	29.973
	FH	28.009	27.089	28.173	28.020	28.063	28.243	28.090	28.241	28.285	27.963	28.244	28.085	28.030	28.018	28.352	27.968
	QR	7.598	7.424	9.253	8.563	8.523	7.998	8.838	8.191	9.268	7.795	8.959	8.240	8.772	7.740	9.177	8.300

Table 5.2: Experimental data of the DMU Aln 501 Minuetto DM068.

km	quotas	1r wheel diameter 819 mm	1l wheel diameter 819 mm	2r wheel diameter 820 mm	2l wheel diameter 820 mm	3r wheel diameter 822 mm	3l wheel diameter 822 mm	4r wheel diameter 822 mm	4l wheel diameter 822 mm	5r wheel diameter 816 mm	5l wheel diameter 816 mm	6r wheel diameter 822 mm	6l wheel diameter 822 mm	7r wheel diameter 818 mm	7l wheel diameter 818 mm	8r wheel diameter 819 mm	8l wheel diameter 819 mm
0	FT	32.419	32.820	32.254	32.325	32.434	32.049	32.583	32.126	32.566	32.538	32.502	32.258	32.187	32.457	32.395	32.209
	FH	28.270	27.826	28.329	27.968	28.137	28.084	28.091	28.084	28.257	27.995	28.295	27.811	28.390	27.651	28.221	27.518
	QR	10.613	10.083	10.716	10.273	10.430	10.006	10.024	10.006	10.511	10.364	10.509	10.408	10.700	10.338	10.335	10.080
1050	FT	31.928	31.418	31.259	31.303	31.890	30.858	31.833	31.013	32.082	31.223	31.867	30.988	31.691	32.080	31.915	30.504
	FH	28.228	27.876	28.325	27.922	28.148	28.006	28.091	28.112	28.262	28.092	28.307	27.884	28.383	27.710	28.245	27.552
	QR	10.134	8.684	10.377	9.267	9.973	8.740	9.615	8.834	9.980	9.083	10.130	8.998	10.202	8.965	9.895	8.370
2253	FT	30.253	29.718	30.617	30.514	30.276	29.030	30.470	29.718	30.187	29.222	30.522	29.012	30.309	29.345	30.641	28.806
	FH	28.304	27.911	28.344	28.054	28.202	28.104	28.085	28.216	28.295	28.099	28.320	27.926	28.382	27.698	28.318	27.632
	QR	8.604	7.209	9.130	8.382	8.294	7.326	8.238	7.343	8.395	7.444	8.793	7.274	8.862	7.065	8.662	7.034
2576	FT	29.642	29.478	30.628	30.367	30.190	29.070	30.622	29.508	29.965	29.121	30.388	28.948	29.982	29.382	30.329	28.471
	FH	28.278	27.883	28.335	28.037	28.213	28.102	28.113	28.171	28.236	28.172	28.341	27.889	28.406	27.792	28.18	27.581
	QR	8.142	7.111	9.032	8.237	8.064	7.246	8.213	7.422	8.058	7.319	8.692	8.284	8.470	7.070	8.181	6.940

Table 5.3: Experimental data of the DMU Aln 501 Minuetto DM082.

km	quotas	1r wheel diameter 846 mm	1l wheel diameter 846 mm	2r wheel diameter 846 mm	2l wheel diameter 846 mm	3r wheel diameter 846 mm	3l wheel diameter 846 mm	4r wheel diameter 846 mm	4l wheel diameter 846 mm	5r wheel diameter 846 mm	5l wheel diameter 846 mm	6r wheel diameter 846 mm	6l wheel diameter 846 mm	7r wheel diameter 846 mm	7l wheel diameter 846 mm	8r wheel diameter 846 mm	8l wheel diameter 846 mm
0	FT	32.473	32.278	32.545	32.237	32.394	32.423	32.382	32.309	32.404	32.064	32.399	32.664	32.116	32.476	32.367	32.338
	FH	28.239	27.916	28.032	27.851	28.294	27.947	28.260	27.910	28.196	27.918	28.100	27.931	28.064	28.071	27.958	28.143
	QR	10.447	10.108	10.518	10.274	10.728	10.229	10.782	10.178	10.474	10.483	10.559	10.283	10.441	10.202	10.313	10.321
852	FT	32.417	31.860	32.336	31.831	32.063	31.929	32.324	31.776	32.410	31.592	32.166	32.036	31.817	32.064	32.030	31.641
	FH	28.189	28.043	28.040	27.917	28.332	28.050	28.331	28.008	28.237	27.914	28.170	28.002	28.213	28.126	27.866	28.130
	QR	10.141	9.800	10.256	9.912	10.405	9.865	10.466	9.951	10.284	10.015	10.220	9.812	10.496	9.721	10.147	9.835
1800	FT	31.232	30.721	31.539	30.738	31.380	30.804	31.539	30.773	31.361	30.349	31.721	30.817	31.144	31.182	31.469	30.216
	FH	28.209	28.001	28.009	27.908	28.374	27.995	28.240	28.061	28.285	27.923	28.165	28.014	28.110	28.126	27.975	28.179
	QR	9.206	8.619	9.503	8.765	9.672	8.644	9.831	8.792	9.372	8.856	9.609	8.650	9.334	8.992	9.321	8.341
2802	FT	29.939	29.614	30.778	29.864	30.354	30.068	31.057	29.385	30.027	29.458	30.997	29.678	30.052	30.407	30.600	29.227
	FH	28.165	28.044	28.088	27.897	28.287	28.024	28.293	28.045	28.233	27.883	28.128	27.931	28.072	28.126	27.562	28.201
	QR	7.844	7.348	8.733	7.885	8.762	7.871	9.065	7.486	8.385	7.885	9.009	7.321	8.172	8.224	8.390	7.431
3537	FT	29.660	29.321	30.512	29.621	30.023	29.806	30.498	29.066	29.760	29.143	30.038	29.304	29.554	30.158	30.024	28.744
	FH	28.196	28.021	28.062	27.928	28.320	28.056	28.298	27.996	28.314	28.002	28.229	27.956	28.067	28.130	28.075	28.202
	QR	7.106	7.234	8.460	7.553	8.383	7.608	8.707	7.111	7.809	7.455	8.229	7.176	7.920	7.917	7.851	7.273

As can be seen by the Tabs. 5.1-5.3, the reference quota values have been measured for all the vehicle wheels (each vehicle has eight wheelsets and thus sixteen wheels as specified in section 3.1). However the following data processing has been necessary in order to obtain as output a single average wheel profile that could be effectively compared with the profile extracted from the numerical simulation and to reduce the measurement errors:

1. initially the arithmetic mean on all the sixteen vehicle wheels has been evaluated; the mean is necessary to obtain a single wheel profile and, at the same time, to reduce the measurement errors affecting the experimental data;

2. then a scaling of the quota values has been carried out to delete the offset on the initial value of the considered quantities: this procedure imposes that all the wear control parameters start from their nominal values (the standard values for the new unworn ORE S 1002 profile have been used) in order to remove the initial differences among the vehicles due to measurement errors;

3. the arithmetic mean on the three vehicle MD061, MD068, MD082 has not been carried out, to maintain a dispersion range for the experimental data.

The experimental data, properly processed, are summarized in Tab. 5.4. As can be seen, the flange height FH remains approximately constant because of the low mileage traveled by the vehicles, while the flange thickness FT and the flange steepness QR decrease almost linearly and highlight, according to the characteristics of the track, the wear concentration in the wheel flange.

Concerning the rail wear, the QM quota evolution is compared with a heuristic criterion present in literature (based on the total tonnage burden on the track) [14]. Particularly a proportionality relationship between tonnage and wear holds: a rail wear of 1mm on the rail head height every $100Mt$ (millions of tons) of accumulated tonnage is expected.

Table 5.4: Experimental data processed.

Vehicle	Distance traveled (km)	FH (mm)	FT (mm)	QR (mm)
DM061	0	28.0	32.5	10.8
	1426	28.2	31.5	9.8
	2001	28.1	30.8	9.1
	2575	28.0	30.2	8.6
DM068	0	28.0	32.5	10.8
	1050	28.0	31.8	10.0
	2253	28.0	30.2	8.5
	2576	28.0	30.0	8.4
DM082	0	28.0	32.5	10.8
	852	28.0	32.3	10.6
	1800	28.0	31.3	9.6
	2802	28.0	30.3	8.7
	3537	27.6	30.0	8.3

5.4 Aosta-Pre Saint Didier Line Results

The results in terms of wheel and rail profiles evolution due to wear, obtained employing the wear model on whole Aosta Pre-Saint Didier line will be presented and compared with the experimental data.

5.4.1 Evolution of Wear Control Parameters

In this section the evolution of the wheel reference quotas numerically evaluated by means of the wear model (flange thickness FT, flange height FH and flange steepness QR) will be compared with the experimental data concerning the three DMUs Aln 501 Minuetto vehicles. Furthermore the rail reference quota QM evolution will be shown and compared with the criterion present in literature based on the total tonnage burden on the track [14].

To have a good compromise between calculation time and result accuracy a suitable number of wheel and rail discrete steps is adopted, $n_{sw} = 20$ and $n_{sr} = 5$, and consequently the wheel wear threshold is fixed equal to $D^w_{step} = 0.2$mm and the rail wear threshold is fixed equal to $D^r_{step} = 0.8$mm.

The progress of FT dimension, for the n_{sr} discrete step of the rail, is shown in Fig. 5.4 as a function of the mileage; as it can be seen, the decrease of the dimension is almost linear with the traveled distance except in the first phases, where the profiles are still not conformal enough; as the wheel-rail contact becomes more and more conformal the wear rate is more regular and then the quotas decrease more slowly. The FH quota progress is represented in Fig. 5.5 and shows that, due to the high sharpness of the considered track and to the few kilometers traveled, the wheel wear is mainly

localized on the flange rather than on the tread; therefore the flange height remains near constant in agreement with experimental data. The QR trend is shown in Fig. 5.6: also the flange steepness decreases almost linearly except in the first phases, leading to an increase of the conicity of the flange. Finally the evolution of the wheel control parameters remains qualitatively similar as the rail wear raises, with a slight increase of all the quotas that indicates a shift of the material removed towards the wheel tread, because of the more and more conformal contact. In Tab. 5.5 the total mileages traveled by the vehicle for each rail step n_{sr} are showed.

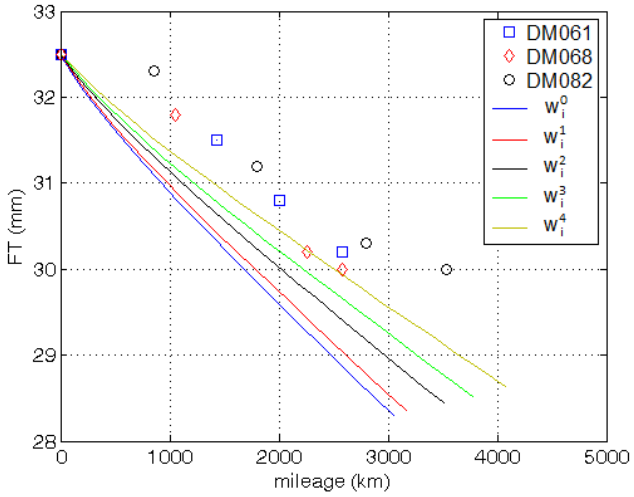

Figure 5.4: Aosta Pre-Saint Didier line: FT dimension progress.

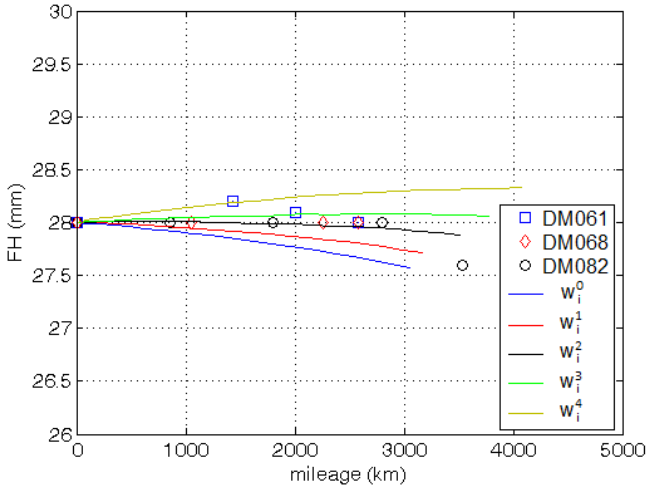

Figure 5.5: Aosta Pre-Saint Didier line: FH dimension progress.

The QM evolution for the analysis of the rail wear is presented in Fig. 5.7 and shows the almost linear dependence between the rail wear and the total tonnage burden on the track. The amount of removed material on the rail head, equal to 2.97mm, is

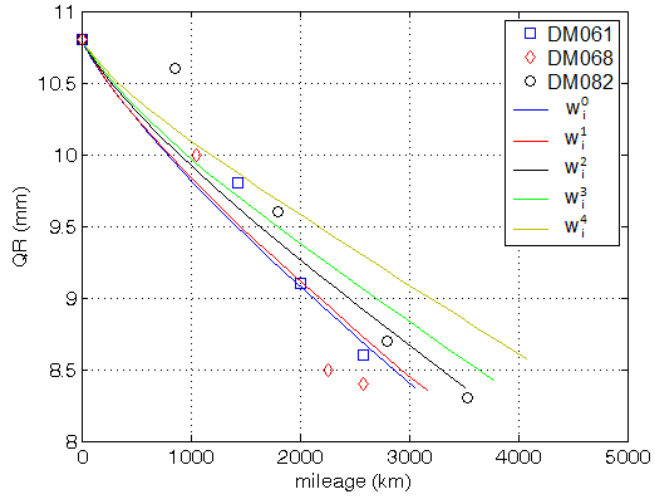

Figure 5.6: Aosta Pre-Saint Didier line: QR dimension progress.

Table 5.5: Evolution of the total mileage km_{tot}.

	km_{tot} (km)
km_{tot}^0	3047
km_{tot}^1	3163
km_{tot}^2	3515
km_{tot}^3	3772
km_{tot}^4	4080

in agreement with the heuristic criterion present in literature (1mm on the rail head height every 100 Mt of accumulated tonnage); the total vehicle number evolving on the track during the whole simulation procedure corresponds to a tonnage of $M_{tot} = N_{tot} * M_v = 310\ Mt$ (the vehicle mass is $M_v = 104700$kg (see Tab. 3.2)) (see Tab. 5.6).

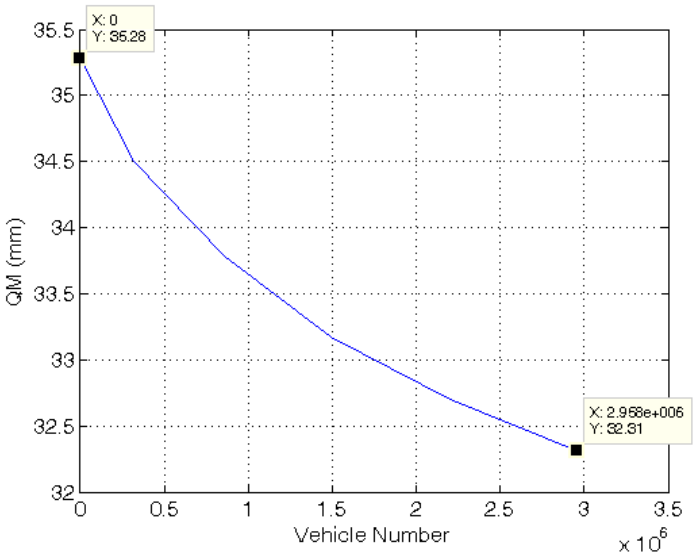

Figure 5.7: Aosta Pre-Saint Didier line: QM dimension progress.

Table 5.6: Total vehicle number N_{tot}.

N_{tot}	2957850

In Fig. 5.8 the evolution of the km_{step} as a function of the wheel discrete step number n_{sw} is shown (for brevity only the km_{step} related to the former and the latter rail step are presented). Related to the first rail step r_0, the lower km_{step} values and their particular increasing trend in the first wheel steps indicate the higher wear rate due to the initial non conformal contact characterizing the coupling between the new ORE S1002 wheel profile and the rail profile UIC 60 with laying angle equal to 1/20rad; the almost constant values in the latter steps (combined with higher km_{step} values) show at the same time the achievement of a more and more conformal contact as the wheel wear increases. Considering the latter rail step r_4 the same curve trend can be seen but characterized by higher km_{step} values because of the worn rail profile that leads to an initial more conformal contact than the previous case. In Fig. 5.9 the evolution of the N_{step} as a function of the rail discrete number n_{sr} shows that the considerations related to the variation of the contact conformity hold also for the rail wear evolution.

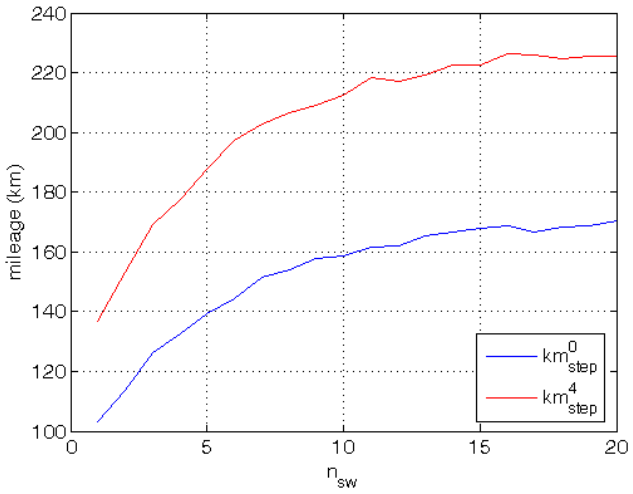

Figure 5.8: Aosta Pre-Saint Didier line: evolution of the km_{step}.

5.4.2 Evolution of the Wheel and Rail Profiles

The wear evolution on the wheel profiles evolving on different rail steps is presented in the Figs. 5.10-5.11 (for reasons of brevity only the profiles evolution related to the first and the last rail steps are showed). As stated previously, the wheel profile evolution is described by means of $n_{sw} = 20$ steps and the threshold on the removed

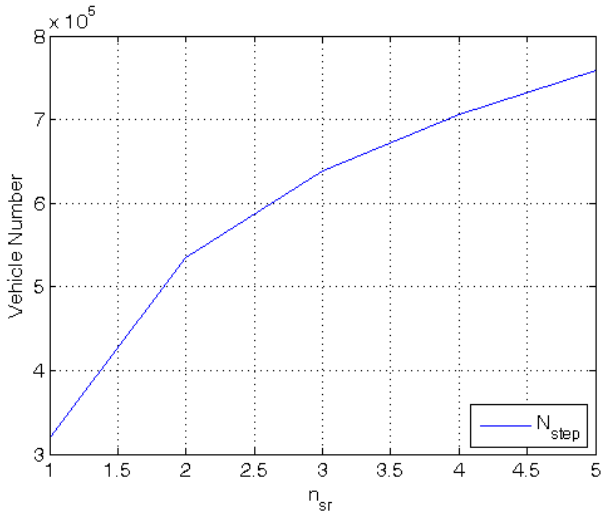

Figure 5.9: Aosta Pre-Saint Didier line: evolution of the N_{step}.

material for each step D^w_{step} has been chosen equal to 0.2mm. The figures show the main localization of the material removed on the wheel flange due to the quite sharp curves that characterize the Aosta-Pre Saint Didier line. The Figs. 5.12-5.13 show the cumulative distributions of removed material in vertical direction z_w on the wheel profile at the first and the last rail step $\sigma_{w_{Kw}}{}^0(y_w) = \sum_{i=1}^{Kw} \sigma_i^{w0}(y_w)$ and $\sigma_{w_{Kw}}{}^{n_{sr}-1}(y_w) = \sum_{i=1}^{Kw} \sigma_i^{wn_{sr}-1}(y_w)$ $(1 \leq Kw \leq n_{sw})$ as a function of y_w, where $\sigma_i^{wj}(y_w)$ is the removed material between two subsequent discrete steps of the wheel profile evolution (the $i-th$ and the $(i-1)-th$ wheel discrete steps) at the $j-th$ rail step $(0 \leq j \leq n_{sr}-1)$ (for reasons of clarity only the distributions characterized by $Kw = 1,10,n_{sw}$ are represented). It can be seen a shift of the material removed towards the wheel tread as the wheel is coupled with more and more worn rail profile due to the achievement of a more conformal contact in the wheel-rail pairs.

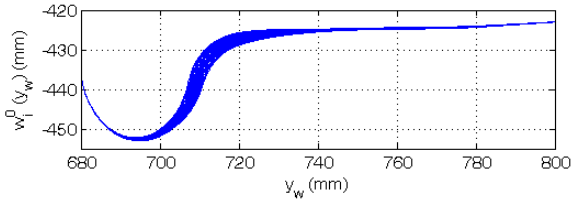

Figure 5.10: Aosta Pre-Saint Didier line: w_i^0 profile evolution.

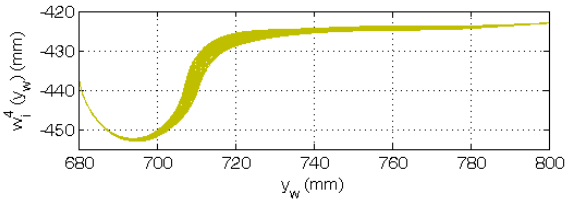

Figure 5.11: Aosta Pre-Saint Didier line: w_i^4 profile evolution.

In Fig. 5.14 the evolution of the rail profile is shown, described by means of $n_{sr} = 5$ discrete step and with the threshold on the removed material for each step D^r_{step} equal to 0.8mm.

The results analysis presented in this section leads to state that the developed wear model reproduces quite good the evolution of all the profile characteristic dimensions,

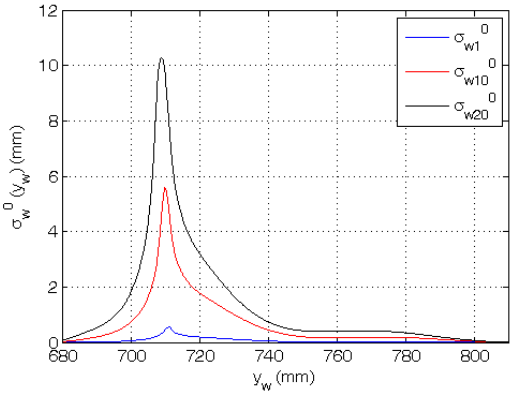

Figure 5.12: Aosta Pre-Saint Didier line: cumulative distributions $\sigma_{wi}{}^{0}$ of the removed wheel material.

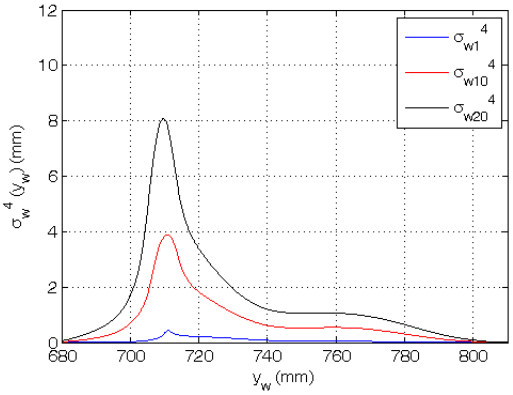

Figure 5.13: Aosta Pre-Saint Didier line: cumulative distributions $\sigma_{wi}{}^{4}$ of the removed wheel material.

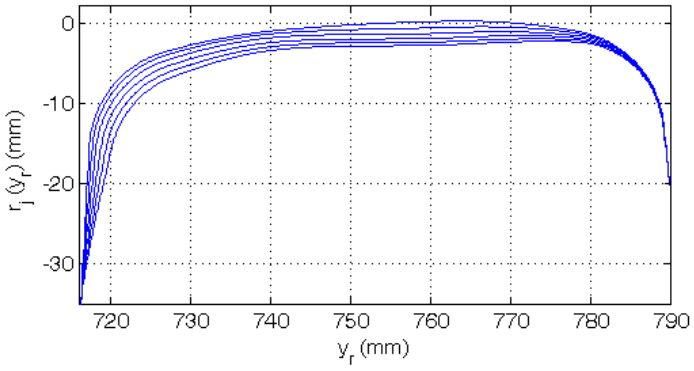

Figure 5.14: Aosta Pre-Saint Didier line: rail profile evolution.

describing in satisfying way the wear progress both on the wheel and on the rail. The results obtained for the wheel profile evolution highlights how, in the particular operating conditions of the studied railway line, the wear is quite severe and strongly localized on the wheel flange, leading to frequent maintenance interventions. As regards the rail profile evolution, the wear is mainly focused on the rail head due to the initial low conformity of the coupling ORE S 1002-UIC 60 with $\alpha_p = 1/20$rad while the total tonnage considered is not sufficient to produce an high wear also on the shoulder of the rail.

Chapter 6

Statistical Analysis of the Railway Track

When the wear analysis has to be carried out on a set of tracks of considerable length by using, at the same time, accurate models for the vehicle and the wheel-rail contact, the utilization of "railway line statistical model" may be an indispensable way to overcome a series of problems due to the computational times and the organization of the simulations themselves. The basic idea is to substitute a complex railway network or the too long tracks to be simulated with a set of simpler tracks which can produce an equivalent amount and distribution of wear both on the vehicle wheels and on the rail tracks [42][43][44][48][49][50].

The steps performed to get the statistical representation is the following:

- since the idea is to obtain a set of simple right curved tracks, each of them characterized by curve radius, superelevation height and a traveling speed, as a first step the whole available track data have been grouped in radius classes. The criterion on which the radius classes have been generated is based on the curvature of the track k, i.e. the reciprocal of the curve radius; starting from the track data the minimum and maximum curvature values are extracted and a set of equidistant curvature intervals are defined. In this way a set of n_{class} curve radius intervals characterized by a minimum R_{min} and a maximum R_{max} radius is identified: the use of the curvature equidistant intervals instead of the curve radius ones guarantees a better accuracy to describe the small radius curves;

- each of these intervals was furthermore divided in n_{class} superelevation subclasses, characterized by h_{min} and h_{max} values. In the proposed approach the same number n_{class} both for the radius and the superelevation classes is considered;

- for each radius classes a representative radius R_c was calculated as a weighted average on all the curve radii, using the length of curve as a weighting factor;

- likewise for each superelevation subclass the correspondent representative superelevation H_c was chosen as a weighted average on all the curve superelevation, using the length of curve as a weighting factor;

- in the statistical approach it is assumed that the wear evolution can be reproduced with a series of simulations on steady curves and straight tracks, neglecting the contribution of the transition lengths (parabolic curves and clothoids [14]) used to connect sections having different superelevation and curve radius. In fact, it would be conceptually difficult to classify and take into consideration these sections; that is the reason why transition lengths have been introduced only in the calculation of the length of the curves, by assigning half length to the curve part and half length to the straight part or to the other adjacent section in case of consecutive curves. For all the missing transition lengths, the information of which are not available from the track data, a reasonable length has been introduced on the basis of the maximum allowable roll speed $\Omega \leq 0.038\text{rad/s}$ and the maximum allowable derivative of the non-compensated acceleration (Eq. 6.1), equal to $\Psi \leq 0.35\text{m/s}^3$ for the rank to which the vehicle belongs [14]. First of all, the instantaneous non-compensated acceleration for a railway vehicle running in a curve (Fig. 6.1) is defined as:

$$a_{nc} = \frac{V^2}{R} - g\frac{h}{s_t}\,, \tag{6.1}$$

in which V is the constant vehicle speed, R is the curve radius, h is the superelevation height, g the gravitational acceleration and s_t the nominal distance (1500mm) between the two contact points on the wheelset when it is centered on the track. The approximated expressions of Ω and Ψ are instead the following:

$$\Omega \cong \frac{\Delta h \cdot V}{s_t l} \tag{6.2a}$$

$$\Psi \cong \frac{V \cdot \Delta a_{nc}}{l}\,, \tag{6.2b}$$

where Δh and s_t are expressed in mm, V is the constant vehicle speed in the transition sections (in m/s), $\Delta a_{nc}\,(\text{m/s}^2)$ is the variation in non-compensated acceleration and l (in m) the length of the transition section. The two above mentioned criteria can be satisfied at the same time by choosing an opportune value for the superelevation gradients dh/ds with respect to the curvilinear abscissa s of the track in the range 1–1.5‰, considering that $dh/ds \cdot l \cong \Delta h$.

- for each superelevation subclass a speed value V_c was chosen as the minimum value

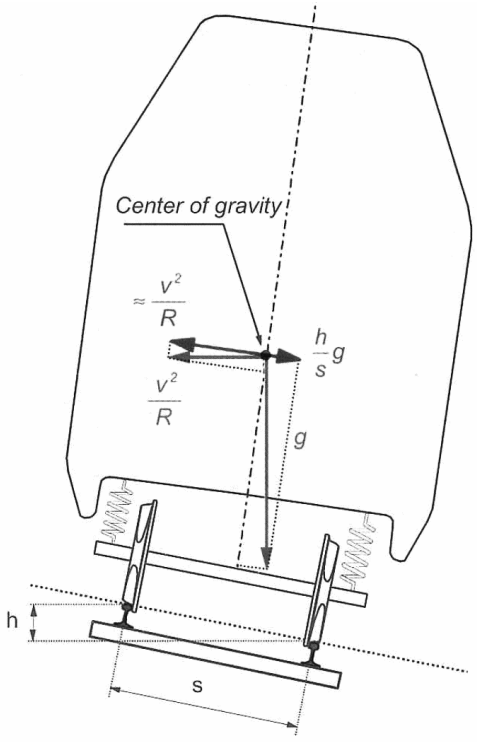

Figure 6.1: Acceleration in curve.

between the maximum speed allowable in curve equal to V_{max} (depending on the radius, the superelevation and the vehicle characteristics) and the speed value V calculated with the equation 6.1 imposing a non-compensated acceleration $a_{nc}^{lim} = 0.6\text{m/s}^2$:

$$V_c = min(V, V_{max}). \tag{6.3}$$

For the straight class the speed value V_c was defined as the maximum vehicle velocity compatibly with the speed line limit.

- finally a weighting factor p_k, calculated as explained in paragraph 4.3, was introduced for each subclass to take into account the frequency of a certain matching radius-superelevation in the track and to diversify the wear contributions of the different curves.

6.1 Statistical Approach Validation

The statistical approach to the railway track has been validated considering the Aosta Pre-Saint Didier scenario. Firstly the statistical track description of the Aosta Pre-Saint Didier line has been extracted according to the provisions described just

above. Then the wear results (evolution both of the reference dimensions and of wheel and rail profiles) have been obtained by means of dynamical simulations of the DMU Aln 501 Minuetto traveled on the N_c classes of curve extracted by the whole Aosta Pre-Saint didier railway network. Finally a carefully comparison between the complete track description results and the statistical analysis ones has been performed focusing both on the model accuracy and on the computational effort. Moreover the sensibility analysis of the statistical approach with respect to the n_{class} parameter will be presented.

6.1.1 Aosta Pre-Saint Didier Statistical Line

The n_{class} parameter plays a fundamental role according to the philosophy of the algorithm used to extract the statistical track description; the classes of curves number N_c and thus the accuracy of the statistical line is strongly dependent by the n_{class} parameter.

As an example in Tab. 6.1 is reported the track classification provided by the statistical approach to the Aosta-Pre Saint Didier line with $n_{class} = 7$, made up of $N_c = 20$ different classes (19 curves and the straight track). For each one of the N_c classes of curves the unworn (i.e just re-profiled) UIC 60 rail profile canted at 1/20rad has been adopted as starting condition for the wear evaluation (also the wheels start from the unworn condition).

6.1.2 Aosta Pre-Saint Didier Statistical Line Results

In this paragraph the results obtained with the statistical analysis approach will be presented. For this purpose a suitable value of the n_{class} parameter have to be supposed. For the Aosta-Pre Saint Didier line the value $n_{class} = 10$, as will be shown in the following, represents a good compromise among track description, result accuracy and computational effort; in fact a n_{class} too high would increase the result accuracy but would increase the computational time too and would lead to a high number of curve classes quite difficult to be statistically treated.

Evolution of Wear Control Parameters

To perform a faithful comparison between the statistical approach and the complete railway one, the same numbers of wheel and rail discrete steps chosen in the whole Aosta Pre-Saint Didier network description are adopted: $n_{sw} = 20$ and $n_{sr} = 5$. At the same manner the wheel wear threshold is fixed equal to $D^w_{step} = 0.2$mm and the rail wear threshold is fixed equal to $D^r_{step} = 0.8$mm.

Table 6.1: Example of curvilinear tracks obtained with the statistical analysis ($n_{class} = 7$).

$\mathbf{R}_{min}$ (m)	$\mathbf{R}_{max}$ (m)	**Superelevation** $h_{min} - h_{max}$ (mm)	$\mathbf{R}_c$ (m)	$\mathbf{H}_c$ (mm)	$\mathbf{V}_c$ (km/h)	$\mathbf{p}_k$ %
150	175	0 - 19	-			
		20 - 39	-			
		40 - 59	-			
		60 - 79	-			
		80 - 99	-			
		100 - 119	162	110	57	0.93
		120 - 140	162	131	60	1.30
175	209	0 - 19	-			
		20 - 39	-			
		40 - 59	-			
		60 - 79	-			
		80 - 99	195	90	60	7.09
		100 - 119	195	103	60	7.42
		120 - 140	195	126	60	5.48
209	259	0 - 19	-			
		20 - 39	-			
		40 - 59	-			
		60 - 79	237	70	60	0.87
		80 - 99	237	83	60	8.76
		100 - 119	237	109	60	4.63
		120 - 140	237	120	60	0.47
259	342	0 - 19	-			
		20 - 39	-			
		40 - 59	293	50	60	0.28
		60 - 79	293	65	60	3.05
		80 - 99	293	83	60	0.90
		100 - 119	293	100	60	0.31
		120 - 140	-			
342	503	0 - 19	-			
		20 - 39	-			
		40 - 59	376	49	60	1.13
		60 - 79	376	62	60	1.26
		80 - 99	-			
		100 - 119	-			
		120 - 140	-			
503	948	0 - 19	-			
		20 - 39	774	24	60	1.73
		40 - 59	774	40	60	0.42
		60 - 79	-			
		80 - 99	-			
		100 - 119	-			
		120 - 140	-			
948	8400	0 - 19	3572	5	60	2.40
		20 - 39	3572	20	60	0.91
		40 - 59	-			
		60 - 79	-			
		80 - 99	-			
		100 - 119	-			
		120 - 140	-			
8400	∞	0	∞	0	130	50.65

The Figs. 6.2-6.5 present the evolution of the wear control parameters. It can be seen the same qualitatively trend obtained with the complete railway approach, related both to the conformity considerations and to the localization of the worn material on the wheel flange (see paragraph 5.4.1). In particular the high wear rate in the first phase due to the initial non conformal enough contact condition, can be seen both in FT and QR progress. Furthermore, also in this case, the evolution of wheel control parameters as the rail wear raises, shows a slight increase of all the quotas, sign of the material removed shift towards the wheel tread due to the more and more conformal contact. In Tab. 6.2 it can be seen the total mileage traveled by the vehicle for each rail step n_{sr}.

The QM progress lead to a reduction of the rail head height of 3.28mm in agreement with the criterion present in literature (1mm on the rail head height every 100 Mt of accumulated tonnage); in fact the total vehicle number evolving on the curved track of the statistical description during the whole simulation corresponding to a tonnage of $M_{tot} = N_{tot} * M_v = 322\ Mt$ (see Tab. 6.3).

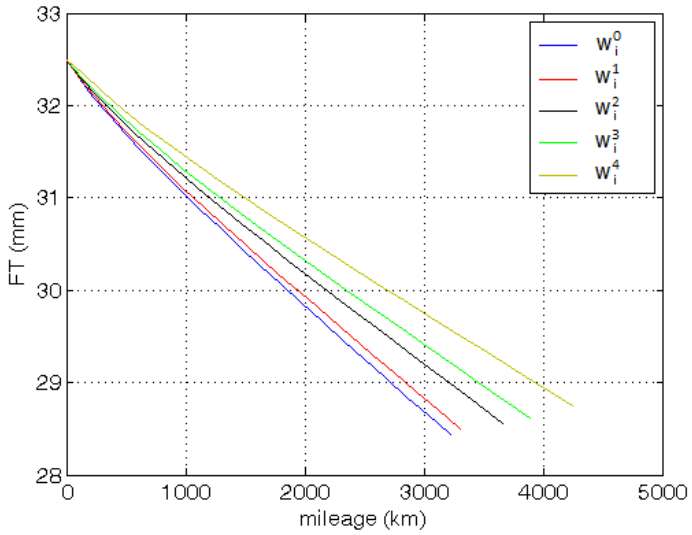

Figure 6.2: Statistical analysis approach: FT dimension progress.

Table 6.2: Evolution of the total mileage km_{tot}.

	km_{tot} (km)
km_{tot}^0	3219
km_{tot}^1	3306
km_{tot}^2	3659
km_{tot}^3	3893
km_{tot}^4	4244

The evolution of the km_{step} and N_{step} as a function of the wheel and rail step numbers n_{sw} and n_{sr} respectively can be seen in the Figs. 6.6-6.7 and shows that the

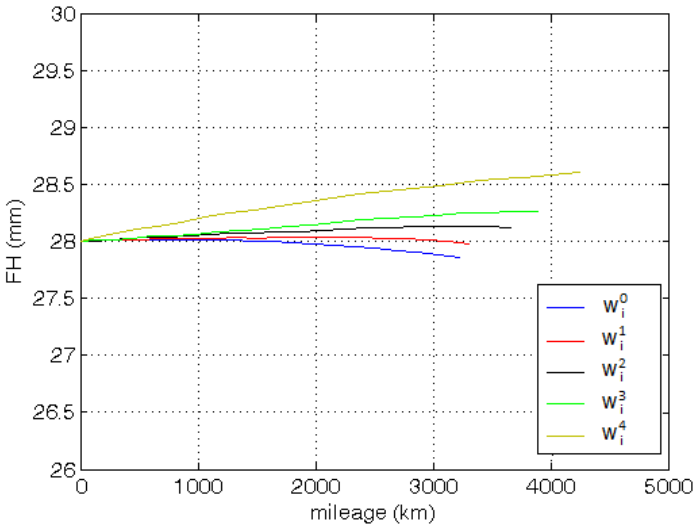

Figure 6.3: Statistical analysis approach: FH dimension progress.

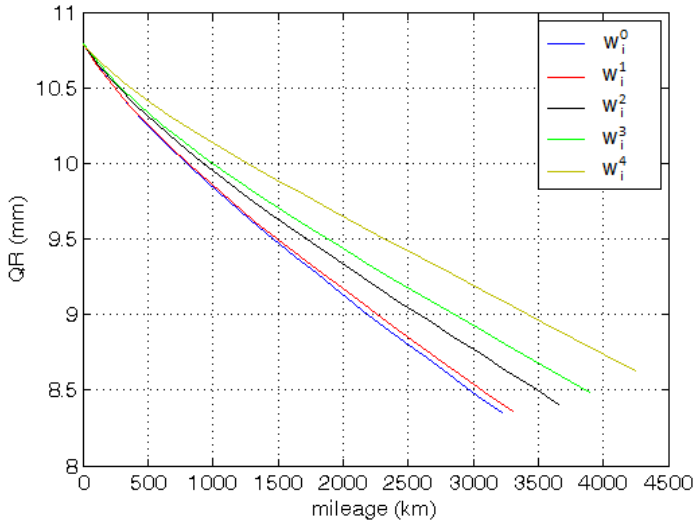

Figure 6.4: Statistical analysis approach: QR dimension progress.

Table 6.3: Total vehicle number N_{tot}.

N_{tot}	3076200

considerations related to the variation of the contact conditions due to the increase of the rail wear (i.e. non conformal and conformal contact) hold also in this case.

Evolution of the Wheel and Rail Profiles

As can be seen in Figs. 6.8-6.11 the evolution of the wheel profile and the cumulative distributions of removed material is qualitatively in agreement with the complete railway approach and the same considerations of section 5.4.2 are valid (for reasons of brevity only the figures referred to the former and the latter rail steps are presented).

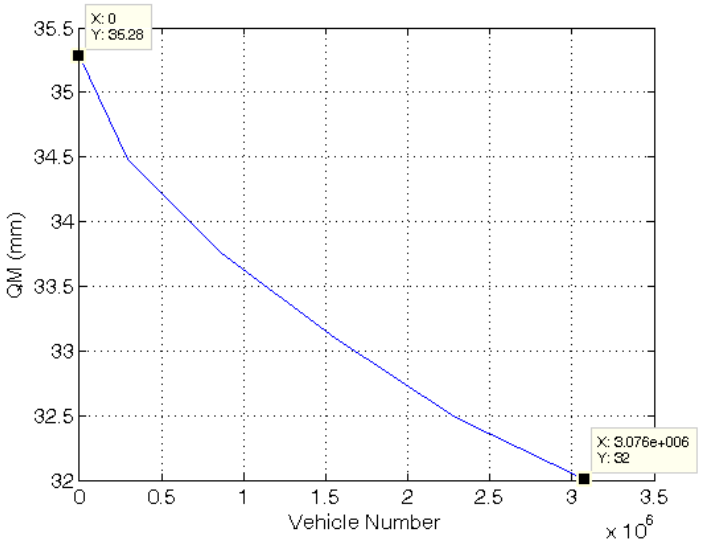

Figure 6.5: Statistical analysis approach: QM dimension progress.

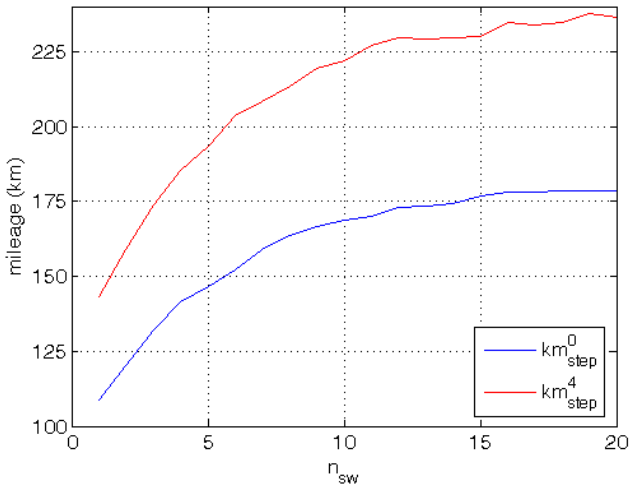

Figure 6.6: Statistical analysis approach: evolution of the km_{step}.

Finally the evolution of the rail profile evolution obtained with the statistical approach is presented in Fig. 6.12.

6.1.3 Comparison between the Complete Railway Line and Statistical Analysis

In this section a quantitatively comparison between the results obtained with the complete railway line (see section 5.4) and the statistical approach with $n_{class} = 10$ (see previous section 6.1.2) will be carried out. In Tabs. 6.4-6.6 the final values of the wheel reference dimensions for each rail step n_{sr} are presented. The increase of the flange height as the rail profile is more and more worn, together with the increase of

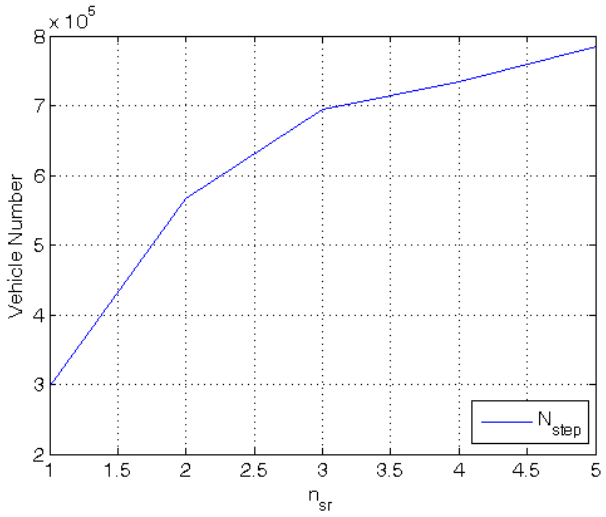

Figure 6.7: Statistical analysis approach: evolution of the N_{step}.

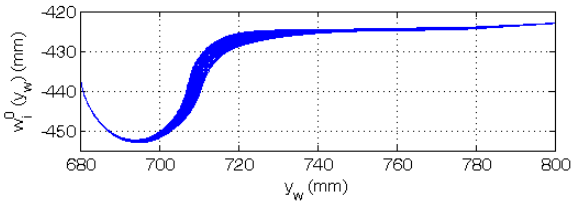

Figure 6.8: Statistical analysis approach: w_i^0 profile evolution.

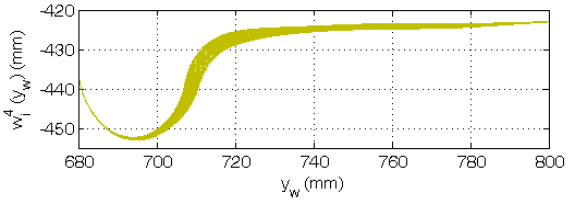

Figure 6.9: Statistical analysis approach: w_i^4 profile evolution.

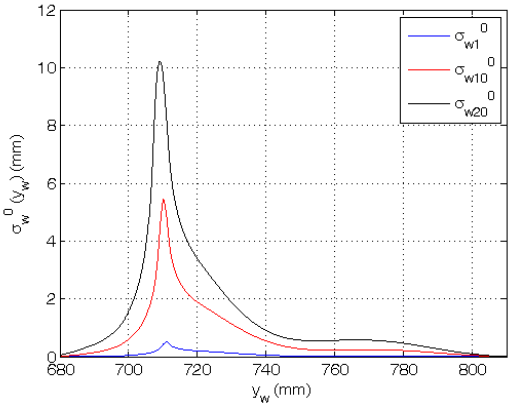

Figure 6.10: Statistical analysis approach: cumulative distributions $\sigma_{wi}{}^0$ of the removed wheel material.

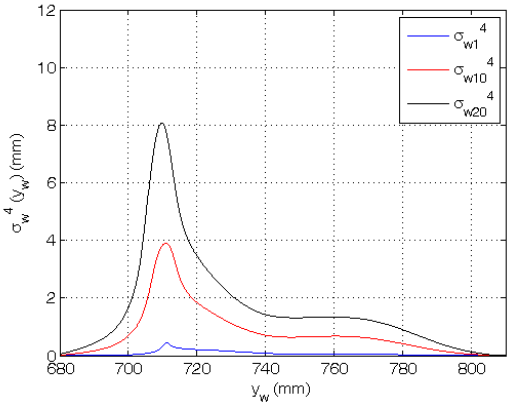

Figure 6.11: Statistical analysis approach: cumulative distributions $\sigma_{wi}{}^4$ of the removed wheel material.

the flange thickness, indicates a shift of the material removed towards the wheel tread due to the variations of the contact conditions as explained in previous sections. The reference dimension comparison shows a good consistency between the two investigate approaches with a maximum error equal to $e = 1.0\%$.

The Tab. 6.7 displays the evolution of the total mileage km_{tot} as a function of the

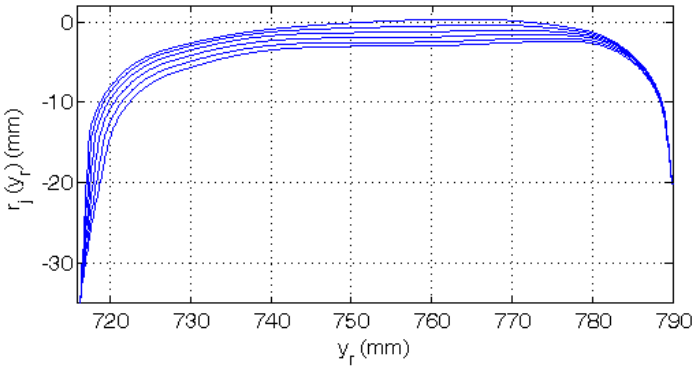

Figure 6.12: Statistical analysis approach: rail profile evolution.

Table 6.4: Evolution of the FH quota.

	Complete Railway	**Statistical Description** $n_{class} = 10$	
	FH (mm)	FH (mm)	e (%)
km^0_{tot}	27.57	27.86	1.0
km^1_{tot}	27.73	27.98	0.9
km^2_{tot}	27.89	28.12	0.8
km^3_{tot}	28.07	28.27	0.7
km^4_{tot}	28.33	28.60	1.0

Table 6.5: Evolution of the FT quota.

	Complete Railway	**Statistical Description** $n_{class} = 10$	
	FT (mm)	FT (mm)	e (%)
km^0_{tot}	28.30	28.43	0.5
km^1_{tot}	28.36	28.50	0.5
km^2_{tot}	28.44	28.56	0.4
km^3_{tot}	28.52	28.62	0.4
km^4_{tot}	28.63	28.75	0.4

Table 6.6: Evolution of the QR quota.

	Complete Railway	**Statistical Description** $n_{class} = 10$	
	QR (mm)	QR (mm)	e (%)
km^0_{tot}	8.38	8.35	0.4
km^1_{tot}	8.35	8.36	0.1
km^2_{tot}	8.37	8.41	0.5
km^3_{tot}	8.43	8.48	0.6
km^4_{tot}	8.57	8.63	0.7

rail step n_{sr} and shows a good consistency between the two considered procedures: the increase of the mileage traveled by the vehicle as the rail profile is more and more worn indicates a decrease of the wear rate explained by a better conformity between wheel and rail surfaces.

In the Tabs. 6.8-6.9 the comparison of the parameters QM and N_{tot} needed to evaluate the rail wear is shown.

Table 6.7: Evolution of the total mileage km_{tot}.

	Complete Railway	**Statistical Description** $n_{class} = 10$	
	km_{tot} (km)	km_{tot} (km)	e (%)
km^0_{tot}	3047	3219	5.6
km^1_{tot}	3163	3306	4.5
km^2_{tot}	3515	3659	4.1
km^3_{tot}	3772	3893	3.2
km^4_{tot}	4080	4244	4.0

Table 6.8: Evolution of the QM quota.

Complete Railway	**Statistical Description** $n_{class} = 10$	
QM (mm)	QM (mm)	e (%)
32.31	32.00	1.0

Table 6.9: Total vehicle number N_{tot}.

	Complete Railway	**Statistical Description** $n_{class} = 10$	e (%)
N_{tot}	2957850	3076200	4.0

6.1.4 Sensibility Analysis of the Statistical Approach

In this paragraph a sensibility analysis of the statistical approach with respect to the class number n_{class}, i.e. the most important parameter of the track discretization, will be presented [42]. The variation range studied is $n_{class} = 4 \div 10$. In Tab. 6.10 is summarized the number of curves N_c (included the straight track) corresponding to each n_{class} value considered.

Table 6.10: Number of curves N_c corresponding to n_{class} parameter.

n_{class}	N_c
4	10
5	13
6	17
7	20
8	23
9	28
10	30

By Analyzing the data relative to the wheel presented in Tab. 6.11, for each value of n_{class} investigated, the trend of the wheel parameters as rail wear raises shows an increase of all the wheel flange dimensions in according to the variation of the contact conditions explained in the previous sections (see 5.4-6.1.3). Analogously the km_{tot} evolution trend is the same for each of the statistical analysis considered, and also the mileage increases as the rail wear increases indicating the more and more conformal contact between wheel and rail surfaces. The error e presented in Tab.

Table 6.11: Evolution of the wheel control parameters (quotas and km_{tot}).

Statistical Description		FH (mm)	e (%)	FT (mm)	e (%)	QR (mm)	e (%)	km_{tot} (km)	e (%)
$n_{class} = 4$	km^0_{tot}	26.99	2.1	28.02	1.0	8.29	1.0	3775	23.9
	km^1_{tot}	27.12	2.2	28.16	0.7	8.25	1.2	3967	25.4
	km^2_{tot}	27.26	2.3	28.19	0.9	8.28	1.1	4267	21.4
	km^3_{tot}	27.49	2.1	28.26	0.9	8.35	1.0	4521	19.9
	km^4_{tot}	27.71	2.2	28.35	1.0	8.47	1.2	4793	17.5
$n_{class} = 5$	km^0_{tot}	27.02	2.0	28.03	1.0	8.31	0.9	3713	21.9
	km^1_{tot}	27.16	2.0	28.16	0.7	8.27	0.9	3877	22.6
	km^2_{tot}	27.31	2.1	28.20	0.9	8.29	1.0	4129	17.5
	km^3_{tot}	27.54	1.9	28.27	0.9	8.35	0.9	4397	16.6
	km^4_{tot}	27.75	2.0	28.36	0.9	8.48	1.1	4688	14.9
$n_{class} = 6$	km^0_{tot}	27.08	1.7	28.06	0.8	8.31	0.8	3620	18.8
	km^1_{tot}	27.24	1.7	28.18	0.6	8.28	0.9	3743	18.5
	km^2_{tot}	27.40	1.8	28.23	0.7	8.29	0.9	4038	14.9
	km^3_{tot}	27.62	1.6	28.31	0.8	8.36	0.9	4237	12.3
	km^4_{tot}	27.83	1.8	28.40	0.8	8.48	1.1	4569	12.0
$n_{class} = 7$	km^0_{tot}	27.11	1.7	28.09	0.7	8.31	0.8	3535	16.0
	km^1_{tot}	27.26	1.7	28.19	0.6	8.29	0.8	3676	16.2
	km^2_{tot}	27.43	1.7	28.25	0.7	8.30	0.9	3984	13.3
	km^3_{tot}	27.65	1.5	28.33	0.6	8.36	0.8	4172	10.6
	km^4_{tot}	27.85	1.7	28.42	0.7	8.48	1.0	4503	10.4
$n_{class} = 8$	km^0_{tot}	27.14	1.6	28.10	0.7	8.33	0.6	3431	12.6
	km^1_{tot}	27.30	1.5	28.19	0.6	8.30	0.5	3529	11.6
	km^2_{tot}	27.47	1.5	28.26	0.6	8.31	0.7	3903	11.0
	km^3_{tot}	27.69	1.3	28.35	0.6	8.37	0.8	4092	8.5
	km^4_{tot}	27.90	1.5	28.44	0.7	8.49	0.9	4445	8.9
$n_{class} = 9$	km^0_{tot}	27.20	1.3	28.13	0.6	8.33	0.6	3308	8.6
	km^1_{tot}	27.37	1.3	28.20	0.6	8.32	0.4	3397	7.4
	km^2_{tot}	27.55	1.2	28.28	0.5	8.31	0.6	3777	7.4
	km^3_{tot}	27.77	1.1	28.38	0.5	8.37	0.7	4011	6.4
	km^4_{tot}	27.97	1.3	28.47	0.6	8.50	0.8	4343	6.4
$n_{class} = 10$	km^0_{tot}	27.86	1.0	28.43	0.5	8.35	0.4	3219	5.6
	km^1_{tot}	27.98	0.9	28.50	0.5	8.36	0.1	3306	4.5
	km^2_{tot}	28.12	0.8	28.56	0.4	8.41	0.5	3659	4.1
	km^3_{tot}	28.27	0.7	28.62	0.4	8.48	0.6	3893	3.2
	km^4_{tot}	28.60	1.0	28.75	0.4	8.63	0.7	4244	4.0

6.11 is referred to the complete railway approach (see section 5.4) and shows less and less consistency between the results of the complete railway approach and the statistical analysis as the n_{class} parameter decreases (see Fig. 6.13). In particular small n_{class} values corresponding to a rough discretization of the track, lead to an important underestimation of the removed material highlighted by the increasing mileage traveled. The less accuracy of the model and the underestimation of the worn material as the track description is more and more rough is found also by analyzing the rail control parameter and the number of the train evolving on the track (see Tab. 6.12 and Fig. 6.14).

Table 6.12: Evolution of the rail control parameters (QM quota and N_{tot}).

Statistical Description	QM (mm)	e (%)	N_{tot}	e (%)
$n_{class} = 4$	31.58	2.3	3797900	28.4
$n_{class} = 5$	31.63	2.1	3641100	23.1
$n_{class} = 6$	31.69	1.9	3543500	19.8
$n_{class} = 7$	31.75	1.7	3398600	14.9
$n_{class} = 8$	31.83	1.5	3309800	11.9
$n_{class} = 9$	31.86	1.4	3188600	7.8
$n_{class} = 10$	32.00	1.0	3076200	4.0

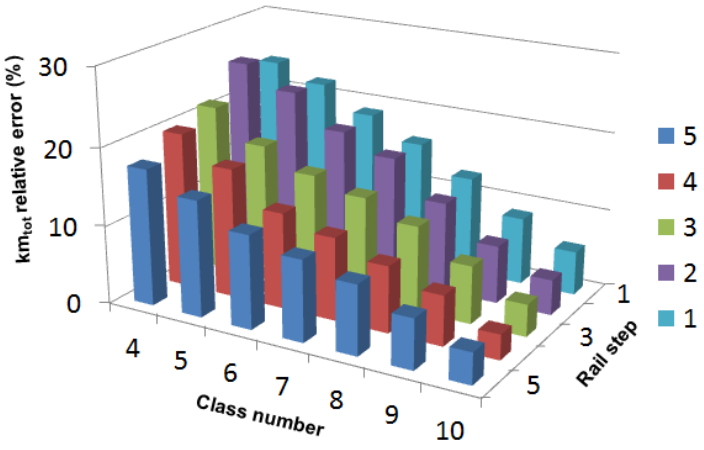

Figure 6.13: Relative error of the km_{tot} parameter referred to the complete railway case.

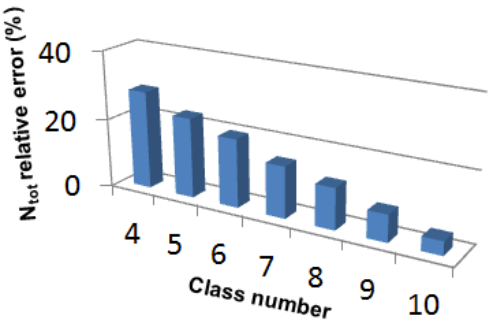

Figure 6.14: Relative error of the N_{tot} parameter referred to the complete railway case.

6.1.5 Computational Effort Comparison

In this section the comparison between the computational load required by the different approaches considered, i.e. the complete railway line and all the analyzed statistical track descriptions ($n_{class} = 4 \div 10$), will be performed.

The characteristics of the processor and the main numerical parameters relative to the integrator used for the dynamical simulations are briefly reported in Tab. 6.13.

Table 6.13: Processor and integrator data.

Processor	INTEL Xeon CPU X5560 2.80 GHz 24GB RAM	
Integrator	Type Alghoritm Order Step type Stepsize	ODE5 Dormand-Prince 5 fixed 10^{-4} s

The mean computational times relative to each discrete step of the whole model loop (for the wheel and for the rail wear evaluation) are schematically summarized in Tab. 6.14 both for the complete railway line and for the statistical descriptions (see also Fig. 6.15): the mean computational times related to the discrete steps of the whole wear

model (t_{wt}, t_{rt} for wheel (see Fig. 6.15(a)) and rail (see Fig. 6.15(b)) respectively) are subdivided in dynamical simulation times (t_{wd}, t_{rd}) and wear simulation times (t_{ww}, t_{rw}). Obviously for all the rail computation times (t_{rt}, t_{rd}, t_{rw}) the relations $t_{rt} = n_{sw} * t_{wt}$, $t_{rd} = n_{sw} * t_{wd}$ and $t_{rw} = n_{sw} * t_{ww}$ hold and the total simulation time is $t_T = n_{sr} * t_{rt}$ where $n_{sw} = 20$ and $n_{sr} = 5$ are the wheel and rail discrete step number introduced in the previous sections.

Table 6.14: Computational time.

Railway approach		Computational time: Wheel wear evaluation t_{wd}	t_{ww}	t_{wt}	Rail wear evaluation t_{rd}	t_{rw}	t_{rt}	Total simulation t_T
Complete track		4d 12min	1d 38min	5d 50min	3dd 12h	1d 8h 40min	4dd 20h 40min	24dd 7h 20min
Statistical analysis	$n_{class} = 4$	8min	4min	12min	2h 40min	1h 20min	4h	20h
	$n_{class} = 5$	11min	4min	15min	3h 40min	1h 20min	5h	1d 1h
	$n_{class} = 6$	13min	6min	19min	4h 20min	2h	6h 20min	1d 7h 40min
	$n_{class} = 7$	15min	7min	22min	5h	2h 20min	7h 20min	1d 12h 40min
	$n_{class} = 8$	18min	7min	25min	6h	2h 20min	8h 20min	1d 16h 40min
	$n_{class} = 9$	21min	9min	30min	7h	3h	10h	2dd 2h
	$n_{class} = 10$	24min	10min	34min	8h	3h 20min	11h 20min	2dd 8h 40min

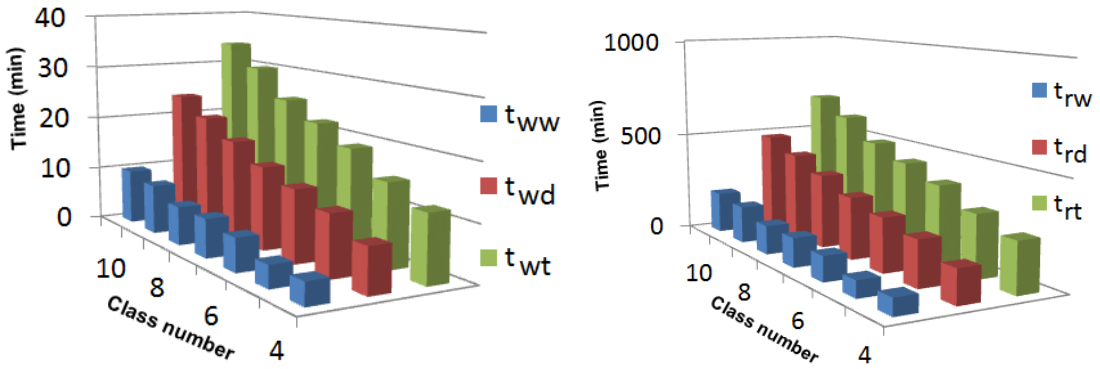

(a) wheel times (b) rail times

Figure 6.15: Statistical analysis: computational effort comparison.

The huge computational effort that affects the complete railway line simulation (more than 24 days for a complete simulation loop), makes this approach hardly feasible to the wear evolution studies typical of the railway field. On the contrary the statistical track description (see the Tabs. 6.11, 6.12 and 6.14) shows a high saving of computational load and at the same time a not excessive loss of model accuracy; in particular with a number of curve class $n_{class} = 10$ wear evaluation results are qualitatively and quantitatively in agreement with the complete line approach (a maximum error $e \simeq 5\%$ on the mileage traveled by the vehicle has been found). To sum up the value $n_{class} = 10$ represents, for in the Aosta-Pre Saint Didier line, a good compromise among track description, result accuracy and computational effort.

In conclusion the innovative wear model developed for the study of complex railway networks using a statistical track description approach is capable to simulate the wear

evolution both on the wheel and on the rail surfaces with reasonable computational time and leads to a good result consistency respect to the considered experimental data.

Chapter 7

Comparison with Commercial Software Wear Model

In this chapter the innovative wear model developed in this research activity will be compared with the wear evaluation model implemented in the commercial software Simpack Rail [48]. An exhaustive comparison will be carried out to evaluate the proposed model performance both in terms of accuracy and efficiency and to further validate the wear model, especially as regard the rail wear evolution. In this regard the rail wear is a long-term phenomenon which requires several months of monitoring to collect the related experimental data; RFI and Trenitalia have scheduled experimental measurement campaigns to investigate the rail wear evolution.

To carry out the performance comparison activity, the scenario composed by the vehicle composition Vivalto (see section 3.1.2 for a detailed vehicle description) running on the Italian railway network has been chosen. A statistical representative mean network has been extracted starting from the data relative to the whole Italian railway line (provided by RFI); the statistical approach is obviously necessary because of the length and the complexity of the considered network that would make both its multibody modeling and the computational load impractical. To better investigate the performance and the usability of the proposed innovative model, in this part of work will be required as output of the wear model both different wheel profiles for each vehicle wheelsets and different rail profile for each representative curve N_c of the statistical analysis, instead of the mean wheel and rail profiles previously used in the validation process performed with the Aln 501 Minuetto traveled on the Aosta Pre-Saint Didier line.

In this chapter for the sake of clarity the innovative model developed in this work will be indicated as UNIFI model, while the benchmark model implemented within the Simpack multibody software will be marked with Simpack model.

7.1 Simpack Wear Model

In this section the general layout of the benchmark wear model implemented within the Simpack multibody software will be presented focusing on the main differences respect to the wear model proposed in this research activity.

7.1.1 General Architecture

The Simpack model layout is similar to the UNIFI one (see chapter 2), with the exception of the local contact model (see Fig. 7.1); in this way an accurate comparison between the models has been possible in terms of accuracy and efficiency. In particular the Simpack wear model uses a global approach to the wear estimation, often used by commercial multibody software to reduce the computational load despite of the model accuracy [26][39].

Therefore the whole model consists of the following parts: the vehicle model fully implemented in Simpack environment (composed by the multibody model and the global contact model) and the global wear model (made up of the wear evaluation directly implemented in Simpack and the profile update implemented in a Matlab environment).

The main difference between the two considered wear models is the approach to the wear problem: the Simpack model uses a global approach to the wear evaluation without taking into account the local contact variables (pressures and creepages) within the contact patch (and consequently its subdivision in sliding and adhesion zone), but using only the global contact variables. This aspect leads to a reduction of the computational load due to the absence of the contact patch discretization and investigation but it mainly causes a decrease of the whole model precision; some works in which the differences between global and local wear approaches are carefully investigated can be found in the literature [36]. Particularly the use of global wear approach involves some handicaps. The improper evaluation of the adhesion and creep zone within the contact patch leads to a likely underestimation or overestimation of the worn material; furthermore the roughness in evaluating the removed material function (due the approximation of the whole contact patch through single contact point) causes both several numerical problems in the wheel and rail profile update procedures and the appearance, in the new profiles, of short wavelengths without physical meaning.

Related to the vehicle model capable of simulating the vehicle dynamics, the benchmark vehicle chosen to compare the wear models is the vehicle composition made up of a locomotive (E.464) and a passengers vehicle (Vivalto), a vehicle configuration widely used in the Italian railway network [40]. As above stated, the track considered to per-

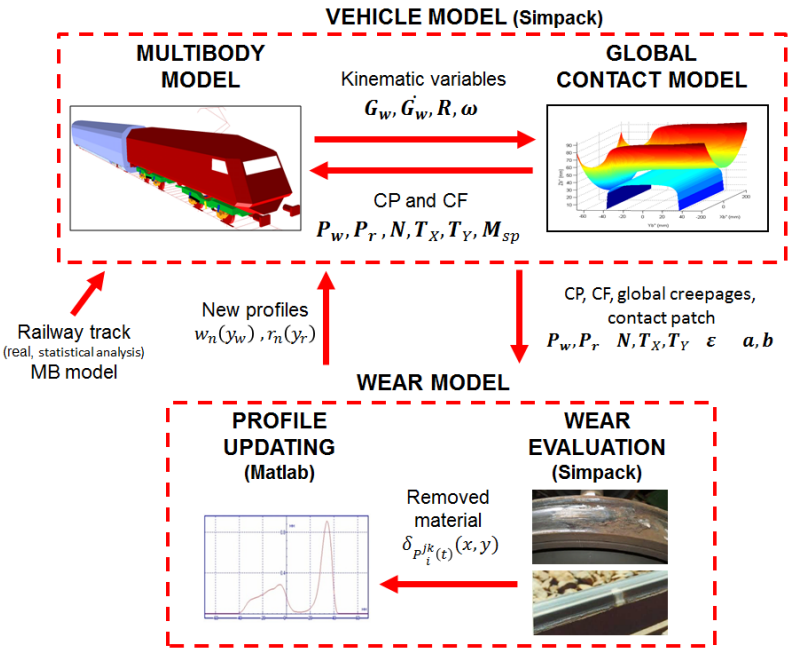

Figure 7.1: General Architecture of the Simpack Model.

form the dynamical simulation is the mean Italian railway line (characterizing by the UIC 60 rail profile with laying angle equal to $\alpha_p = 1/20$rad) traveled by the Vivalto composition, built with the provisions of the statistical approach developed in this work (see the chapter 6) and starting from the the data relative to the whole Italian railway network. No difference with respect to the multibody model are presented in the two considered model layout.

On the contrary, concerning the global contact model, the version implemented in the Simpack commercial software has been used. Also this model is capable of calculating the global contact forces and of detecting multiple contact points at the wheel-rail interface; however, for the research of multiple contact points, the wheel and rail surfaces are divided in three different zones within which a single point can be detected, introducing a limitation on the number of contact points and especially on their position. In addition to the simplifying hypothesis on the geometry and kinematics of the contact problem, the Simpack contact model uses look-up table to evaluate the contact parameters with a consequent loss of the model precision. The outputs of the vehicle model represent also the inputs of the wear model and are the global contact variables evaluated during all the N_c dynamic simulations.

The profile update strategy has been implemented in a Matlab environment in order both to reproduce the same strategy adopted in the UNIFI model and to adapt it to the wear evaluation model implemented in Simpack, based on a different wear law with respect to the UNIFI model [26][39]; moreover the update strategy is necessary because the Simpack model is not designed to simulate a wear loop like that considered in the

UNIFI one; in particular it is not capable to pass back the new worn profiles to the *vehicle model* to close the loop.

Finally the same considerations explained for the UNIFI model about both the discrete approach of the whole model and the adopted discretization strategy hold also for the Simpack model (see chapter 2).

7.1.2 Simpack Global Contact Model

The Simpack wear model employs the global contact model implemented in the Simpack multibody software both for the contact points detection and for the global forces calculation [30].

The standard ORE S1002 wheel profile and UIC 60 rail profile with laying angle equal to $\alpha_p = 1/20$rad have been introduced in Simpack by means of cubic spline approximation; however a limitation on the number of profile sampling points (equal to 600 points) is imposed by the software for computational time requirements unlike the UNIFI global contact model where no limitations are present.

Among all the contact point detection algorithms provided by the software, the more general and suitable version has been chosen to compare the two different models. This algorithm ensures multiple contact points detection but, at the same time, introduces a set of simplifying hypotheses:

- a maximum of three contact points for each wheel-rail pair can be detected;
- the wheel profile is divided in three zones called *tread*, *flange* and *flange2* areas: for each of these a single contact point can be found. Moreover the *flange2* corresponds to the back of the flange and thus only two actual contact points for each wheel-rail pair can be detected. The limitation on the contact points position is an important approximation on the kinematics of the contact problem;
- suitable look-up tables for the calculation of the *tread* contact point location and of the relative tangential forces are used to have reasonable calculation times. The *tread* point is detected considering a quasi-elastic contact. In this case wheel and rail are regarded as qualitatively elastic by means of a special weighting and regularization function (calculated with the look-up table mentioned above): it leads to a virtual contact patch instead of a single contact points and thus no discontinuities can appear with this method.
- the *flange* and *flange2* contacts are calculated online without pre-calculated tables: for these points the wheel-rail contact is considered rigid. With this method, discontinuities in the contact points position and other contact parameters (i.e.

tangential forces) can arise when moving the wheelset laterally over the track. The use of different approaches for the contact points detection (in the *tread* and in the *flange* zones) could result in solver and accuracy problems.

Concerning to the global normal forces calculation, in the *tread* zone the contact between wheel and rail is ensured by introducing a one-sided spring-damper element which moves along the profiles and the track depending on the contact point position; the spring-damper element produces a force only when there is penetration between wheel and rail surfaces. The normal contact force is calculated from the equivalent penetration by means of the Hertz theory. In the *flange* and *flange2* zones, instead, the wheel-rail contact is ensured by introducing a suitable kinematic constraint while the normal force is the constraint force calculated through the Lagrange multipliers method. The tangential forces evaluation, both for the online calculation in the *flange* and *flange2* zones and for the look-up table calculation in the *tread* zone is based on the linear saturated Kalker theory.

7.1.3 Simpack Wear Evaluation

The Simpack wear model is an add-on module of the Simpack multibody software and allows the calculation of wear effects on the wheel and the rail profiles of a railway vehicle [30]. The wear evaluation is a post-processing calculation after a time domain simulation. The global wear approach leads to the estimation of the removed material starting from the global contact creepages without considering the local ones within the contact patch and therefore this quantity represents an averaged volume to be removed on all the contact patch surface, causing a possible wear overestimation.

This model is based on the wear law proposed by Krause and Poll [26] that correlates the volume of removed material for unit of distance traveled by the vehicle (K^{SIM} expressed in m^3/m) with the specific frictional power I^{SIM} dissipated in the contact patch of area A ($I^{SIM} = P_g/A$ expressed in W/mm^2: the global power is $P_g = \mathbf{T}^r \bullet \mathbf{s}_g$ where the global creepages $\mathbf{s}_g = V \begin{pmatrix} \varepsilon_x \\ \varepsilon_y \end{pmatrix}$ are expressed in m/s) by means of a proportionality law. It distinguishes between two wear regimes, *mild wear* and *severe wear*, characterized by different removed material rates: the wear coefficients, i.e. the proportionality factors between frictional work and removed material, supposed the same for wheel and rail, are available in the literature [39]:

$$\begin{aligned} &mild\ wear: && C_{mild} = 9.8710 * 10^{-14}\ m^3/J && I^{SIM} < 4W/mm^2 \\ &severe\ wear: && C_{severe} = 9.8710 * 10^{-13}\ m^3/J = 10 * C_{mild} && I^{SIM} \geq 4W/mm^2. \end{aligned} \tag{7.1}$$

The removed material volume for unit of distance traveled by the vehicle for each wheel and rail is then calculated as follows:

$$K^{SIM} = \frac{1}{2} \cdot C \cdot \frac{P_g}{V} \tag{7.2}$$

where C is the proportionality factor of equation 7.1 and V is the velocity of the vehicle.

Finally the average removed material volume (expressed in $m^3/(m \cdot mm^2)$) in the normal direction to the profiles for the i-th contact patch of the j-th wheel and rail pair during the k-th of the N_c dynamical simulations are obtained:

$$\delta^{tot}_{P^{jk}_{wi}(t)}{}^{SIM}(y_w) = \begin{cases} 0 & y_w \leq -b^{jk}_{wi}/2 \\ \frac{K^{SIM}}{2\pi w(y^{cjk}_{wi}) \cdot b^{jk}_{wi}} & -b^{jk}_{wi}/2 \leq y_w \leq b^{jk}_{wi}/2 \\ 0 & y_w \geq b^{jk}_{wi}/2 \end{cases} \tag{7.3}$$

$$\delta^{tot}_{P^{jk}_{ri}(t)}{}^{SIM}(y_r) = \begin{cases} 0 & y_r \leq -b^{jk}_{ri}/2 \\ \frac{K^{SIM}}{l_k \cdot b^{jk}_{ri}} & -b^{jk}_{ri}/2 \leq y_w \leq b^{jk}_{ri}/2 \\ 0 & y_r \geq b^{jk}_{ri}/2 \end{cases} \tag{7.4}$$

where $w(y^{cjk}_{wi})$ is the wheel radius evaluated in y^{cjk}_{wi} (the transversal position of the generic wheel contact point), l_k is the length of the k-th simulated track ($1 \leq k \leq N_c$) and b^{jk}_{wi}, b^{jk}_{ri} are the generic contact patch widths. The $1/\left[2\pi w(y^{cjk}_{wi}) \cdot b^{jk}_{wi}\right]$ and $1/\left(l_k \cdot b^{jk}_{ri}\right)$ factors average the removed volume for each contact point P^{jk}_i over the whole longitudinal development of the wheel and of the rail.

The global wear evaluation approach, with no local contact model for the investigation of the local variables (pressures and creepages) within the contact patch and therefore no distinction between sliding and adhesion zone in the contact area, leads to the evaluation of the mean wear volumes $\delta^{tot}_{P^{jk}_{wi}(t)}{}^{SIM}(y_w)$ and $\delta^{tot}_{P^{jk}_{ri}(t)}{}^{SIM}(y_r)$ to be subtracted from the rail and the wheel profiles uniformly along all the contact patch width b. This approximation avoids the contact patch discretization leading to a time calculation saving but obviously it causes also a decrease of the whole wear model accuracy.

The outputs of the Simpack wear evaluation are thus the distributions of the removed material $\delta^{tot}_{P^{jk}_{wi}(t)}{}^{SIM}(y_w)$ and $\delta^{tot}_{P^{jk}_{ri}(t)}{}^{SIM}(y_r)$.

7.1.4 Simpack Update Profile Procedure

The update strategy is necessary also for the Simpack model because it is not structured to support a whole wear loop and specifically it is not capable to pass back the new worn profiles to the *vehicle model*.

With reference to Fig. 7.2, that shows the logical correlations among the update

steps both for the UNIFI wear model and the Simpack one, the update step called *Longitudinal integration*, relating to the sum in longitudinal direction of all the wear contributes inside the contact patch, is necessary only in the UNIFI case that using the local wear approach considers the contact patch discretization.

All the further update procedure steps are the same both for the UNIFI procedure and the Simpack one and for the details it can refer to the section 4.3. However same changes to the profile update procedure described in section 4.3 (based on mean wheel and rail profiles as output of the wear model) are necessary to consider different wheel profile evolutions for each vehicle wheelsets and different rail profile evolutions for each N_c representative curve. More specifically the steps called *Average on the wheel-rail pairs* and *Average on the curved tracks of the statistical approach* are replaced by the following single update step as shown in Fig. 7.2:

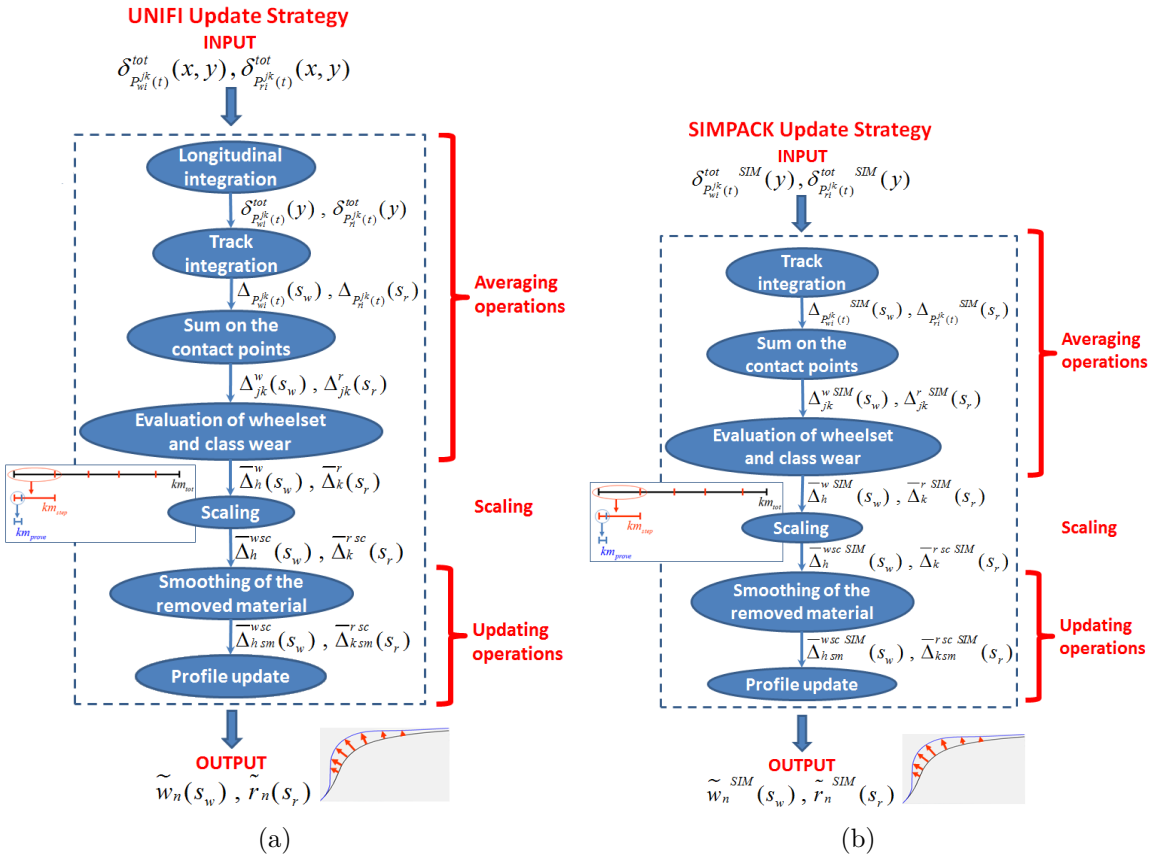

Figure 7.2: Profile update strategy.

- *Evaluation of wheelset wear and class wear*:
  starting from the quantities $\Delta^w_{jk}(s_w)$ $\Delta^r_{jk}(s_r)$ (where $1 \leq j \leq N_w$ and $1 \leq k \leq N_c$ with N_w the vehicle wheels number and N_c the number of the curve classes) obtained by the previous update step *Sum on the contact points* a new index is introduced to indicate the h-th vehicle wheelset; the average on the right and left

wheels of each wheelset (commonly listed with odd and even index respectively [11]) is carried out in order to consider the two-way traffic typical for railways vehicle:

$$\Delta^w_{hk}(s_w) = 1/2 \left(\Delta^w_{(2h)k}(s_w) + \Delta^w_{(2h-1)k}(s_w) \right) \Big|_{h=1}^{N_w/2}. \tag{7.5}$$

Then the following averages to evaluate for each wheelset the mean wear on all the N_c tracks and for each of the N_c classes the mean rail wear (considering all the wheel-rail pairs) have been performed:

$$\sum_{k=1}^{N_c} p_k \Delta^w_{hk}(s_w) = \overline{\Delta}^w_h(s_w) \tag{7.6}$$

$$\frac{1}{N_w} \sum_{j=1}^{N_w} \Delta^r_{jk}(s_r) = \overline{\Delta}^r_k(s_r). \tag{7.7}$$

7.2 The Vivalto Mean Italian Railway Line

To draw up the mean line traveled by the Vivalto composition (E.464 locomotive and Vivalto passenger coach) on the Italian railway network the statistical approach presented in chapter 6 has been exploited. This mean line has to be a significant and equivalent synthesis, in a statistical sense, of the whole set of tracks in Italian railways on which the vehicle composition operates every day.

The whole data were made available by Trenitalia S.p.A. and Rete Ferroviaria Italiana, as electronic databases, paper plans and paper charts of the single tracks. The data are based on the knowledge and the exhaustive analysis of the tracks on which the vehicles operate as well as the relative number of weekly shifts. The shifts are arranged by the district areas of administrative competence of the overall considered railway network, which are six: Florence, Milan, Bologna, Genova, Bari and Rome. The extent of the analyzed data for each district area is summarized in Tab. 7.1, where actually the distances are the sum of the products between the length of the sections and the relative number of weekly shifts, to take into account the service frequency in each track.

Starting from the real data the representative N_c classes of curves statistically equivalent to the Italian network and characterizing by suitable radius values R_c, superelevation values H_c, vehicle velocity V_c and the statistical weights p_k are extracted. In particular, for the present case the class number parameter has been chosen equal to $n_{class} = 8$; the consequent track representation, made up of $N_c = 28$ different classes (27 curvilinear tracks and the straight one), is shown in Tab. 7.2.

Table 7.1: Percentage of analyzed data for the Vivalto composition vehicle.

District area	**Analyzed distance** (km)	**Total distance** (km)	%
Florence	17934	21588	83.1
Milan	5261	8206	64.1
Bologna	11235	14547	77.2
Genova	1636	1712	95.5
Bari	4667	4668	99.9
Rome	33195	103257	32.1
Total	73929	153978	48.0

7.3 Results Comparison

The results obtained with the UNIFI wear model will be shown and compared with the Simpack wear model ones. In the present part of the research activity the wheel and rail steps number n_{sw}, n_{sr} and consequently suitable values for the wheel and rail wear thresholds D^w_{step}, D^r_{step} have been chosen as shown in Tab. 7.3, to perform the dynamic analyses according to the simulation algorithm described in section 4.4.

Table 7.2: Virtual tracks.

$\mathbf{R}_{min}$ (m)	$\mathbf{R}_{max}$ (m)	**Superelevation** $h_{min} - h_{max}$ (mm)	$\mathbf{R}_c$ (m)	$\mathbf{H}_c$ (mm)	$\mathbf{V}_c$ (km/h)	$\mathbf{p}_k$ %
278	316	100–119	**294**	110	70	0.04
		120–139		135	75	0.03
316	367	120–139	**333**	124	75	0.74
		140–160		153	85	0.74
367	438	60–79	**400**	66	70	0.82
		80–99		90	70	0.07
		140–160		152	85	0.19
438	541	40–59	**485**	50	70	0.03
		120–139		126	90	0.20
		140–160		150	100	1.76
541	709	20–39	**616**	30	70	0.02
		60–79		66	70	0.15
		120–139		123	95	0.36
		140–160		144	105	1.29
709	1026	20–39	**845**	24	70	0.03
		60–79		74	90	0.25
		80–99		90	95	1.14
		140–160		151	130	1.93
1026	1862	40–59	**1360**	43	70	0.63
		80–99		86	105	1.87
		120–139		124	130	1.80
		140–160		152	150	2.78
1862	10000	0–19	**4590**	5	70	0.60
		20–39		34	95	3.96
		40–59		45	140	2.12
		60–79		72	160	1.27
		80–99		90	160	1.78
10000	∞				160	72.4

Table 7.3: Simulation algorithm parameters.

Parameter		Value
Number of discrete step	n_{sw}	15
	n_{sr}	5
Wear threshold	D^w_{step}	0.4 mm
	D^r_{step}	0.8 mm

7.3.1 Evolution of Wear Control Parameter

In this section the evolution both of the wheel reference quotas (flange thickness FT, flange height FH and flange steepness QR) and of the rail reference quota QM numerically will be presented. The wheel quotas are shown as a function of the n_{sw} wheel steps while the QM parameter is shown as a function of the rail steps n_{sr}. To focus on the main physical effects due to wear evolution avoiding dispersion in the results description, only the wheel quotas related to the former and the latter rail steps (r_{k0} and r_{k4}) will be shown together with the rail quota QM related to only three of the N_c curves; the considerations on the wheel and rail wear evolution as function of the traveled distance will be presented at the end of this section considering the difference between the discrete step lengths calculated by the two models.

In Fig. 7.3-7.6 the comparison between the FT dimensions for the two wheelsets of the front bogie of the E.464 locomotive and of the Vivalto coach is presented. As it can be seen the thickness of the leading wheel (w_{1i}, ${w_{1i}}^{SIM}$) decreases more than the same quantity of the rear wheel (w_{2i}, ${w_{2i}}^{SIM}$) for both the vehicles. It is due to the vehicle dynamics that causes different load distribution on the wheels and to the particular position of the wheelsets inside the bogie; the rear wheels of each bogie have a smooth curve entry because of the guide effect of the bogie itself with a consequent less wear stress respect to the leading wheels.

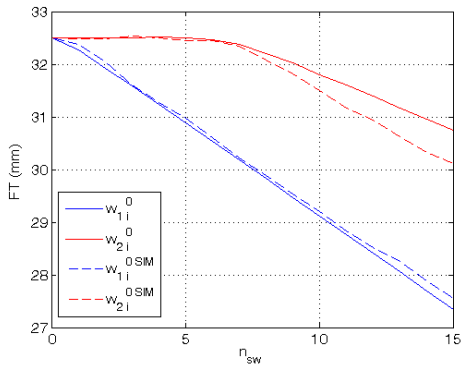

Figure 7.3: E.464 vehicle: FT progress at r_{k0} rail step.

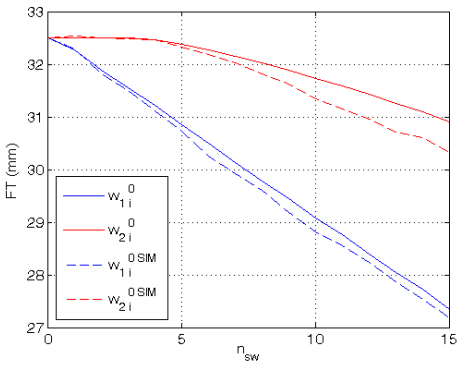

Figure 7.4: Vivalto vehicle: FT progress at r_{k0} rail step.

The FH quota progresses are represented in Fig. 7.7-7.10 and show that the wheel

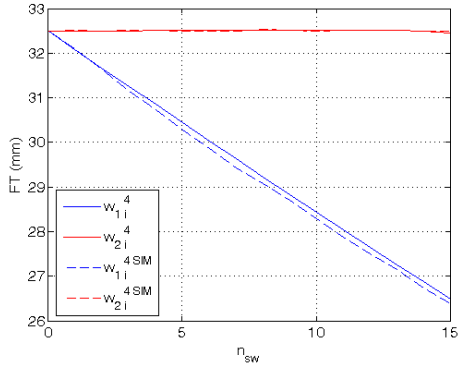

Figure 7.5: E.464 vehicle: FT progress at r_{k4} rail step.

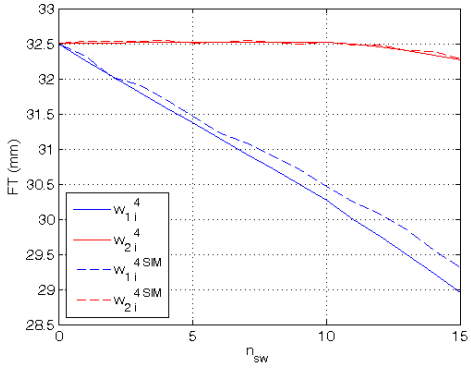

Figure 7.6: Vivalto vehicle: FT progress at r_{k4} rail step.

wear on the tread is appreciable mainly for the first rail step (i.e. UIC 60 unworn rail profile). The considered scenario (Vivalto composition traveled on the mean Italian railway line) is mainly made up of straight and large curves radius tracks (almost the 90% of the network is characterized by curve radius values greater than 1000m) and thus the wheel-rail contact evolve mainly in the wheel tread zone. However the more conformal contact between wheel and rail surface as the rail wear increases lead to a wear rate reducing on the wheel tread. Also the FH dimension displays more wear on the leading wheel while for the rear wheel the tread wear is lower in all studied cases.

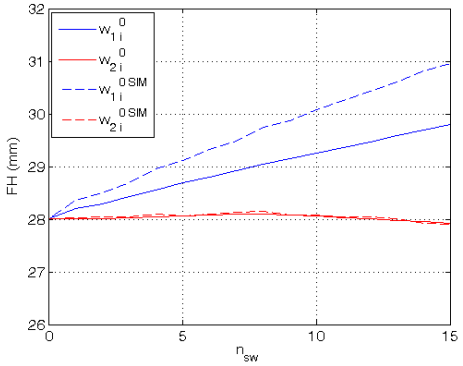

Figure 7.7: E.464 vehicle: FH progress at r_{k0} rail step.

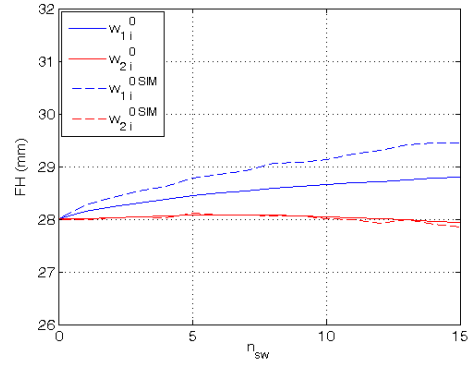

Figure 7.8: Vivalto vehicle: FH progress at r_{k0} rail step.

The QR trend are shown in Fig. 7.11-7.14; the flange steepness decreases leading to an increase of the conicity of the flange; also for this dimension the considerations related to the leading and rear wheels hold.

In Fig. 7.15 the QM evolution for the rail wear investigation can be seen: for the sake of clarity the wear progress of only three of the N_c curves are represented (the first, the 14th and the 27th). The QM trend shows that the rail wear increases if the curve radius decreases according with the real wear phenomena (see Tab. 7.2: r_{1j} is

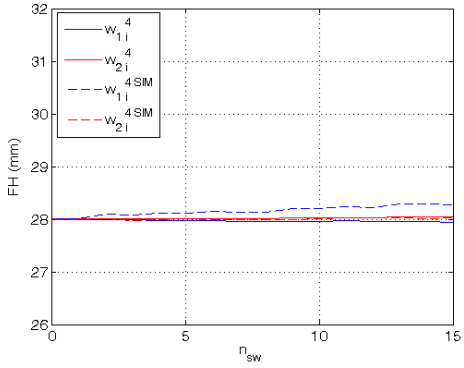

Figure 7.9: E.464 vehicle: FH progress at r_{k4} rail step.

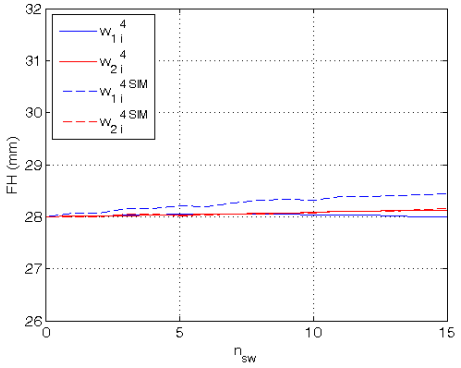

Figure 7.10: Vivalto vehicle: FH progress at r_{k4} rail step.

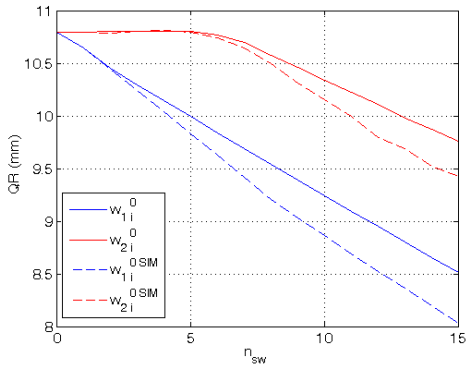

Figure 7.11: E.464 vehicle: QR progress at r_{k0} rail step.

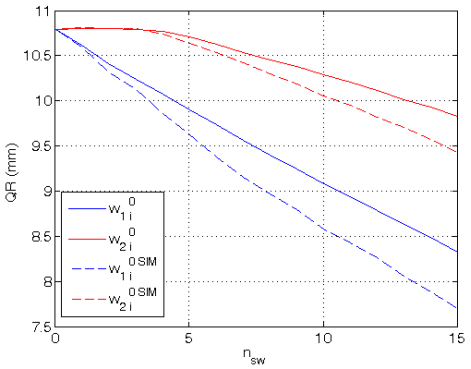

Figure 7.12: Vivalto vehicle: QR progress at r_{k0} rail step.

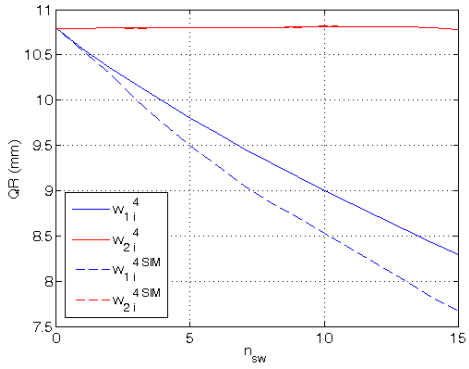

Figure 7.13: E.464 vehicle: QR progress at r_{k4} rail step.

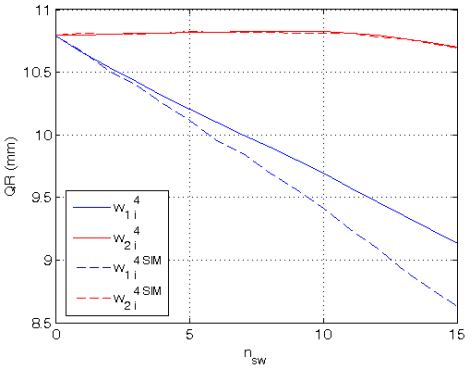

Figure 7.14: Vivalto vehicle: QR progress at r_{k4} rail step.

referred to the minimum curve radius, r_{14_j} to an intermediate one while r_{27_j} to the maximum curve radius).

In conclusion the comparison of the reference dimensions leads to a good qualitative agreement between the developed wear model and the Simpack one; both show the same wear behavior concerning leading and rear wheelsets, contact conformity and

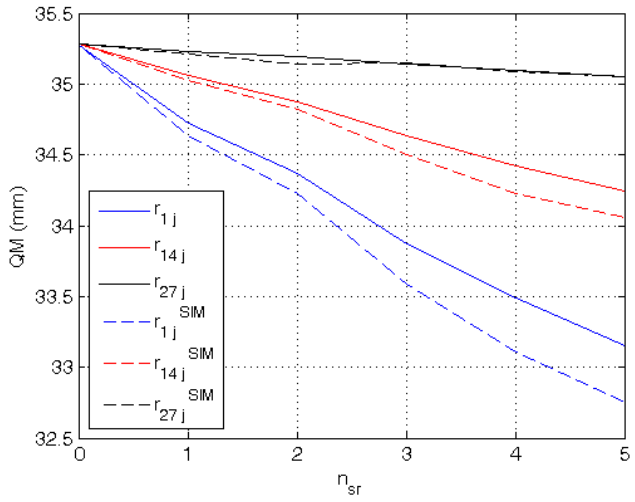

Figure 7.15: QM progress.

curve radius.

In Fig. 7.16 the evolution of the km_{step} as a function of the wheel discrete step number n_{sw} is shown (for clarity only the km_{step} related to the former and the latter rail step are presented). Related to the first rail step r_{k0}, the lower km_{step} values and their higher gradient in the first wheel steps indicate the higher wear rate due to the initial non conformal contact characterizing the coupling between the new ORE S1002 wheel profile and the rail profile UIC 60 with laying angle equal to 1/20rad; the almost constant values in the latter steps (combined with higher km_{step} values) show at the same time the achievement of a more and more conformal contact as the wheel wear increases. Considering the latter rail step r_{k4} the same curve trend can be seen but characterized by higher km_{step} values because of the worn rail profile that leads to an initial more conformal contact than the previous case. In Fig. 7.17 the evolution of the N_{step} as a function of the rail discrete number n_{sr} is shown and it can be seen that the considerations referred to the variation of the contact conditions (i.e. non conformal and conformal contact) hold also in this case.

The Tabs. 7.4-7.5 show the overall mileages km^j_{tot} traveled by the vehicle composition for each rail step r_{kj} and the total vehicle number N_{tot} burden on the track during the overall wear loop. The increase of the total mileage as the rail profile is more and more worn is caused, as stated above, by the increase of the conformity between wheel and rail surfaces.

Table 7.4: Evolution of the total mileage km_{tot}.

Wear Model	km^0_{tot}(km)	km^1_{tot}(km)	km^2_{tot}(km)	km^3_{tot}(km)	km^4_{tot}(km)
UNIFI	81460	88120	94350	102080	108950
Simpack	78530	84870	92020	98210	102790

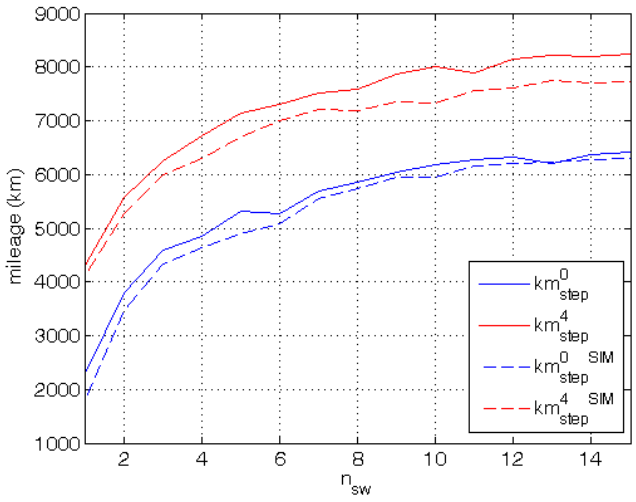

Figure 7.16: Evolution of the km_{step}.

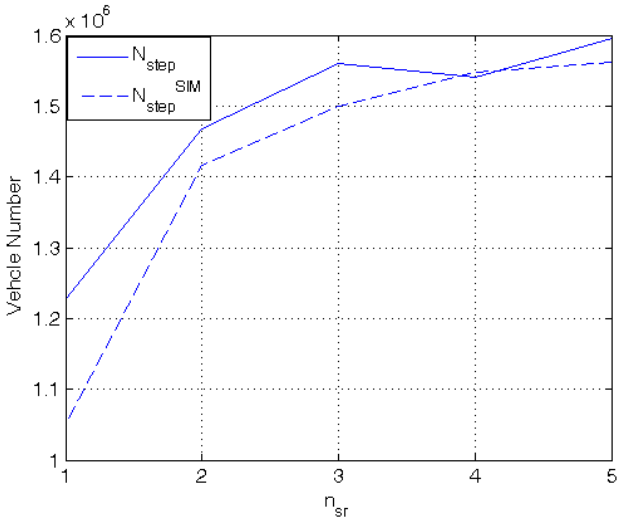

Figure 7.17: Evolution of the N_{step}.

Table 7.5: Evolution of the total vehicle number N_{tot}.

Wear Model	N_{tot}
UNIFI	7390900
Simpack	7074500

Finally, analyzing the difference between the UNIFI and the Simpack model the Fig. 7.16 shows slightly lower km_{step} values in the Simpack case that indicate an increase of the wheel wear rate due to a probable wear overestimation caused by the global wear approach of the Simpack model that, not considering the subdivision of the contact patch in slip and adhesion zone, leads to subtract the mean removed material due to wear in overall the contact patch itself; the same observation holds for the vehicle number N_{step} as can be seen in Fig. 7.17.

7.3.2 Evolution of the Wheel and Rail Profile

The wear evolution on the wheel profiles evolving on the first and on the latter rail steps r_{k0}, r_{k4} for the wheelsets of the front bogie of both E.464 and Vivalto vehicles is presented in the Figs. 7.18-7.33. As stated previously, the wheel profile evolution is described by means of $n_{sw} = 15$ steps and the threshold on the removed material for each step D^w_{step} has been chosen equal to 0.4mm. From the figures it can be seen both the wear increase on the leading wheel with respect to the rear wheel of the bogie and the wheel tread wear decrease when the wheel is coupled with the worn rail profile r_{k4} (with respect to the unworn profile r_{k0}) due to the achievement of a more conformal contact in the wheel-rail pairs.

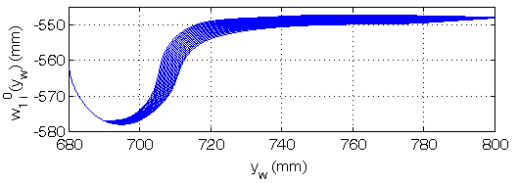

Figure 7.18: UNIFI model: E.464 $w_{1_i}^0$ profile evolution.

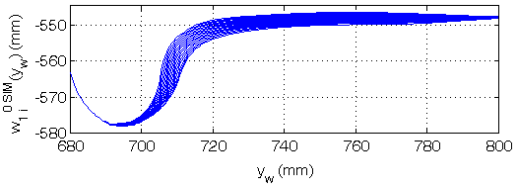

Figure 7.19: Simpack model: E.464 $w_{1_i}^0$ profile evolution.

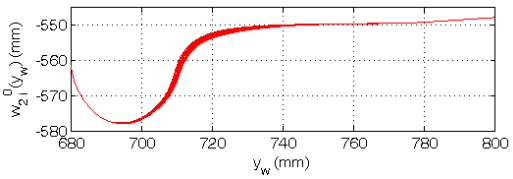

Figure 7.20: UNIFI model: E.464 $w_{2_i}^0$ profile evolution.

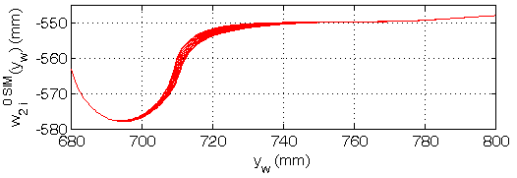

Figure 7.21: Simpack model: E.464 $w_{2_i}^0$ profile evolution.

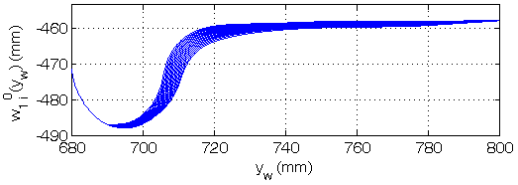

Figure 7.22: UNIFI model: Vivalto $w_{1_i}^0$ profile evolution.

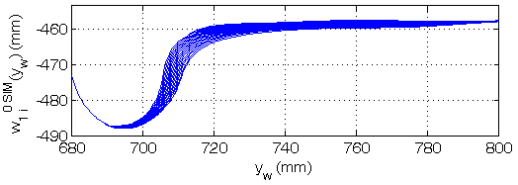

Figure 7.23: Simpack model: Vivalto $w_{1_i}^0$ profile evolution.

By way of example, the Figs. 7.34-7.35 show the cumulative distributions of removed material in vertical direction z_w on the leading wheel profile of the E.464 locomotive at the first and at the last rail step $\sigma_{w1_{Kw}}{}^0(y_w) = \sum_{i=1}^{Kw} \sigma_i^{w1\,0}(y_w)$ and $\sigma_{w1_{Kw}}{}^{n_{sr}-1}(y_w) = \sum_{i=1}^{Kw} \sigma_i^{w1\,n_{sr}-1}(y_w)$ $(1 \leq Kw \leq n_{sw})$ as a function of y_w; $\sigma_i^{w1\,j}(y_w)$ is the removed material between two subsequent discrete steps of the leading wheel profile evolution (the $i-th$ and the $(i-1)-th$ wheel discrete steps) at the $j-th$

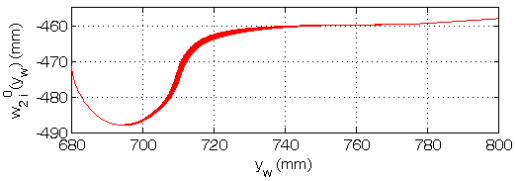

Figure 7.24: UNIFI model: Vivalto $w_{2_i}^0$ profile evolution.

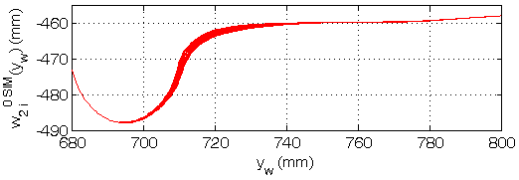

Figure 7.25: Simpack model: Vivalto $w_{2_i}^0$ profile evolution.

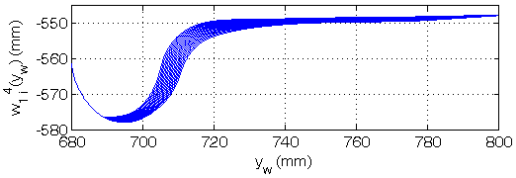

Figure 7.26: UNIFI model: E.464 $w_{1_i}^4$ profile evolution.

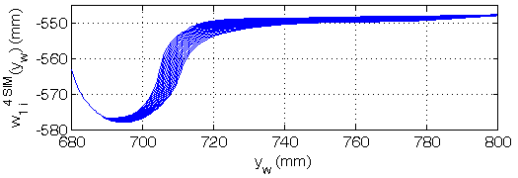

Figure 7.27: Simpack model: E.464 $w_{1_i}^4$ profile evolution.

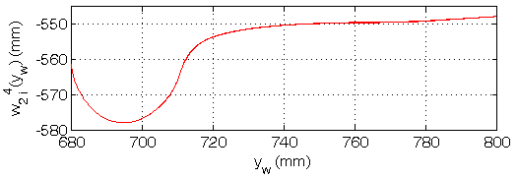

Figure 7.28: UNIFI model: E.464 $w_{2_i}^4$ profile evolution.

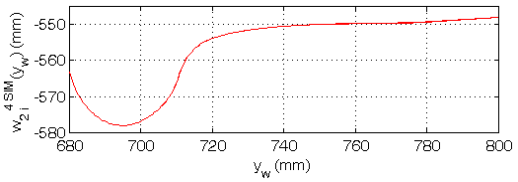

Figure 7.29: Simpack model: E.464 $w_{2_i}^4$ profile evolution.

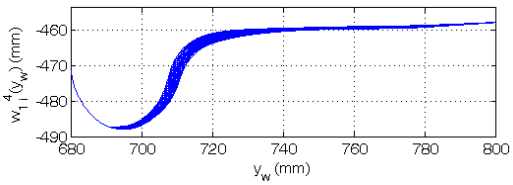

Figure 7.30: UNIFI model: Vivalto $w_{1_i}^4$ profile evolution.

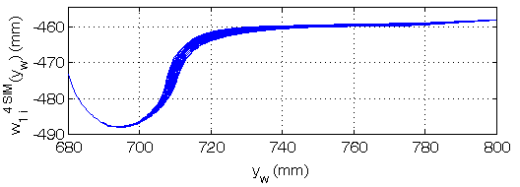

Figure 7.31: Simpack model: Vivalto $w_{1_i}^4$ profile evolution.

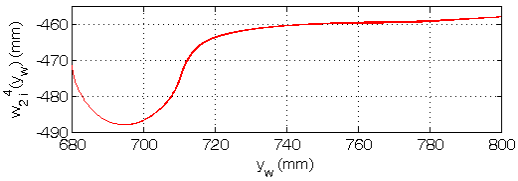

Figure 7.32: UNIFI model: Vivalto $w_{2_i}^4$ profile evolution.

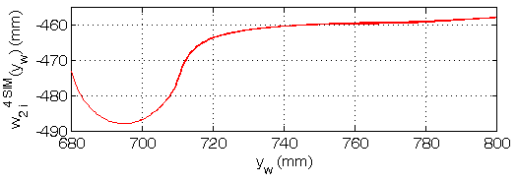

Figure 7.33: Simpack model: Vivalto $w_{2_i}^4$ profile evolution.

rail step ($0 \leq j \leq n_{sr} - 1$) (for reasons of clarity only the distributions characterized by $Kw = 1{,}8{,}n_{sw}$ are represented). The cumulative distributions highlight the reduction of removed material on the wheel tread as the contact becomes more and more conformal.

In Figs. 7.36-7.41 the rail profile evolutions related to the three different curves

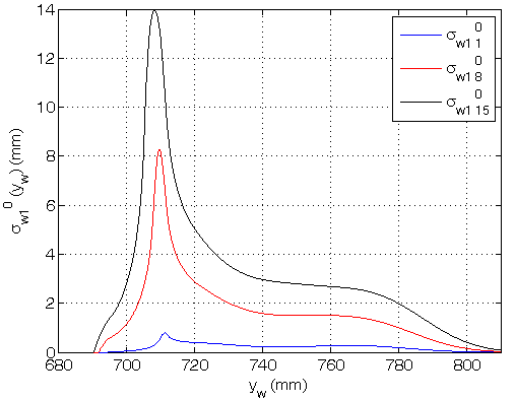

Figure 7.34: UNIFI model: E.464 cumulative distributions $\sigma_{w1_i}^{0}$ of the removed wheel material.

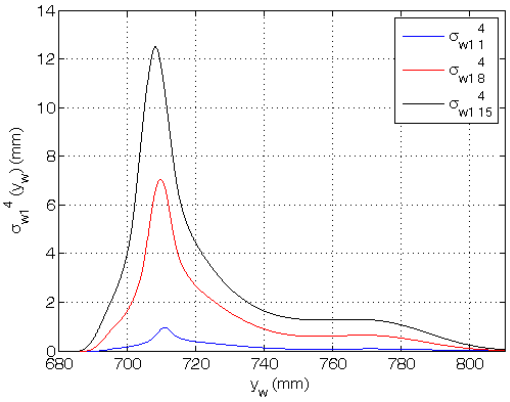

Figure 7.35: UNIFI model: E.464 cumulative distributions $\sigma_{w1_i}^{4}$ of the removed wheel material.

of the statistical analysis r_{1_j}, r_{14_j} and r_{27_j} are presented; the removed material due to wear shows a rather clear dependence from the curve radius and in particular the wear increases in the sharp curves because of the resulting vehicle dynamics and harder contact conditions. For instance, the Fig. 7.42 shows the cumulative distributions of removed material on the rail (in vertical direction z_r) of the first curve of the statistical analysis $\sigma_{r1_{Kr}}(y_r) = \sum_{j=1}^{Kr} \sigma_j^{r1}(y_r)$ as a function of y_r $(1 \leq Kr \leq n_{sr})$; $\sigma_j^{r1}(y_r)$ is the removed material between two subsequent discrete steps of the rail profile evolution (the $j-th$ and the $(j-1)-th$ rail discrete steps).

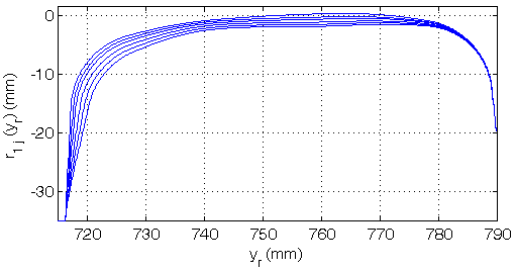

Figure 7.36: UNIFI model: r_{1_j} profile evolution.

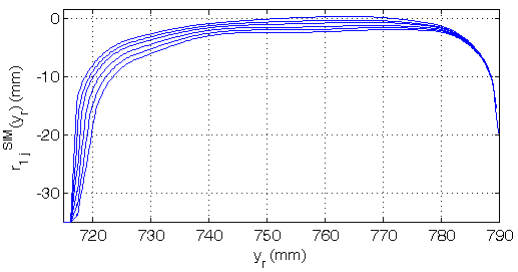

Figure 7.37: Simpack model: ${r_{1_j}}^{SIM}$ profile evolution.

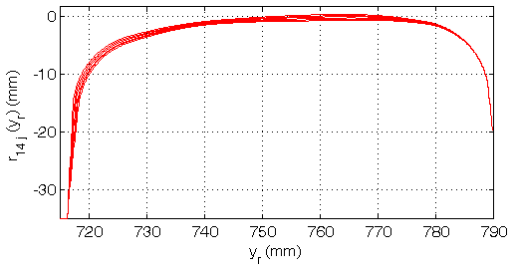

Figure 7.38: UNIFI model: r_{14_j} profile evolution.

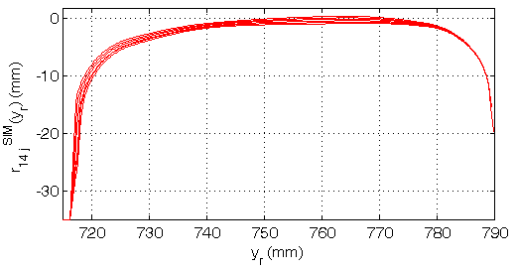

Figure 7.39: Simpack model: ${r_{14_j}}^{SIM}$ profile evolution.

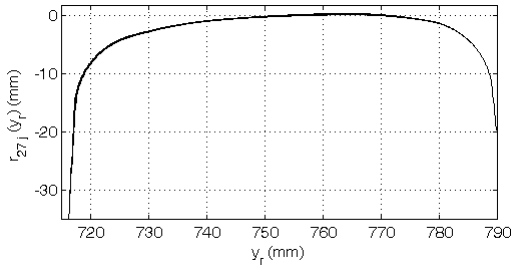

Figure 7.40: UNIFI model: r_{27_j} profile evolution.

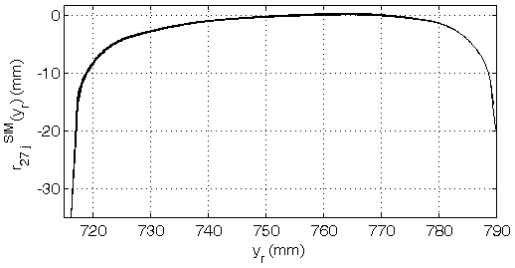

Figure 7.41: Simpack model: ${r_{27_j}}^{SIM}$ profile evolution.

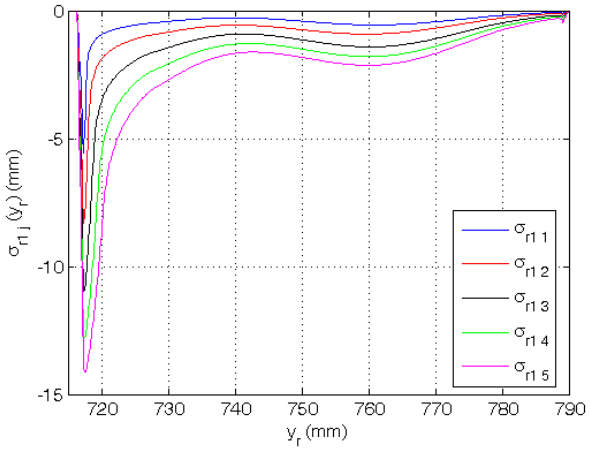

Figure 7.42: UNIFI model: cumulative distributions σ_{r1_j} of the removed rail material.

In all the studied cases the comparison between the profile evolution obtained with the innovative developed wear model and the Simpack one results rather satisfactory without pronounced differences.

7.3.3 Computational Effort

The characteristics of the processor used in the simulations and the mean computational times relative to each discrete step of the whole model loop (dynamical simulation and wear simulation including both wheel and rail procedures as described in detail in section 4.4) are schematically summarized in Tab. 7.6 both for the innovative developed model and for the Simpack model. The main numerical parameters relative to the integrator used for the dynamical simulations of both the models are briefly reported in Tab. 7.7.

The UNIFI dynamic simulation, thanks to the high numerical efficiency of the new global contact model (see section 3.2), is rather faster than the Simpack one despite the latter uses approximated look-up tables for evaluating the global contact parameters. In particular the analytical reduction of the algebraic contact problem dimension (from 4D to 1D scalar problem) performed in the UNIFI global contact model implies both an

Table 7.6: Computational time.

Wear Model	Processor	Computational time		
		Dynamic simulation	Wear simulation	Total time reduction
UNIFI	INTEL Xeon CPU E 5430 2.66 GHz 8GB RAM	38min	9min	−29%
Simpack		1h 2min	4min	-

Table 7.7: Integrator parameters.

Integrator type	ODE5
Alghoritm	Dormand-Prince
Order	5
Step type	fixed
Stepsize	10^{-4} s

increase of the model efficiency and a simplified treatment of the multiple contact, with a consequent computational time reduction. Moreover the UNIFI innovative algorithm is implemented directly online trough C/C++ user routine strongly integrated within Simpack environment that, consequently, leads to an important improve in terms of computational load and memory consumption (no heavy LUTs are used). On the other hand the approximation due to the global wear evaluation approach of the Simpack model leads to a lower wear simulation time than the UNIFI model where the contact patch investigation obviously has an impact on the computational load. Finally the UNIFI model shows a considerable computational time reduction if compared to the Simpack model (almost 30%).

In conclusion the results showed in this chapter highlight how the innovative model reflects the real behavior of the wear phenomena (for example an higher removed material for the leading wheel and for the sharp curves and a wear rate decrease when the contact conditions reach the conformal contact). The comparison with the Simpack wear model has given satisfactory results both in terms of reference dimensions and profiles evolution; the only difference is a little wear overestimation of the SIMPACK model probably due to the approximated global wear approach that does not consider the division of the contact patch in adhesion and slip zone. Moreover the innovative model highlights better performance in terms of computational efficiency with a considerable time reduction respect to the Simpack wear model.

Chapter 8

Industrial Applications of the Wear Model

This chapter treats some possible applications of the innovative wear model in industrial field. Wear phenomena due to wheel-rail interaction represent a critical aspect in railway branch because of the evolution of rail and wheel profiles that involves serious effects on both dynamical and stability characteristics of vehicles. From a safety viewpoint, modifications in wheel and rail profiles may compromise the vehicle stability and also increase the derailment risk due to wheels climbing over the rail. Profile changes lead also to higher maintenance cost, mainly concerned with the periodically re-profiling operations of wheels and the undesirable replacements of rails, necessary to re-establish the original profiles.

A main strengths of a reliable wear model is represented by the research of optimized shape profiles of wheel and rail to obtain a more uniform wear on rolling surfaces. In such a way the overall amount of worn material can be reduced, the mean time between two maintenance interventions can be increased and, at the same time, the dynamical performance of the wheel-rail pair can be kept approximately constant between two succeeding repair interventions. The optimum matching is usually pursued through the design of new wheel profiles which matches an existing rail profile, because the cost of rail interventions is notably higher compared with the cost of turning or replacement of the wheels; several works, based on the rolling radii difference, contact angle, equivalent conicity or wheel/rail gap minimization can be found in the literature [6][18][31][34]. In this chapter will be presented a new optimization procedure designed in collaboration with Trenitalia and RFI that, with respect to the state of the art, introduces innovative features and permits to work directly on the contact point and on their distribution, with a consequent improvement in terms of wear control, stability and guidance. The wear model is employed to assess the performance in terms of wear of the new wheel profile shapes [45][46][47].

In the last part of the chapter another interesting application will be presented; the

wear model will be used as an aid in the vehicle design to predict the wheel re-profiling intervals.

8.1 Wheel Profile Optimization Procedure

The procedures for the design of the proposed wheel profile, named DR2 wheel profile will be described in detail [45][46][47]. These procedures have been developed in collaboration with Trenitalia and RFI [40] with the aim of improving the poor performance with regard to the resistance to wear and the guidance in sharp curves that the ORE S1002 wheel profile, originally designed to match the UIC 60 rail profile canted at 1/40rad, exhibits when coupled to the UIC 60 rail profile canted at 1/20rad (the latter wheel-rail matching represents the standard adopted in the Italian railway line).

8.1.1 DR2 Wheel Profile

The design of the DR2 wheel profile aims to guarantee the kinematic characteristics of the original matching formed by ORE S1002 wheel profile and UIC 60 rail profile with laying angle α_p equal to 1/40rad, also with the new matching DR2 wheel profile - UIC6 0 rail profile canted at 1/20rad. The kinematic properties of the original matching have been chosen as reference value, because it is widely common in European railways and it is characterized by good performances in both wear and kinematic behavior.

The procedure developed by the authors to design the DR2 wheel profile is articulated in several steps. A first intermediate wheel profile, conventionally named DR1, is designed according to the purposes previously described. The resulting rolling radii difference function (RRD) (the difference between rolling radii of the right and the left wheels for each lateral displacement y), is then compared with the one characterizing the original wheel and rail profiles matching and a rolling radii difference error function is obtained. The minimization of the error function through an appropriate algorithm leads then to the optimized version of the wheel profile, conventionally named DR2.

The design of the DR2 profile exploits the two appropriate reference systems already used to describe the global contact point detection algorithm (see paragraph 3.2.1), namely auxiliary (or rail) reference system $O_r x_r y_r z_r$ and local (or wheel) reference system $O_w x_w y_w z_w$, both shown in Fig. 8.1. The position of the local reference system origin expressed in the auxiliary reference system is denoted by:

$$\mathbf{O}_w^r = [\ y \quad z(y)\ ]^T. \tag{8.1}$$

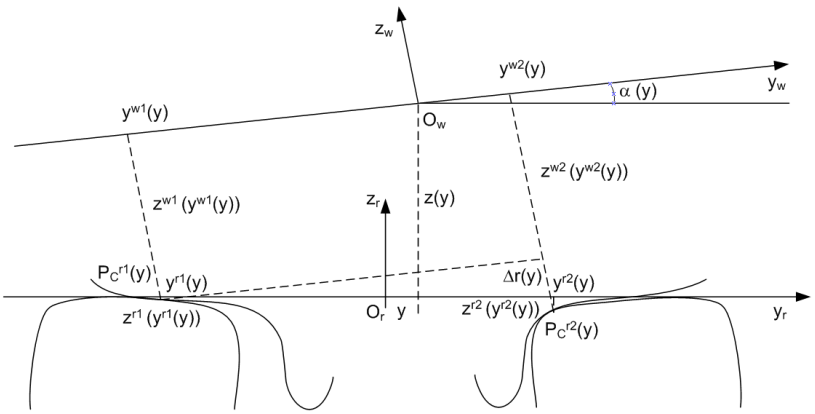

Figure 8.1: Adopted nomenclature for DR2 design.

Introducing apexes 1 and 2 to denote respectively the right and left wheel, the coordinates of the contact points respectively in the auxiliary reference and the local reference system may be defined as:

$$\begin{aligned} \mathbf{P}_c^{r1} &= [\ y^{r1}(y) \quad z^{r1}(y^{r1}(y))\ ]^T & \mathbf{P}_c^{w1} &= [\ y^{w1}(y) \quad z^{w1}(y^{w1}(y))\ ]^T \\ \mathbf{P}_c^{r2} &= [\ y^{r2}(y) \quad z^{r2}(y^{r2}(y))\ ]^T & \mathbf{P}_c^{w2} &= [\ y^{w2}(y) \quad z^{w2}(y^{w2}(y))\ ]^T. \end{aligned} \tag{8.2}$$

Design of the DR1 wheel profile

The purpose in maintaining the kinematic properties of the ORE S1002-UIC 60 canted at 1/40rad matching is achieved by imposing that some variables of the new matching (DR2 wheel profile - UIC 60 matching canted at 1/20rad) remain the same of the original ones. More specifically these variables (all depending on the wheelset lateral displacement y) are the lateral coordinates $y^{r1}(y)$, $y^{r2}(y)$ of the contact points expressed in the auxiliary reference system, the vertical coordinate $z(y)$ and the roll angle $\alpha(y)$ of the wheelset. In the remaining of the chapter the variables characterizing the original matching and those referring to the new matching will be respectively denoted with the subscripts 40 and 20.

Consequently the six inputs required by the design procedure from the old matching are $y_{40}^{r1}(y)$, $y_{40}^{r2}(y)$, $\alpha_{40}(y)$, $z_{40}(y)$ and the rail functions $z_{40}^{r1}(y_{40}^{r1}(y))$, $z_{40}^{r2}(y_{40}^{r2}(y))$ while the two further inputs required from the new matching are $z_{20}^{r1}(y_{40}^{r1}(y))$, $z_{20}^{r2}(y_{40}^{r2}(y))$.

The DR1 wheel profile design procedure is formed by the following steps:

1. evaluation of the lateral $y_{20}^{w1}(y)$, $y_{20}^{w2}(y)$ and vertical $z_{20}^{w1}(y_{20}^{w1}(y))$, $z_{20}^{w2}(y_{20}^{w2}(y))$ coordinates of the contact points of the new wheel profile in the local reference system;

2. filling of the hole regions of the resulting profiles;

3. evaluation of the RRD functions characterizing the new wheel profile.

Step 1: Evaluation of the lateral and vertical coordinates of the contact points of the new wheel profile

Starting from the inputs, the equations describing the coordinate transformation of the contact points between the local and the auxiliary reference system can be written both for the original matching:

$$\begin{pmatrix} y_{40}^{r1}(y) \\ z_{40}^{r1}(y_{40}^{r1}(y)) \end{pmatrix} = \begin{pmatrix} y \\ z_{40}(y) \end{pmatrix} + R(\alpha_{40}(y)) \begin{pmatrix} y_{40}^{w1}(y) \\ z_{40}^{w1}(y_{40}^{w1}(y)) \end{pmatrix} \tag{8.3}$$

$$\begin{pmatrix} y_{40}^{r2}(y) \\ z_{40}^{r2}(y_{40}^{r2}(y)) \end{pmatrix} = \begin{pmatrix} y \\ z_{40}(y) \end{pmatrix} + R(\alpha_{40}(y)) \begin{pmatrix} y_{40}^{w2}(y) \\ z_{40}^{w2}(y_{40}^{w2}(y)) \end{pmatrix} \tag{8.4}$$

and for the new matching:

$$\begin{pmatrix} y_{40}^{r1}(y) \\ z_{20}^{r1}(y_{40}^{r1}(y)) \end{pmatrix} = \begin{pmatrix} y \\ z_{40}(y) \end{pmatrix} + R(\alpha_{40}(y)) \begin{pmatrix} y_{20}^{w1}(y) \\ z_{20}^{w1}(y_{20}^{w1}(y)) \end{pmatrix} \tag{8.5}$$

$$\begin{pmatrix} y_{40}^{r2}(y) \\ z_{20}^{r2}(y_{40}^{r2}(y)) \end{pmatrix} = \begin{pmatrix} y \\ z_{40}(y) \end{pmatrix} + R(\alpha_{40}(y)) \begin{pmatrix} y_{20}^{w2}(y) \\ z_{20}^{w2}(y_{20}^{w2}(y)) \end{pmatrix} \tag{8.6}$$

where the wheelset lateral displacement value y is bounded in the range $[-y_M,y_M]$. The outputs of the design procedure that characterize the new wheel profile are the lateral $y_{20}^{w1}(y)$, $y_{20}^{w2}(y)$ and vertical $z_{20}^{w1}(y_{20}^{w1}(y))$, $z_{20}^{w2}(y_{20}^{w2}(y))$ coordinates of the contact points of the new wheel profile in the local reference system. The design procedure is performed in a discrete way for every y value of the discretized range $[-y_M,y_M]$ (with a resolution equal to 0.1 mm).

Step - 2: Filling of the hole regions of the resulting profiles

The profile resulting from the previous step is characterized by holes (see Fig. 8.2a), that are regions where there is not any computed contact point. In the present procedure these regions have been filled fitting the computed points with spline functions and the resulting wheel profile, named DR1, is illustrated in Fig. 8.2b.

Step 3: Evaluation of the RRD functions characterizing the new wheel profile

The RRD functions characterizing the original (ORE S1002 wheel profile and UIC 60 canted at 1/40rad) and the resulting matching are respectively defined through the following expressions (see Fig. 8.3):

$$\Delta r_{40} = z_{40}^{w2}(y_{40}^{w2}(y)) - z_{40}^{w1}(y_{40}^{w1}(y)) \qquad \Delta r_{20} = z_{20}^{w2}(y_{20}^{w2}(y)) - z_{20}^{w1}(y_{20}^{w1}(y)). \tag{8.7}$$

The adopted design procedure implies that the rolling radii difference of the output

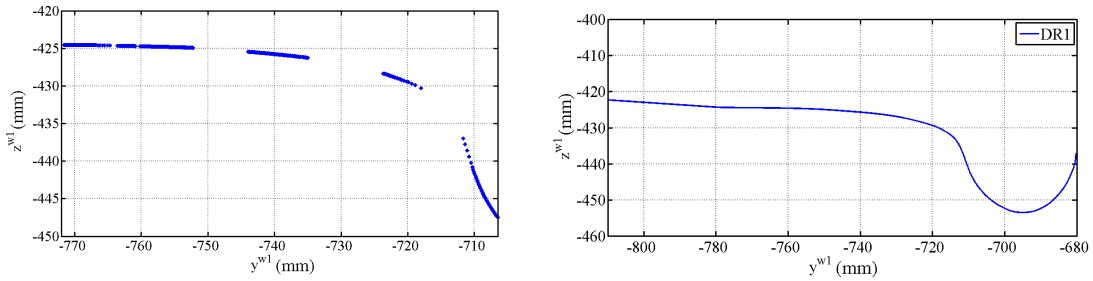

Figure 8.2: DR1 wheel profile design (a): contact points distribution (b): DR1 wheel profile.

matching is equal to the one characterizing the original matching, disregarding a small estimable variation $e = \Delta r_{20} - \Delta r_{40}$ (see Fig. 8.4), calculated by means of an appropriate analytical procedure.

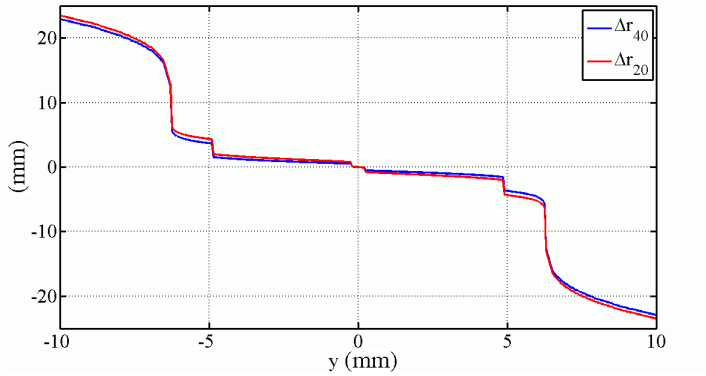

Figure 8.3: Rolling radii differences: $\Delta\ r_{20} = z_{20}^{w2}(y_{20}^{w2}(y)) - z_{20}^{w1}(y_{20}^{w1}(y))$ relative to the matching DR1-UIC 60 canted at $1/20$rad and $\Delta\ r_{40} = z_{40}^{w2}(y_{40}^{w2}(y)) - z_{40}^{w1}(y_{40}^{w1}(y))$ relative to the ORE S1002-UIC 60 rail canted at $1/40$rad.

Optimization of the wheel profile and design of DR2 wheel profile

In order to improve the rolling radii difference error between the original matching and DR1 wheel profile - UIC 60 canted at $1/20$rad matching, an optimization algorithm has been developed according to the following steps:

1. expression of the rolling radii functions variation between the new and the original matching as a function of the wheelset lateral displacement;

2. minimization process of the RRD function error to evaluate the optimum translation $k(y)$ and translation of the lateral input coordinates $y_{40}^{r1}(y)$, $y_{40}^{r2}(y)$ of the quantity $k(y)$;

3. optimization process and re-definition of the resulting lateral coordinates of the contact points in the auxiliary reference system;

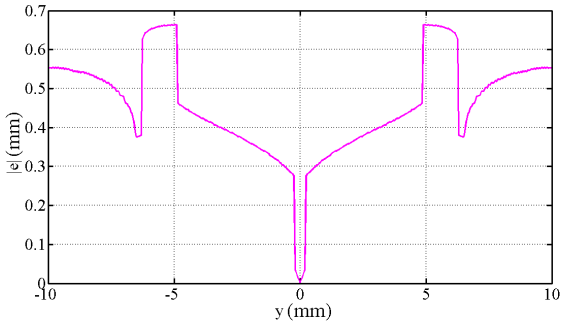

Figure 8.4: Absolute value of the error e in rolling radii difference distribution for the DR1-UIC 60 canted at $1/20\text{rad}$ matching.

4. computation of the outputs characterizing the optimized wheel profile;

5. holes fitting procedure;

6. evaluation of the new RRD function.

Step 1: Expression of the rolling radii functions variation between the new and the original matching

An expression of the RRD functions variation between the new and the original matching can be obtained. Subtracting the Eq. 8.3 from the Eq. 8.4 and the Eq. 8.5 from the Eq. 8.6, it leads to the following expressions:

$$\begin{pmatrix} y_{40}^{r2}(y) - y_{40}^{r1}(y) \\ z_{40}^{r2}(y_{40}^{r2}(y)) - z_{40}^{r1}(y_{40}^{r1}(y)) \end{pmatrix} = R(\alpha_{40}) \begin{pmatrix} y_{40}^{w2}(y) - y_{40}^{w1}(y) \\ \Delta r_{40} \end{pmatrix} \tag{8.8}$$

$$\begin{pmatrix} y_{40}^{r2}(y) - y_{40}^{r1}(y) \\ z_{20}^{r2}(y_{40}^{r2}(y)) - z_{20}^{r1}(y_{40}^{r1}(y)) \end{pmatrix} = R(\alpha_{40}) \begin{pmatrix} y_{20}^{w2}(y) - y_{20}^{w1}(y) \\ \Delta r_{20} \end{pmatrix}. \tag{8.9}$$

Then, subtracting on turn the Eq. 8.8 from the Eq. 8.9 it holds:

$$R^T(\alpha_{40}) \begin{pmatrix} 0 \\ \Delta z_{20}^r - \Delta z_{40}^r \end{pmatrix} = \begin{pmatrix} \Delta y_{20}^w - \Delta y_{40}^w \\ \Delta r_{20} - \Delta r_{40} \end{pmatrix}. \tag{8.10}$$

The second component of the previous equation leads to the expression of the rolling radii functions variation between the new and the original matching

$$(\Delta z_{20}^r - \Delta z_{40}^r)\cos\alpha_{40} = \Delta r_{20} - \Delta r_{40} = e(y) \tag{8.11}$$

as a function of the wheelset lateral displacement where $\Delta z_{20}^r = z_{20}^{r2}(y_{40}^{r2}(y)) - z_{20}^{r1}(y_{40}^{r1}(y))$ and $\Delta z_{40}^r = z_{40}^{r2}(y_{40}^{r2}(y)) - z_{40}^{r1}(y_{40}^{r1}(y))$.

Step - 2: Minimization process of the RRD function error to evaluate the quantity $k(y)$ and translation of the lateral input coordinates $y_{40}^{r1}(y)$, $y_{40}^{r2}(y)$ of the quantity $k(y)$

The basic idea of this algorithm consists in translating the lateral input coordinates $y_{40}^{r1}(y)$, $y_{40}^{r2}(y)$ of a certain quantity $k(y)$, evaluated through a minimization process of the RRD function error for each possible lateral wheelset displacement y. The lateral coordinates of the contact points in the auxiliary reference system can be then re-defined as:

$$y_{40}^{r1\,k} = y_{40}^{r1} + k \qquad\qquad y_{40}^{r2\,k} = y_{40}^{r2} + k \tag{8.12}$$

where the k value is bounded in the range $[-\bar{k}, +\bar{k}] = I_k$. Therefore the expression of the rolling radii error becomes a function of both y and k values:

$$E(y,k) = \cos\alpha_{40}(z_{20}^{r2}(y_{40}^{r2}+k) - z_{20}^{r1}(y_{40}^{r1}+k) - z_{40}^{r2}(y_{40}^{r2}) + z_{40}^{r1}(y_{40}^{r1})) \tag{8.13}$$

Eq. 8.13 is used as the objective function to find the optimal value k_{opt} of the translation quantity, which is then defined for each wheelset lateral displacement y as:

$$k_{opt}(y) = \underset{k\in I_k}{\operatorname{argmin}} \left|E(y,k)\right|. \tag{8.14}$$

Step - 3: Optimization process and re-definition of the resulting lateral coordinates of the contact points in the auxiliary reference system

The optimization process is performed by discretizing the I_k range with a resolution equal to 0.1 mm.

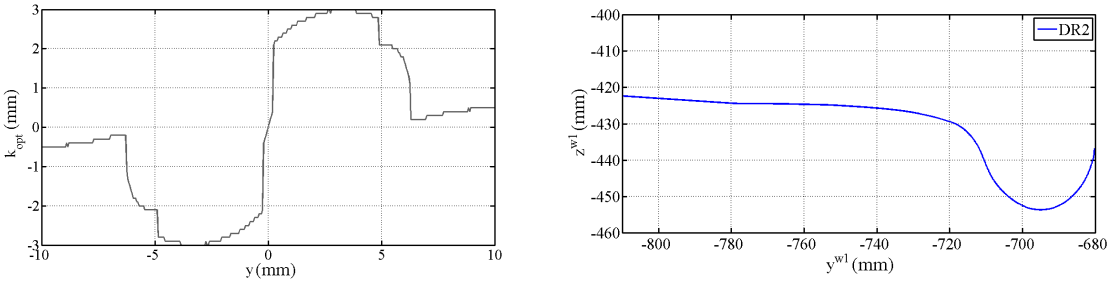

(a) (b)

Figure 8.5: DR2 wheel profile design (a): optimal value of the translation quantity k (b): DR2 wheel profile.

Fig. 8.5a illustrates the graphical representation of the k_{opt} value for a determined lateral displacement y. It should be noticed that the resulting values are small compared to the characteristic length of the problem. The resulting lateral coordinates of the contact points in the auxiliary reference system are evaluated as:

$$y_{opt}^{r1} = y_{40}^{r1} + k_{opt} \qquad\qquad y_{opt}^{r2} = y_{40}^{r2} + k_{opt}. \tag{8.15}$$

Step - 4: Computation of the outputs characterizing the optimized wheel profile

Through the introduction of the resulting coordinates into Eq. 8.6 and Eq. 8.5, the outputs $y_{20}^{w1}(y)$, $z_{20}^{w1}(y_{20}^{w1}(y))$, $y_{20}^{w2}(y)$, $z_{20}^{w2}(y_{20}^{w2}(y))$ of the optimized wheel profile - UIC 60 rail canted at 1/20rad matching are given by the following expressions:

$$\begin{pmatrix} y_{opt}^{r1}(y) \\ z_{20}^{r1}(y_{opt}^{r1}(y)) \end{pmatrix} = \begin{pmatrix} y \\ z_{40}(y) \end{pmatrix} + R(\alpha_{40}(y)) \begin{pmatrix} y_{20}^{w1}(y) \\ z_{20}^{w1}(y_{20}^{w1}(y)) \end{pmatrix} \tag{8.16}$$

$$\begin{pmatrix} y_{opt}^{r2}(y) \\ z_{20}^{r2}(y_{opt}^{r2}(y)) \end{pmatrix} = \begin{pmatrix} y \\ z_{40}(y) \end{pmatrix} + R(\alpha_{40}(y)) \begin{pmatrix} y_{20}^{w2}(y) \\ z_{20}^{w2}(y_{20}^{w2}(y)) \end{pmatrix}. \tag{8.17}$$

Step - 5: Holes fitting procedure

The optimized wheel profile, obtained after the holes fitting procedure and named DR2 wheel profile, is shown in Fig. 8.5b.

Step - 6: Evaluation of the new RRD function

The new RRD function is compared with the original one in Fig. 8.6; it shows that the two plots are almost coincident and that the error (see Fig. 8.7), which depends on the discretization precision of the range I_k, is about zero.

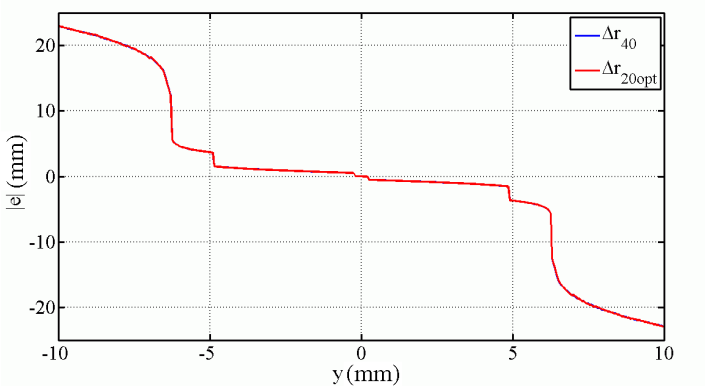

Figure 8.6: Rolling radii differences: $\Delta r_{20} = z_{20}^{w2}(y_{20}^{w2}(y)) - z_{20}^{w1}(y_{20}^{w1}(y))$ relative to the optimized matching DR2-UIC 60 canted at 1/20rad and $\Delta r_{40} = z_{40}^{w2}(y_{40}^{w2}(y)) - z_{40}^{w1}(y_{40}^{w1}(y))$ relative to the ORE S1002-UIC 60 rail canted at 1/40rad.

The design procedure adopted to define the DR2 discrete wheel profile may be affected by numerical errors coming from different sources such as:

- use of splines in the holes (where there is not a contact point distribution) and of fictitious points at the extremities of the wheel profile (parts of the ORE S1002 have been used);
- subsequent re-interpolations and smooth process of the wheel profile;
- since the DR2 wheel profile and UIC 60 rail canted at 1/20rad matching is based on the geometrical properties of the ORE S1002-UIC 60 canted at 1/40rad, it is characterized by the stiffness caused by the conformal contact typical of the

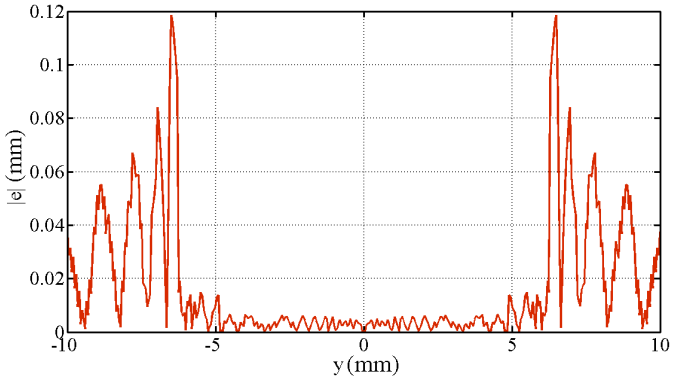

Figure 8.7: Absolute value of the error e in rolling radii difference distribution for the DR1-UIC 60 canted at $1/20\text{rad}$ matching.

original matching. In fact, as long as the contact becomes more conformal, contact points move more quickly along the contact surfaces even for small variations of the surfaces relative positions, leading to an increase in stiffness and ill-conditioning of the problem;

At the same time, one of the numerical advantage of the procedure consists in the fact that the new DR2 wheel profile is designed without any condition on the derivatives of the profiles; this aspect involves a reduction of the smoothing requirements and does not further increase the ill-conditioning characteristic of the design problem.

8.1.2 Comparison between the ORE S 1002 and the DR2 Wheel Profiles

This section deals with the comparison of the DR1 and DR2 characteristics with those relative to the standard ORE S1002 (optimized to match the UIC 60 rail canted at 1/40rad). Figs. 8.8-8.9 show the comparison between the resulting DR1 and DR2 wheel profiles and the original ORE S1002, while in Fig. 8.10 their relative differences along the vertical coordinates are plotted.

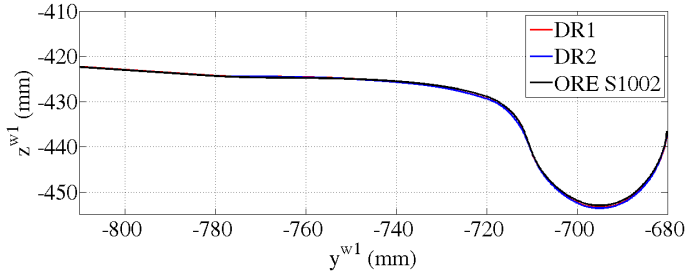

Figure 8.8: DR1, DR2 and ORE S1002 wheel profiles.

The derivatives of the resulting DR1 and DR2 wheel profile compared with the derivative of the standard ORE S1002 are illustrated in Fig. 8.11.

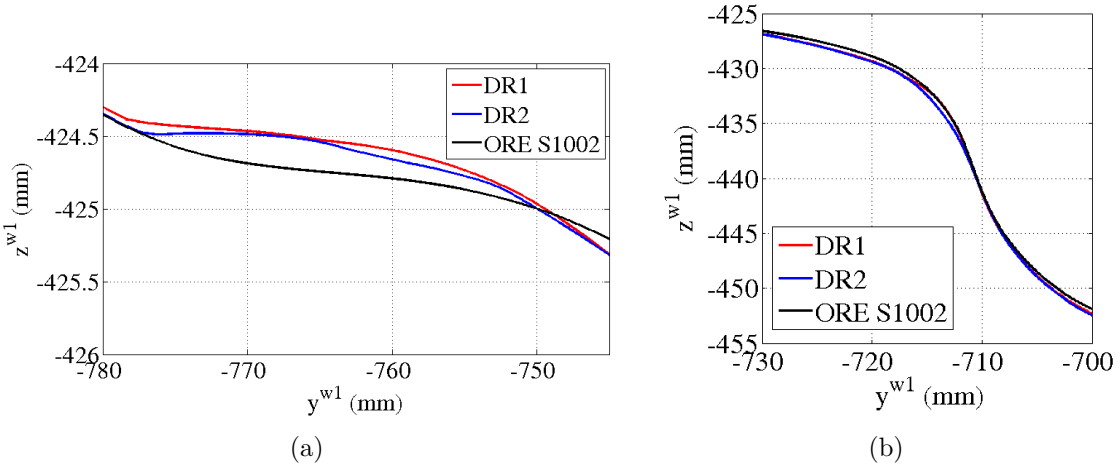

Figure 8.9: Comparison of the three wheel profiles. (a): tread zone (b): flange zone.

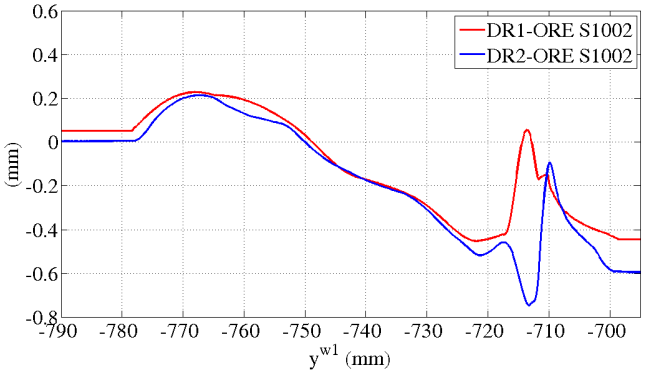

Figure 8.10: Vertical differences DR1-ORE S1002 and DR2-ORE S1002

The DR1 and DR2 wheel profiles are almost similar, representing that the DR2 optimization algorithm may improve the DR1 designing procedure which nevertheless, produces itself a wheel profile with good kinematic and wear characteristics. It can be noticed that the new DR1 and DR2-UIC 60 canted at 1/20rad matching try to reproduce the conformal contact characterizing the original matching ORE S1002-UIC 60 canted at 1/40rad with coherent vertical translations of the wheel profiles and derivatives in the tread and flange zone. More specifically the points of the new wheel profiles in the tread zone (Fig. 8.9a) are translated upwards with respect to those characterizing the original ORE S1002 wheel profile, while the points in the flange zone slope downwards (Fig. 8.9b).

8.1.3 Wear Analysis

The trainset to be investigated in order to evaluate the capability in wear reduction of the innovative profile is the passenger vehicle ALn 501 Minuetto, which is equipped with the standard ORE S1002 wheel profile and UIC 60 rail profile canted at 1/20rad

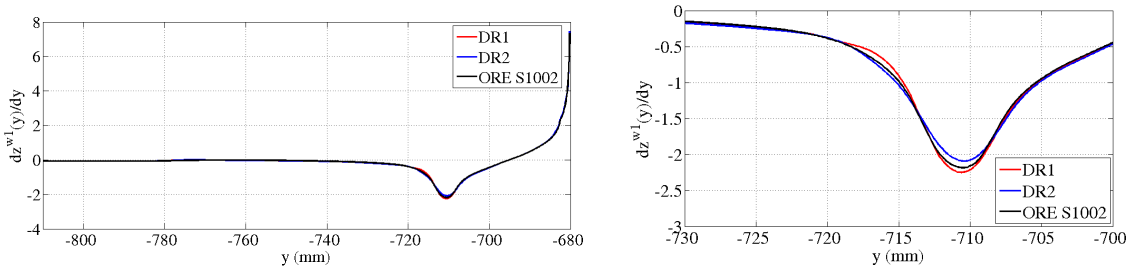

Figure 8.11: DR1, DR2 and ORE S1002 wheel profile derivatives.

in Italian railways. The dynamical simulations are performed on a virtual track that represents a statistical description of the mean Italian railway network traveled by the Minuetto vehicle; in Tab. 8.1 are summarized the track data provided by RFI and analyzed to obtain the statistical description according to the provisions described in chapter 6.

Table 8.1: Percentage of analysed data for the Minuetto vehicle.

District area	**Analysed distance** (km)	**Total distance** (km)	%
Florence	15576	37043	42.0
Turin	52220	78358	66.6
Naples	16740	32939	50.8
Verona	15182	22715	66.8
Total	85719	171055	50.1

The mean line presented in Tab. 8.2 has been extracted choosing a class number equal to $n_{class} = 8$; the resulting line is made up of $N_c = 27$ classes (the non-existent radius-superelevation are not listed for brevity). For each subtrack the mean radius R_c, the speed V_c, the superelevation h_c as well as the statistical weight p_k have been specified.

The focus of the optimization procedure is on the wheel profile evolution due to wear; for this purpose the rail profile of each N_c class of curve is supposed to be constant. The simplifying hypothesis of a constant rail profile (a UIC 60 rail profile for example) for all the tracks could be useful to overcome any conceptual difficulty in building a significant model of a railway net, but at the same time it can greatly reduce the validity of the results. In fact, the shape of the rails affects the position of the contact points both on rails and on wheels, the contact forces and, as consequence, the amount of wear and its distribution.

In this part of the research activity, the available data on the rail profiles provided by RFI have been exploited to select a series of rail profiles to be used as time-independent

Table 8.2: Mean Italian Minuetto virtual track.

$\mathbf{R}_{min}$ (m)	$\mathbf{R}_{max}$ (m)	**Superelevation** $h_{min} - h_{max}$ (mm)	$\mathbf{R}_c$ (m)	$\mathbf{H}_c$ (mm)	$\mathbf{V}_c$ (km/h)	$\mathbf{p}_k$ %
250	285	80–99	**263**	90	65	1.90
		140–160		156	75	4.21
285	331	80–99	**307**	92	70	1.11
		140–160		154	80	1.62
331	394	100–119	**358**	106	70	0.44
		120–139		135	80	1.24
394	488	40–59	**438**	50	70	0.80
		120–139		126	80	0.33
		140–160		150	90	4.17
488	640	80–99	**557**	82	70	1.44
		100–119		105	80	4.72
		120–139		130	90	1.29
640	930	0–19	**769**	10	70	0.23
		60–79		75	80	3.08
		80–99		90	90	3.78
		120–139		131	115	0.78
		140–160		150	110	1.46
930	1702	0–19	**1239**	12	70	1.27
		20–39		30	85	1.91
		40–59		48	85	2.41
		80–99		90	130	2.67
		100–119		114	130	2.16
		120–139		132	130	1.10
1702	10000	0–19	**4202**	5	70	1.08
		20–39		22	120	1.21
		40–59		50	130	0.25
10000	∞				130	52.34

profiles in the multibody simulations. According to the working hypothesis based on the collected data that in small radius curves it is easier to find a deeply worn rail profile than in straight tracks or in large radius curves, a pair of representative rail profiles, in a statistical sense, has been chosen for each radius curve range. In detail, the population of the possible curve radius has been divided in 8 classes, coincident with the radius classes of the mean line; for each rail class a left and right rail profile have been assigned. The choice of these profiles has been made by analyzing the data concerning rails in different regions of Italy (Tuscany, Latium, Veneto, Trentino-Alto Adige and Sicily) and by calculating the average rail wear at 45 degrees. Among the external rails, the profile with the minor deviation with respect to this average wear was selected as the representative external rail profile of the class, while the associated profile on the other side of the track was selected for the internal side of the track.

The rail profiles acquired by means of an optical instrumentation are shown in

Fig. 8.12(a) (the external rails) and Fig. 8.12(b) (the internal ones). The worn rail data included a certain amount of numerical noise and they had to be treated in order to smooth the profiles and their derivatives. To this end, the data were filtered with a sliding mean filter and then the rails profile have been rebuilt through several sections of cubic splines. Finally, these pairs of rail profiles have been associated to each class of the virtual track depending on the radius curve.

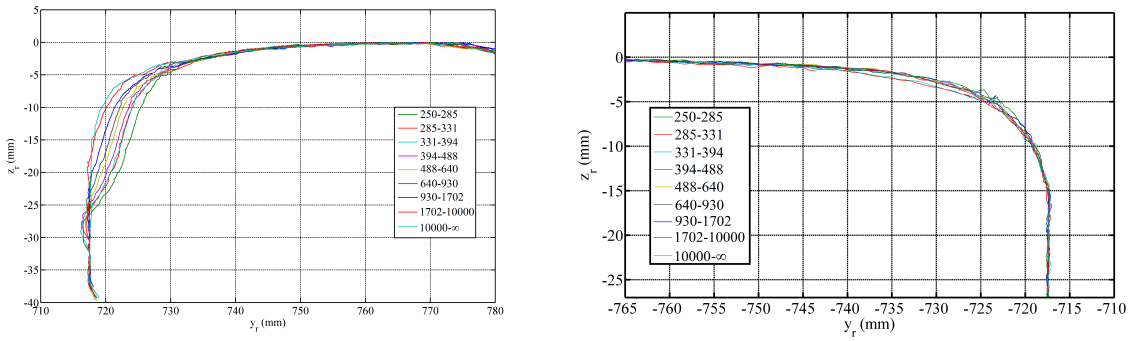

(a) (b)

Figure 8.12: Worn rail profile of each class (cant of 1/20rad) (a): external (b): internal.

Wear Parameters Evolution

In this section the results of the dynamic simulations aimed at a wear evaluation will be presented in order to compare the profiles considered in this study: the standard ORE S1002 and the DR2 wheel profiles. The simulation campaign has been performed considering the compared wheel profiles running on the same rail inclination 1/20rad. Concerning the resistance to wear, the performance can be assessed by analyzing the evolution of three reference dimensions introduced in the previous section 5.2.

To this end, Fig. 8.13 shows the progress of the QR dimension for each profile: as it can be seen, the progress of DR2 profile is slower than that of the ORE S1002. In fact, assuming a comparison limit equal to 7mm, which is slightly above than the acceptable threshold value of 6.5mm prescribed by the standard [12], the trend of the DR2 shows that the comparison limit is reached with an increase in the covered distance by at least 30 %.

With regard to the progress of the flange thickness FT depicted in Fig. 8.14, the minimum value equal to 22mm [12] is reached after covering about 80000km when the ORE S1002 profile is adopted on the Minuetto vehicle; differently, with the new profiles the total covered distance can be extend up to 100000km and above (see Tab. 8.3). Regarding the flange height FH, the comparison is depicted in Fig. 8.15: this quota usually increases owing to the wear on the tread of the profile. However, in the

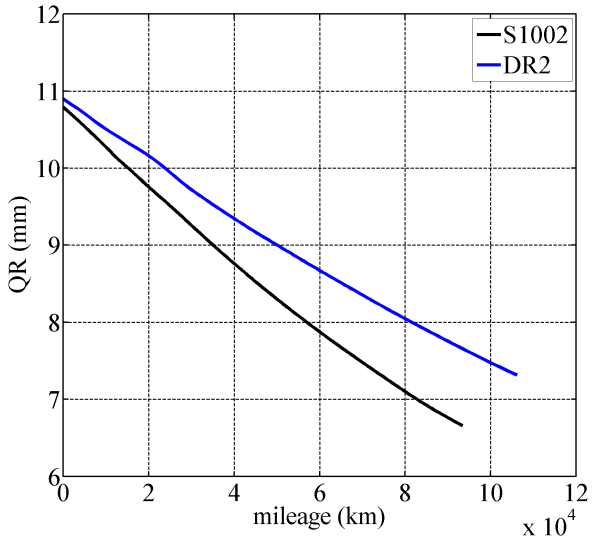

Figure 8.13: Progress of the QR dimension: comparison of the wheel profiles.

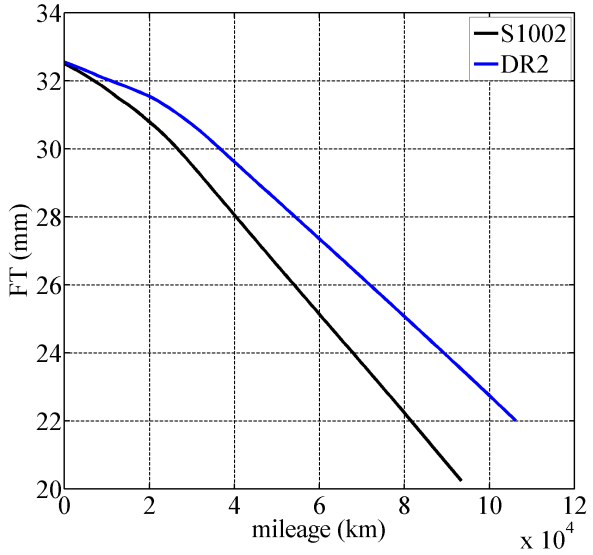

Figure 8.14: Progress of the FT dimension: comparison of the wheel profiles.

case of study the wear is specially localized on the wheel flange and the consequently slight increase of the flange height is not critical regarding the wear evolution progress. Obviously it is not true when the tread wear is dominating: to this aim other experimental tests are being performed to obtain data also for tread wear progress (to get these data more time and kilometers are needed). The progress of the quotas shows also a relocation of the material towards the tread zone.

With respect to the evolution of the wheel shape, the comparison between the initial and the final condition for the ORE S1002 and DR2 profiles is presented in the Figs. 8.16 and 8.17. The variation in wheel profile is numerically described by means of about one hundred procedure steps and besides the unworn and the final profile, all the intermediate wheel geometries have also been plotted in the relative figure. Since

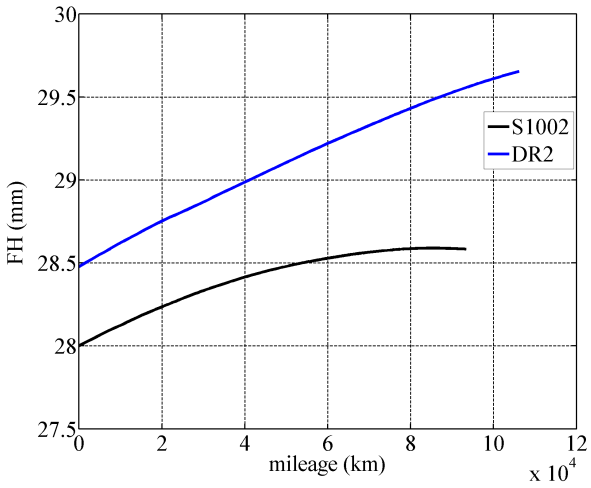

Figure 8.15: Progress of the FH dimension: comparison of the wheel profiles.

Table 8.3: Total mileage traveled up to achievement the re-profiling condition $FT = 22\text{mm}$.

Wheel profile	km_{tot}(km)	*Increase of wheel wear performance (%)*
ORE S1002	81400	-
DR2	106100	30.3

the Italian mean line of the Minuetto vehicle comprises a relevant percentage of sharp curves, the wear is mainly located on the flange instead of the tread. The DR2 wheel shape evolution shows a transfer of the worn material towards the tread zone respect to the standard ORE S1002 shape evolution; it indicates a better distribution of the worn material that leads to an increase of the wheel profile lifetime.

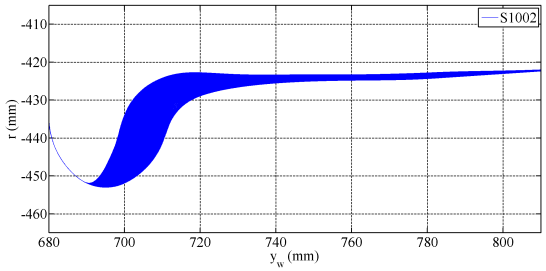

Figure 8.16: Evolution of the S1002 wheel profile due to wear.

8.1.4 Stability Assessment

Besides the resistance to wear, the performance of the new DR2 profile has been also investigated from a running stability point of view in order to assess the critical speed of the vehicle, that is the minimum speed at which instability occurs by way of *hunting*. The meaning of stability can be explained easily with the wheelset motion;

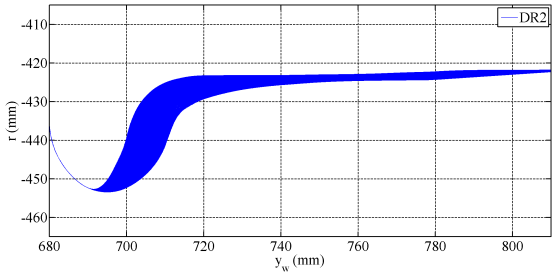

Figure 8.17: Evolution of the DR2 wheel profile due to wear.

stability means that for a slight lateral displacement or yaw angle the wheelset moves back into its central position with a damped oscillatory parasitic motion. The wheelset motion is considered to be unstable if for some small irregularities an excited vibration takes place, so that the maximum amplitudes increase and the parasitic motion is finally only restricted by flange contact.

For a railway vehicle equipped with wheelsets instead of independent rotating wheels, a critical speed always exists and hence the maximum speed in service must be enough lower than this threshold.

It is also well-known that, besides the influence on wheel and rail wear, the characteristics of the wheel-rail interaction strongly affect both the guidance and the stability of a railway vehicle. More precisely, the influence of the wheel profile (or even better of the wheel-rail pair) lies in the rolling radius difference function: in fact, the progress of its first derivative is the local conicity of the wheel-rail pair and both the performance in negotiating the curves and the frequency of the wheelset kinematic oscillation depend on this conicity function. Leaving out the guidance which is not discussed in detail in this activity, for what regards the stability at high speeds, the most simple evidence of this phenomenon can be found in the Klingel's linear model of a wheelset on straight track [14][20].

Nevertheless, being the physical problem nonlinear, not only for the characteristics of the wheel-rail coupling, but also for the structure of the vehicle (for example the non linear suspension characteristics), the better way to check the stability condition is a nonlinear approach by means of dynamic simulations. Among the most common methods used in investigating the critical speed via numerical simulation of the vehicle motion [11], a criterion based on the wheelset lateral displacement has been chosen in this work.

The procedure consists in simulating the initially perturbed motion of the vehicle on straight track at variable speed and checking the amplitude of the wheelset lateral displacement: the vehicle can be considered stable at a certain speed if the lateral displacement of all its wheelsets is almost zero or anyway negligible if compared with the

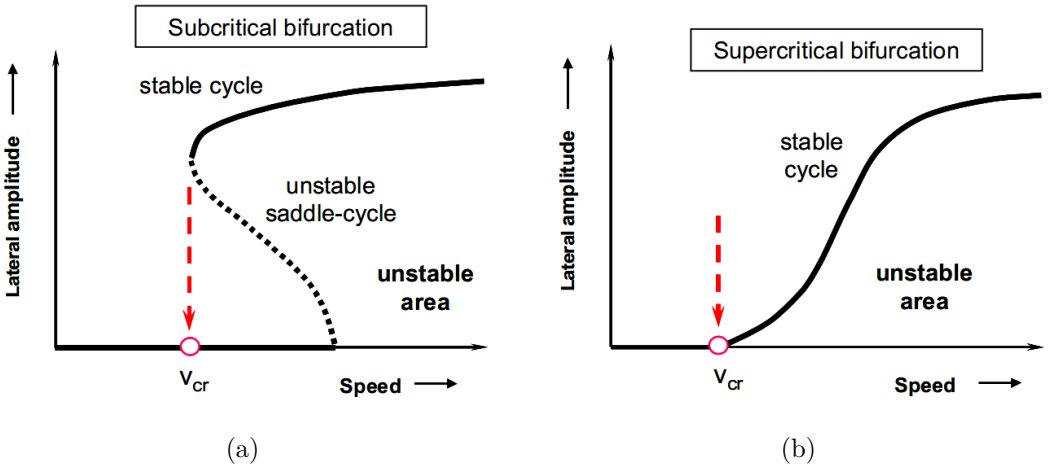

Figure 8.18: Examples of bifurcation diagrams arising from stability tests [20][33].

flangeway clearance. In more detail, the result in this kind of test is a bifurcation diagram of the displacement amplitude as a function of the traveling speed; the two typical forms of the response are depicted in Fig. 8.18, although more complicated situations may occur. Basically, in the supercritical case the amplitude increases continuously as the speed is augmented; on the contrary, when the bifurcation is subcritical, there is a speed range within which multiple solutions are possible depending on the amplitude of the excitation.

In order to find the real critical speed V_{cr}, the test should be carried out by reducing the traveling speed instead of increase it, starting from an unstable running condition characterized by flange contact. The speed at which the lateral oscillation of the most critical wheelset vanishes or begin to reduce notably can be considered as the critical speed of the vehicle.

With regard to the present work, the stability assessment have been performed taking into account both the unworn and the worn geometries of the two wheel profiles. In particular, the wheel shapes corresponding to a covered distance equal to 80000km, being this latter the kilometrage at which the first limit value among the wear control parameters is reached by the S1002 profile (see section 8.1.3), have also been chosen as fully worn profiles.

The progresses of the lateral displacement of the most critical wheelset and the speed for each unworn wheel profile are reported in Figs. 8.19, and 8.20. In order to excite the lateral motion of the wheelsets and the flange contact, through a single smoothed irregularity the track is suddenly displaced laterally of 5mm before the reduction in speed takes place. In regarding to the friction coefficient at the wheel-rail contact, a value equal to 0.4 has been chosen to draw conservative conclusions.

While the S1002 can be considered stable only for speed less than 155km, the new

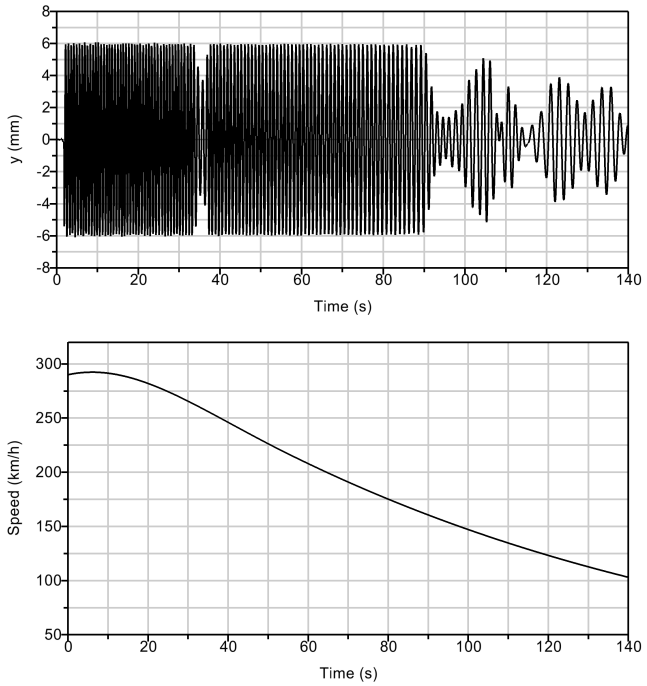

Figure 8.19: Stability test of the unworn S1002 profile: lateral displacement of the 7^{th} wheelset and speed profile.

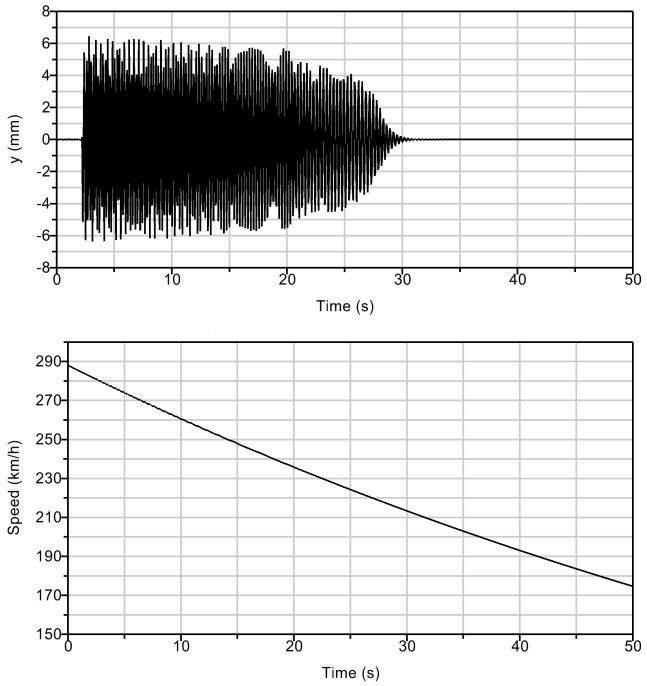

Figure 8.20: Stability test of the unworn DR2 profile: lateral displacement of the 7^{th} wheelset and speed profile.

profile has a critical speed approximately equal to 240km/h, which is considerably higher than the maximum service speed of the Minuetto, equal to 130km.

The results of the stability test when the worn profiles are applied to the Minuetto

are shown in Figs. 8.21 and 8.22. The critical speed are notably lower than the previous ones and the reduction in the oscillation amplitude convergence is slower.

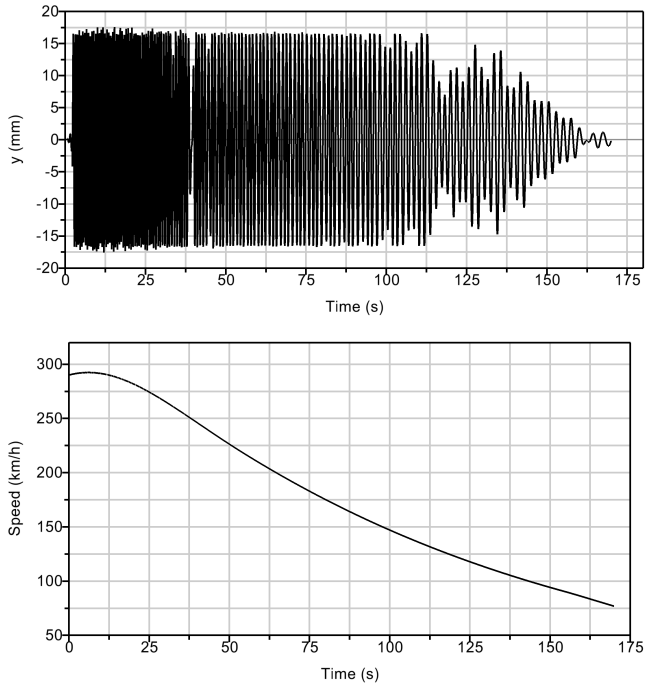

Figure 8.21: Stability test of the worn S1002 profile: lateral displacement of the 7^{th} wheelset.

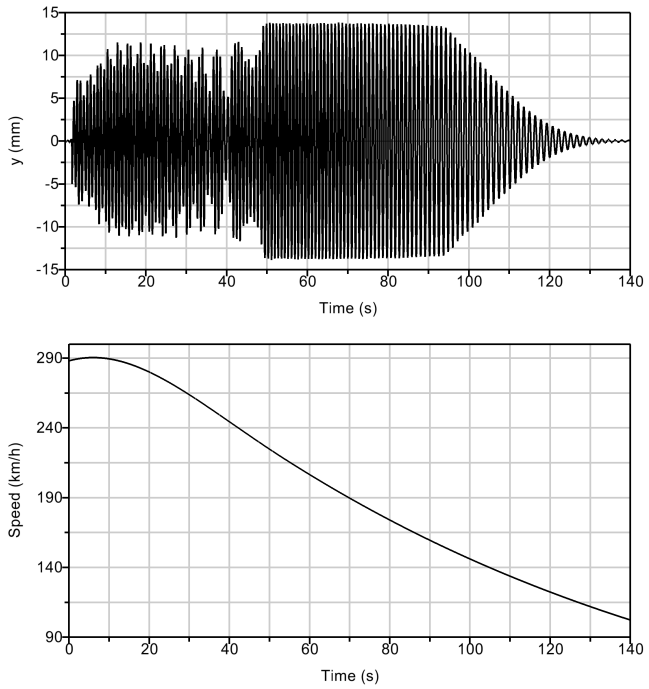

Figure 8.22: Stability test of the worn DR2 profile: lateral displacement of the 7^{th} wheelset.

The results of the stability assessment are summarized in Tab. 8.4: in the investigated cases, the critical speeds arising from the employment of the innovative profile

Table 8.4: Summary of the critical speeds (km/h) of the Minuetto: comparison of the ORE S 1002 and DR2 wheel profiles.

Wheel profile		Critical speed (km/h)
S1002	new	155
	worn	135
DR2	new	240
	worn	160

is greater than the maximum service speed of the vehicle.

Experimental evaluations of the wear on the Minuetto equipped with the DR2 wheel profile by means of experimental tests have been scheduled by Trenitalia, in order to verify the response in terms of progress of the reference dimensions so as to focus on a future approval of the proposed new wheel profile.

8.2 Prediction of Wheel Re-profiling Intervals

Suitable wear models can be used as powerful tool in the railway vehicle design to predict the wheel re-profiling intervals; in this way possible critical situations connected with either the bogie suspension characteristics of the vehicle or the specific wheel rail matching can be investigated and improving solutions can be researched directly during the design phase with several cost saving.

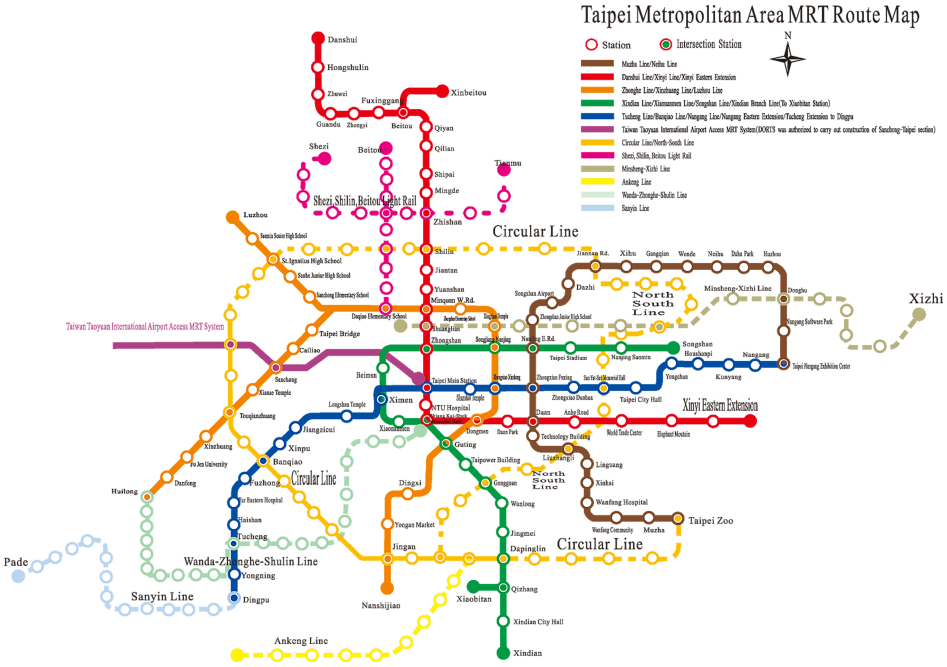

Figure 8.23: Taipei metropolitan layout.

The wheel wear evolution prediction has been carried out in collaboration with

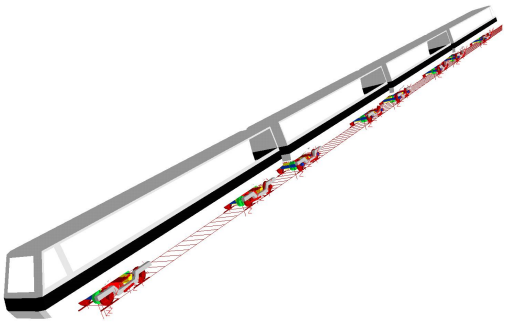

Figure 8.24: MLA Taipei: multibody model.

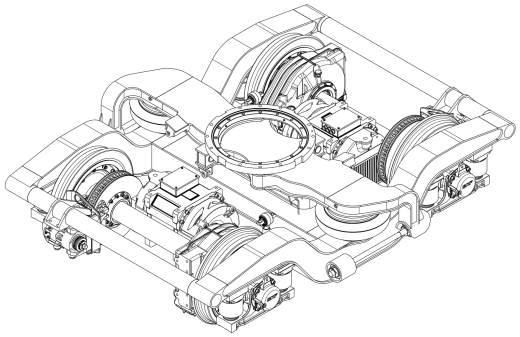

Figure 8.25: MLA Taipei: motor bogie.

AnsaldoBreda S.p.A. that was very interested to study the Taipei subway scenario from the wear standpoint. The Italian company is responsible for the construction of the MLA Taipei metro vehicles (MLA is the fully automated platform developed by AnsaldoBreda and Ansaldo STS with technology driverless) running on the new Taipei Metro Circular Line (Phase I) starting from December 2015 (see Fig. 8.23) [8].

8.2.1 Metro Taipei Scenario

In Fig. 8.24 the multibody model of the MLA Metro Taipei is showed; it is composed by four coaches with two motor bogies for each of these (see Fig. 8.25) and the general data of the Taipei Metro Circular Line scenario is presented in Tab. 8.5.

Table 8.5: Taipei Metro Circular Line: general data.

Maximum speed in service	90 $\mathrm{km\,h^{-1}}$
Maximum vehicle capacity	700 passengers
Wheel profile	ORE S 1002
Wheel diameter	710 mm
Minimum curve radius	45 m
Rail gauge	1435 mm
Rail cant α_p	1/40
Rail profile	UIC 60

Wear phenomena plays a critical role in metropolitan field because of the very small curve radii typical of the subway networks. To perform the dynamical simulations some characteristics curves have been extracted from the Taipei Circular Line (whose total length is equal about to 15km) using the statistical approach described in previous sections. The statistical analysis has been built focusing on the very sharp curves typical of the considered network; to this aim different numbers for the radii class $n^R_{class} = 8$ and the superelevation subclass $n^h_{class} = 2$ have been chosen and the resulting classification made up of $N_c = 11$ tracks is shown in Tab. 8.6.

Table 8.6: Data of the curvilinear tracks statistically equivalent to Taipei Circular Line.

$\mathbf{R}_{min}$ (m)	$\mathbf{R}_{max}$ (m)	**Superelevation** $h_{min} - h_{max}$ (mm)	$\mathbf{R}_c$ (m)	$\mathbf{H}_c$ (mm)	$\mathbf{V}_c$ (km/h)	$\mathbf{p}_k$ %
45	51	0 - 65	**45**	46	25	1.61
60	72	0 - 65	**65**	56	32	0.28
90	120	0 - 65	**102**	30	36	0.37
		65 - 130		85	43	1.53
120	179	0 - 65	**134**	55	45	0.77
		65 - 130		79	48	1.80
179	354	0 - 65	**246**	43	59	1.31
		65 - 130		104	69	5.42
354	20000	0 - 65	**2570**	29	90	12.93
		65 - 130		92	90	2.01
20000	∞	0	∞	0	90	71.97

According to the AnsaldoBreda the average wheel profile evolution is investigated and based on the European standard provision [12] the limit for the vehicle wheels re-profiling is reached when the flange thickness FT is equal to 27.5mm; in Figs. 8.26-8.29 the wheel profile evolution due to wear (imposing wheel discrete step threshold $D^w_{step} = 0.4$mm) and the reference quotas FH, FT and QR progresses considering dry contact condition (friction coefficient equal to $\mu = 0.3$) are shown. The FT progress (Fig. 8.27) highlights a total mileage traveled by the vehicle until $FT = 27.5$mm equal to $km_{tot} = 140470$km. The mileage traveled by the MLA Taipei vehicle to reach a re-profiling interval is bigger than the RAMS (Reliability Availability Maintainability Safety) provisions required by the Department of Rapid Transit Systems of Taipei City Government in the terms of business contract: in fact, the RAMS requirement related to the wheel re-profiling interval is $km_{RAMS} = 120000$km and therefore the MLA Taipei vehicle design satisfies the customer wear provisions.

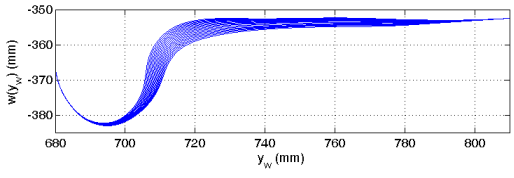

Figure 8.26: MLA Taipei: wheel profile evolution.

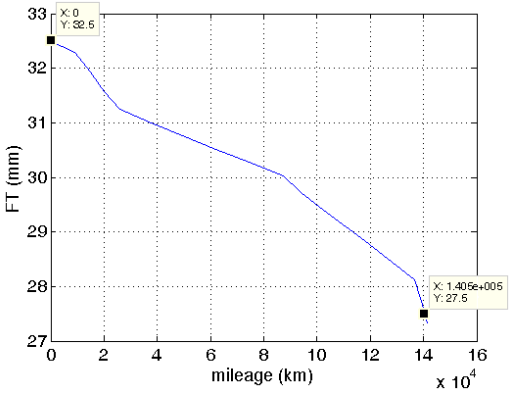

Figure 8.27: MLA Taipei: FT quota progress.

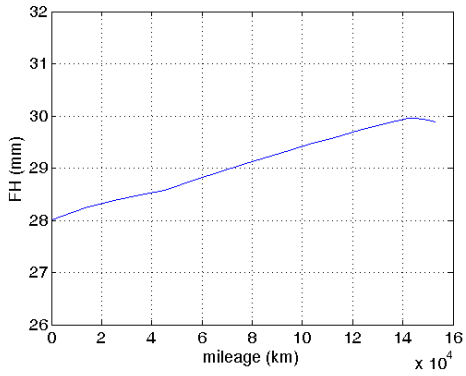

Figure 8.28: MLA Taipei: FH quota progress.

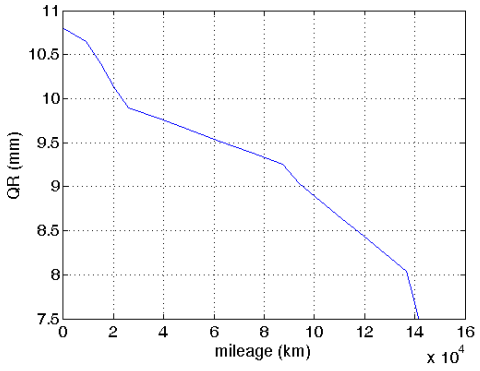

Figure 8.29: MLA Taipei: QR quota progress.

However the lubrication contact condition has been implemented in the proposed wear model to further investigate the wear phenomena. In particular the friction coefficient has been modified in the small radius curves to simulate the presence of any rail greasers on the Taipei Circular Line network. For example in the following Figs. 8.30-8.33 are presented the results imposing a frictional coefficient equal to $\mu = 0.1$ (typical value for the grease contact condition [7][9]) for the curves with radii $R < 120$m, corresponding to the top four curves of the statistical analysis (see Tab. 8.6); the other curve classes maintain dry contact conditions with a friction coefficient equal to $\mu = 0.3$.

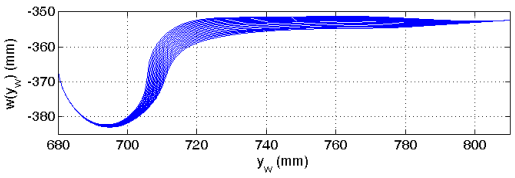

Figure 8.30: MLA Taipei with lubricated rails: wheel profile evolution.

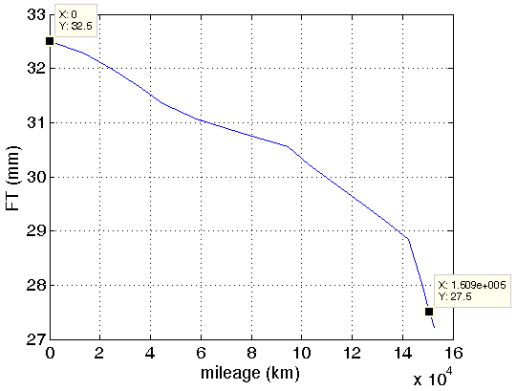

Figure 8.31: MLA Taipei with lubricated rails: FT quota progress.

In Tab. 8.7 are summarized the wheel re-profiling intervals for the two considered cases: the lubrication of the rails in the $R < 120$m curves, corresponding to the 3.8% of the Taipei Circular Line total length leads to an increase of the wheelset's lifetime of about ten thousand kilometers. As can be seen by the comparison between Fig. 8.26 and Fig. 8.30 the lubrication contact in the smaller radius curves causes a better distribution of the removed material with a shift towards the wheel tread (highligthed also by the increase of the flange height (see Figs 8.28, 8.32)).

At the same time the Figs. 8.34-8.36 show the rail wear evolution with dry contact

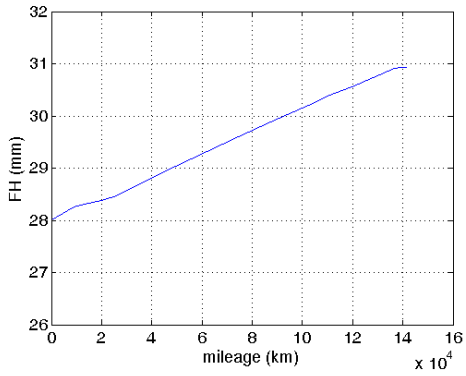

Figure 8.32: MLA Taipei with lubricated rails: FH quota progress.

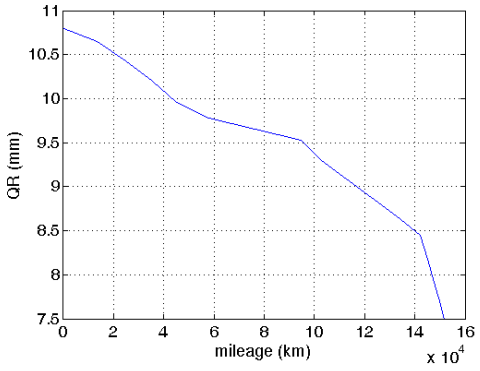

Figure 8.33: MLA Taipei with lubricated rails: QR quota progress.

Table 8.7: Total mileage traveled up to achievement the re-profiling condition $FT = 27.5\text{mm}$.

Scenario contact condition	*Lubricated track (%)*	km_{tot}(km)	*Increase of wheel wear performance (%)*
Dry contact condition	-	140470	-
$R < 120$m curves lubricated	3.8	150900	7.4

and lubricated contact condition for $R < 120$m curves. The rail wear is studied starting from the new UIC 60 rail (the Taipei circular Line opening is scheduled for December 2015) considering $n_{sr} = 5$ rail discrete step with rail threshold equal to $D^r_{step} = 0.8$mm. In Tab. 8.8 can be seen the considerable improvement of rail wear performance using lubricated rails with about further 47% of vehicle burden on the track to reach the same rail wear of the dry contact scenario.

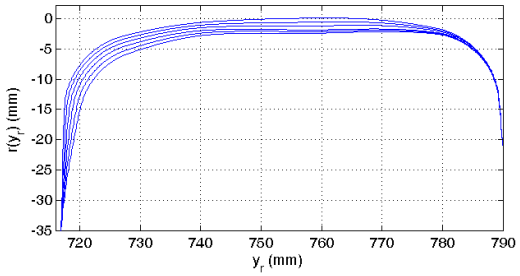

Figure 8.34: MLA Taipei: rail profile evolution.

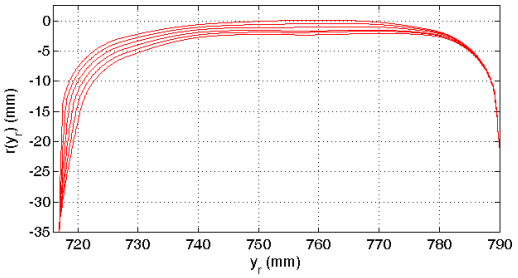

Figure 8.35: MLA Taipei with lubricated rails: rail profile evolution.

Table 8.8: Total vehicle number burden on the track.

Scenario contact condition	*Lubricated track (%)*	N_{tot}	*Increase of rail wear performance (%)*
Dry contact condition	-	1869750	-
$R < 120$m curves lubricated	3.8	2748375	47.0

The increase of wheelsets and rails lifetime represent a focus point in the Taipei metropolitan area that carries almost 2 thousands of users per day [8]. With simple

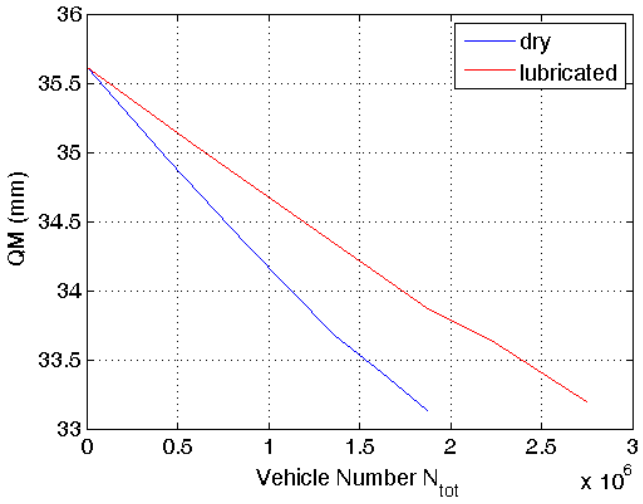

Figure 8.36: MLA Taipei: QM progress.

considerations related to the metropolitan lines numbers and the frequency of the vehicle traveling on the networks is possible estimate the management and maintenance cost due to both wheelsets re-profiling operations [4] (and consequently the corresponding vehicle not traveling on the line) and rail grinding [38] (and consequently the stop of the corresponding line) (see Tab. 8.9). Finally the proposed example clarify the importance of the wear model in vehicle design optimization.

Table 8.9: Estimation of wear maintenance costs.

Component	*Cost item*	*estimated quantity*
Rail	Rail grinding	5000 €/km
	Rail renewal	100000 €/km
	Network stopped	150000 $people/day$
Wheelset	Wheelset turning	400 €
	Wheelset renewal	3000 €
	Vehicle stopped	18000 $people/day$

Chapter 9

Conclusion

A complete model for the wheel and rail wear prediction in railway applications has been presented in this Ph.D. thesis. Such model was specifically developed for complex railway networks, where the exhaustive analysis on the complete line is not feasible because of the computational load required.

The whole model is made up of two mutually interactive parts. The former evaluates the vehicle dynamics and comprises both the multibody model of the vehicle and a global wheel-rail contact model for the calculation of the contact points and of the contact forces. The latter is the wear model which evaluates the amount of material to be removed due to wear starting from the outputs of the multibody simulations. The interaction between the two parts is not a continuous time process but occurs at discrete steps; consequently the evolution of the wheel and rail geometry is described through several intermediate profiles.

The main innovative aspects of the model are related to the track statistical approach to study complex railway networks based on the replacement of the complete railway line with a statistically equivalent set of representative curved tracks classified by radius, superelevation and traveling speed. Moreover the use of innovative global contact models in wear model designed to study complex railway networks, assure both an increase of the model accuracy and an important reduction of the computational time making possible the online implementation within the commercial multi-body software without discrete approximated look-up tables. Finally the simultaneous rail and wheel wear evolution has been investigated through a suitable simulation strategy properly developed and implemented to consider the different time scales characterizing the wheel and rail wear behavior: the wheel wear has been studied basing on the distance traveled by vehicle, while the rail wear has been evaluated basing on the total tonnage burden on the railway track.

The whole model has been validated on a critical scenario in terms of wear in Italian

railways: the Alstom DMU Aln 501 Minuetto circulating on on the Aosta-Pre Saint Didier railway line. This choice has permitted to have significant results from the wear viewpoint in a relatively few mileage traveled by the vehicle. In this way manageable experimental campaigns characterized by reasonable measurement times could have been carried out. Particularly, the new model results have been compared with both the complete railway network ones and the experimental data provided by Trenitalia. If the track discretization is accurate enough, the developed model turned out to be quite in agreement with the experimental data, the complete railway network model and the evolution of all the profile characteristic dimensions, describing in a satisfying way the wear progress both on the wheel and on the rail. Therefore, as regard to the track description, the statistical analysis represents a good approach with a significant saving of computational time despite a very slight loss of the result accuracy if compared to the complete railway network approach.

As further validation and to better investigate the performance and usability of the innovative model a comparison with the wear evaluation procedure implemented within the Simpack multibody commercial software has been carried out. The scenario composed by a vehicle composition widely used in Italian railways (E.464 locomotive and Vivalto coach) running on a virtual statistical representative mean Italian railway network has been considered for the comparison study. The results obtained highlight how the innovative model reflects the real behavior of the wear phenomena (for example an higher removed material for the leading wheel and for the sharp curves and a wear rate decrease when the contact conditions reach the conformal contact). Furthermore the proposed model highlights better performance in terms of computational efficiency with a considerable time reduction if compared to the Simpack model, because of the high numerical efficiency of the global contact model.

The wear model has been used for the wear assessment of a new wheel profile shape developed in collaboration with Trenitalia and RFI, to improve the poor performance with regard to the resistance to wear and the guidance in sharp curves that the S1002 wheel profile exhibits when matched to the UIC 60 rail profile canted at 1/20rad. The innovative wheel profile realized for the UIC 60 rail with a laying angle of 1/20rad has proven to work fine as for the resistance to wear if compared with the S1002 wheel profile. In addition, the kinematic characteristics of the innovative wheel-rail coupling is appreciably better than those of the S1002. A stability assessment has also been performed to check the critical speed of the Aln 501 Minuetto vehicle equipped with the new wheel profile both in the unworn and worn condition.

The proposed model has been employed in collaboration with AnsaldoBreda S.p.A. to predict wheel re-profiling intervals and to investigate and improve the considered wheel-rail matching wear behavior directly during the vehicle design phase with several

cost saving.

Future developments will be based on further validation relative to other railway tracks with an higher mileage than the Aosta-Pre Saint Didier line and to a combination of vehicles traveling on the tracks. The experimental campaigns scheduled by Trenitalia and RFI will take into account advanced wear on the wheel (especially on the wheel tread) and on the rail considering both the head rate and the gauge corner rail evolution and also the wear of the complete wheel and rail profiles. Moreover the new data will make it possible the study of different environmental conditions (i.e. wet and lubricated contact). Also further physical phenomena like the rolling contact fatigue (RCF) and the plastic wear will be considered and implemented in the developed wear model.

Bibliography

[1] J-F. Antoine, C. Visa, et al. “Approximate Analytical Model for Hertzian Elliptical Contact Problems”. In: ***Journal of Tribology*** 128 (2006), pp. 660–664.

[2] A.M.S. Asih, K. Ding, and A. Kapoor. “Modelling rail wear transition and mechanism due to frictional heating”. In: ***Wear*** 284-285 (2012), pp. 82–90.

[3] J. Auciello, E. Meli, et al. “Dynamic simulation of railway vehicles: wheel/rail contact analysis”. In: ***Vehicle System Dynamics*** 47 (2009), pp. 867–899.

[4] A. Bevan, P.M. Berry, et al. “Optimisation of wheelset maintenance using whole-system cost modelling”. In: ***Journal of Rail and Rapid Transit*** 227 (2013), issue 6,594–608.

[5] F. Braghin, R. Lewis, et al. “A mathematical model to predict railway wheel profile evolution due to wear”. In: ***Wear*** 261 (2006), pp. 1253–1264.

[6] I.Y. Shevtsov C. Esveld V.L. Markine. “Shape optimisation of a railway wheel profile”. In: ***European Railway Review*** 12(2) (2006), pp. 81–86.

[7] P. Clayton. “Tribological aspects of wheel-rail contact a review of recent experimental research”. In: ***Wear*** 191 (1996), pp. 170–183.

[8] *Department of Rapid Transit Systems, Taipei City Government.* URL: `http://english.dorts.taipei.gov.tw/`.

[9] L. Deters and M. Proksch. “Friction and wear testing of rail and wheel material”. In: ***Wear*** 258 (2005), pp. 981–991.

[10] R. Caldwell E. Magel J. Kalousek. “A numerical simulation of wheel wear”. In: ***Wear*** 258 (2004), pp. 1245–1254.

[11] *EN 14363: Railway applications — Testing for the acceptance of running characteristics of railway vehicles — Testing of running behaviour and stationary tests.* 2005.

[12] *EN 15313: Railway applications — In-service wheelset operation requirements — In-service and off-vehicle wheelset maintenance*. 2010.

[13] R. Enblom and M. Berg. "Simulation of railway wheel profile development due to wear influence of disc braking and contact environment". In: ***Wear*** 258 (2005), pp. 1055–1063.

[14] C. Esveld. *Modern Railway Track*. Delft, Netherland, 2001: Delft University of Technology, 1985.

[15] E. Funaioli, A. Maggiore, and U. Meneghetti. *Lezioni di Meccanica Applicata alle Macchine*. Cambridge, UK: Pàtron Editore, 2005.

[16] C. Hardwick, Roger Lewis, and D.T. Eadie. "Wheel and Rail Wear - Understanding the Effect of Third Body Materials". In: *CM2012 9th International Conference on Contact Mechanics and Wear of Rail/Wheel Systems*. Chengdu, China, 2012.

[17] H. Hertz. "The Contact of Elastic Solids". In: ***J. Reine Angew. Math.*** 92 (1881), pp. 156–171.

[18] S. Iwnicki I. Persson. "Optimisation of railway wheel profiles using a genetic algorithm". In: *18th Int. Association for Vehicle System Dynamics. Symposium*. Kanagawa, Japan, 2003.

[19] S. Iwnicki. "Simulation of wheel - rail contact forces". In: ***Fatigue and Fracture of Engineering Materials and Structures*** 26 (2003), pp. 887–900.

[20] S. Iwnicki. *The Manchester Benchmarks for Rail Vehicle Simulators*. Lisse, Netherland, 1999: Swets and Zeitlinger, 2008.

[21] T. Jendel and M. Berg. "Prediction of wheel profile wear". In: ***Suppl. Vehicle System Dynamics*** 37 (2002), pp. 502–513.

[22] K. Johnson. *Contact Mechanics*. Cambridge, UK: Cambrige University Press, 1985.

[23] J. J. Kalker. "A fast algorithm for the simplified theory of rolling contact". In: ***Vehicle System Dynamics*** 11 (1982), pp. 1–13.

[24] J. J. Kalker. "Survey of wheel-rail rolling contact theory". In: ***Vehicle System Dynamics*** 8 (1979), pp. 317–358.

[25] J. J. Kalker. *Three-dimensional Elastic Bodies in Rolling Contact*. Dordrecht, Netherlands: Kluwer Academic Publishers, 1990.

[26] H. Krause and G. Poll. "Verschleiβbei gleitender und wälzender Relativbewegung". In: ***Tribologie und Schmierungstechnik*** 31 (1984), issue 4/5, 209–214/285–289.

[27] E. Meli, S. Falomi, et al. “Determination of wheel - rail contact points with semianalytic methods”. In: ***Multibody System Dynamics*** 20 (2008), pp. 327–358.

[28] E. Meli, S. Magheri, and M. Malvezzi. “Development and implementation of a differential elastic wheel?rail contact model for multibody applications”. In: ***Vehicle System Dynamics*** 49:6 (2011), pp. 969–1001.

[29] E. Meli, S. Magheri, et al. “An innovative wheel-rail contact model for multibody applications”. In: ***Wear*** 271 (2011), pp. 462–471.

[30] *Multi-Body Simulation SIMPACK MBS Software*. 2012. URL: `http://www.simpack.com/`.

[31] S. Zakharov et ot. “Problems with wheel and rail profiles selection and optimization”. In: ***Wear*** 265 (2008), pp. 1266–1272.

[32] T. G. Pearce and N. D. Sherratt. “Prediction of wheel profile wear”. In: ***Wear*** 144 (1991), pp. 343–351.

[33] O. Polach. “Influence of wheel/rail contact geometry on the behaviour of a railway vehicle at stability limit”. In: ENOC-2005, Eindhoven University of Technology, 7-12 August. The Netherlands, 2005, pp. 2203–2210.

[34] O. Polach. “Wheel profile design for target conicity and wide tread wear spreading”. In: ***Wear*** 271 (2011), pp. 195–202.

[35] J. Pombo, J. Ambrosio, and ot. “A study on wear evaluation of railway wheels based on multibody dynamics and wear computation”. In: ***Multibody System Dynamics*** 24 (2010), pp. 347–366.

[36] J. Pombo, J. Ambrosio, et al. “Development of a wear prediction tool for steel railway wheels using three alternative wear functions”. In: ***Wear*** 20 (2011), pp. 327–358.

[37] A. A. Shabana, M. Tobaa, et al. “On the computer formulations of the wheel/rail contact problem”. In: ***Nonlinear Dynamics*** 40 (2005), pp. 169–193.

[38] T. Siefer and T. Hempe. “Rail grinding as un integral part of technically and economically efficient track maintenance”. In: ***ZEVrail Glasers Annalen*** 131 (2007), pp. 1–14.

[39] W. Specht. *Beitrag zur rechnerischen Bestimmung des Rad- und Schienenverschleisses durch Gueterwagen Diss*. RWTH Aachen, 1985.

[40] P. Toni. *Ottimizzazione dei profili delle ruote su binario con posa 1/20*. Trenitalia S.p.A., 2010.

[41] I. Zobory. “Prediction of wheel/rail profile wear”. In: ***Vehicle System Dynamics*** 28 (1997), pp. 221–259.

Publication on International Journals

[42] A. Innocenti, L. Marini, E. Meli, G. Pallini, A. Rindi. “Development of a Wear Model for the Analysis of Complex Railway Networks”. In: ***Wear*** 309 (2014), issues 1–2, pp. 174–191.

[43] J. Auciello, M. Ignesti, L. Marini, E. Meli, A. Rindi. “Development of a model for the analysis of wheel wear in railway vehicles”. In: ***Meccanica*** 40 (2013), pp. 681–697.

[44] J. Auciello, M. Ignesti, M. Malvezzi, E. Meli, A. Rindi. “Development and validation of a wear model for the analysis of the wheel profile evolution in railway vehicles”. In: ***Vehicle System Dynamics*** 50 (2012), issue 11, pp. 1707–1734.

[45] M. Ignesti, A. Innocenti, L. Marini, E. Meli, A. Rindi. “A numerical procedure for the wheel profile optimisation on railway vehicles”. In: ***Journal of Engineering Tribology*** 228 (2014), no. 2, pp. 206–222.

[46] M. Ignesti, A. Innocenti, L. Marini, E. Meli, A. Rindi. “Development of a wear model for the wheel profile optimisation on railway vehicles”. In: ***Vehicle System Dynamics*** 51 (2013), issue 9, pp. 1363–1402.

[47] M. Ignesti, A. Innocenti, L. Marini, E. Meli, A. Rindi, P. Toni. “Wheel profile optimization on railway vehicles from the wear viewpoint”. In: ***International Journal of Non-Linear Mechanics*** 53 (2013), pp. 41–54.

[48] M. Ignesti, L. Marini, A. Innocenti, E. Meli, A. Rindi. “Development of a model for the simultaneous analysis of wheel and rail wear in railway systems”. In: ***Multibody System Dynamics*** 31 (2014), issue 2, pp. 191–240.

[49] M. Ignesti, L. Marini, E. Meli, A. Rindi. “Development of a Model for the Prediction of Wheel and Rail Wear in the Railway Field”. In: ***ASME J. Comp. Nonlin. Dyn*** 7 (2012), pp. 1–14.

[50] M. Ignesti, L. Marini, M. Malvezzi, E. Meli, A. Rindi. “Development of a wear model for the prediction of wheel and rail profile evolution in railway systems”. In: ***Wear*** 284-285 (2012), pp. 1–17.

Publications on Proceedings of International Conferences

[51] J. Auciello, M. Ignesti, L. Marini, E. Meli, A. Rindi, P. Toni. "Wear modelling in railway vehicles: development and implementation of an innovative model for the prediction of the wheel profile evolution due to wear". In: Railways 2012 The 1st International Conference on Railway Technology. Gran Canaria, Spain, 2012.

[52] M. Ignesti, A. Innocenti, L. Marini, E. Meli, A. Rindi. "Development and validation of a wear model for the prediction of wheel and rail profile evolution on complex railway nets". In: European Congress on Computational Methods in Applied Sciences and Engineering (ECCOMAS). Zagreb, Croatia, 2013.

[53] M. Ignesti, A. Innocenti, L. Marini, E. Meli, A. Rindi. "Development of a new wear model for the prediction of wheel and rail profile evolution on complex railway networks". In: 23rd IAVSD Symposium on Dynamics of Vehicle on Roads and Tracks. Qingdao, China, 2013.

[54] M. Ignesti, A. Innocenti, L. Marini, E. Meli, A. Rindi. "Development of a new wear model for the study of wheel and rail profile evolution on complex railway networks". In: 5th World Tribology Congress (WTC). Turin, Italy, 2013.

[55] M. Ignesti, A. Innocenti, L. Marini, E. Meli, A. Rindi. "Development of a wear model for the wheel profile optimization on railway vehicles running on the Italian net". In: European Congress on Computational Methods in Applied Sciences and Engineering (ECCOMAS). Vienna, Austria, 2012.

[56] M. Ignesti, A. Innocenti, L. Marini, E. Meli, A. Rindi, P. Toni. "Development of a wear model for the wheel profile optimization in the railway field". In: The 2nd Joint International Conference on Multibody System Dynamics. Stuttgart, Germany, 2012.

[57] M. Ignesti, L. Marini, E. Meli, A. Rindi. "Wear prediction in the railway field: development of a model for the study of the wheel and rail profile evolution". In: European Congress on Computational Methods in Applied Sciences and Engineering (ECCOMAS). Vienna, Austria, 2012.